UNIVERSITY OF OKLAHOMA

GRADUATE COLLEGE

COGNITIVE MULTI-USER FREE SPACE OPTICAL COMMUNICATION

A DISSERTATION

SUBMITTED TO THE GRADUATE FACULTY

in partial fulfillment of the requirements for the

Degree of

DOCTOR OF PHILOSOPHY

in

ELECTRICAL & COMPUTER ENGINEERING

By
FEDERICA AVETA
Norman, Oklahoma
2020

COGNITIVE MULTI-USER FREE SPACE OPTICAL COMMUNICATION

A DISSERTATION APPROVED FOR THE

SCHOOL OF ELECTRICAL & COMPUTER ENGINEERING

BY THE COMMITTEE CONSISTING OF

Dr. Hazem H. Refai, Chair

Dr. Daniel Hamlin

Dr. James Sluss

Dr. Choon Yik Tang

Dr. Peter LoPresti

ACKNOWLEDGEMENTS

My Ph.D. journey has come to an end. There have been ups and downs during this fulfilling experience and I would like to express my gratitude to all the amazing people that have been there to celebrate with me while I enjoyed my "ups" and to support me during my "downs".

I would like to deeply thank my advisor Dr. Hazem Refai for his continuous support, mentorship and guidance during these years and for all of the opportunities I was given to further my research. During this journey he has always challenged me to accomplish more and to further enrich my academic and professional background.

I would like to extend my sincere appreciation to my doctoral committee members: Dr. Daniel Hamlin, Dr. James Sluss, Dr. Choon Yik Tang, and Dr. Peter LoPresti. Thank you for your time and insightful comments. A special acknowledgement of thanks is extended in memory of Dr. Thordur Runolfsson.

A huge thanks goes to my husband Giovanni. He has always believed in me and has constantly pushed me to achieve goals I would have never imagined I am capable of. I wouldn't be where I am if it wasn't for him. Thank you for the endless opportunities and experiences you decided to share with me.

A special thanks go to the the OU-Tulsa family of students, alumni, and staff. In particular, I want to thank everyone that has passed by office "4305" and made this journey comfortable, enjoyable, and sometimes funny. I have met two special friends Amal Algedir and Madelene Ghanem, and I am so grateful that our paths have crossed during this journey.

My sincere recognition goes to all people that have contributed to the realization of this work. I would like especially to thank Dr. Peter LoPresti for his help and guidance in his lab at the University of Tulsa. My appreciation goes to Michelle Farabough for editing

this dissertation and to Krista Pettersen for being so helpful every time I needed it. Finally, I am grateful for the advice, help, and brainstorming sessions with my OU colleagues.

I am so appreciative of my big family and for their unconditional trust and support throughout my life. Being far away from them has been the hardest part of this journey, and their love has helped me keep going throughout these years.

Finally, I want to thank all the wonderful friends I have met in Tulsa during this journey and for everything they have done to make me feel at home.

TABLE OF CONTENTS

LIST OF TABLES

LIST OF FIGURES

ABSTRACT

Increasing deployment of terrestrial, aerial, and space-based assets designed with more demanding services and applications is dramatically escalating the need for high capacity, high data-rate, adaptive, and flexible communication networks. Cognitive, multi-user Free Space Optical Communication (FSOC) networks provide a solution to address these challenges. Such FSOC networks can potentially merge automation and intelligence, as well as offer the benefits of optical communication with enhanced bandwidth and data-rate over long communication networks. Extensive research has investigated various designs, techniques, and methods to enable desired FSOC systems.

This dissertation reports the investigation and analysis of novel, state-of-the-art methodologies and algorithms for supporting cognitive, multi-user FSOC. This work details an investigation of the ability of diverse Optical-Multiple Access Control (O-MAC) techniques for performing multi-point communication. Independent Component Analysis (ICA) and Non-Orthogonal Multiple Access (NOMA) techniques were experimentally validated, both singularly and in a combined approach, in a high-speed FSOC link. These methods proved to successfully support multi-user FSOC when users share allocation resources (e.g., time, bandwidth, and space, among others). Additionally, transmission and channel parameters that can affect signal reconstruction performance were identified. To introduce cognition and flexibility into the network, the research reported herein details the use of several Machine Learning (ML) algorithms for estimating crucial parameters at the Physical Layer (PHY) of FSOC networks (e.g., number of transmitting users, modulation format, and quality of transmission [QoT]) for automatically supporting and decoding multiple users. In particular, a novel methodology based on a weighted clustering analysis for automatic and blind user discovery is presented in this work. Extensive experimental anal-

ysis was conducted under multiple communication scenarios to identify system performance and limitations. Experimental results demonstrated the ability of the proposed techniques to successfully estimate parameters of interest with high accuracy. Finally, this dissertation presents the design and testing of a modular, multiple node, high-speed, real-time Optical Wireless Communication (OWC) testbed, which provides a hardware and software platform for testing proposed methods and for further research development.

This dissertation successfully proves the feasibility of cognitive, multi-user FSOC through the developed and presented methodologies, as well as extensive experimental analyses. The main strength of the research outcomes of this work consists of exploiting software solutions (e.g., O-MAC, signal processing, and ML techniques) to intelligently support multiple users into a single optical channel (i.e., same allocation resources). Accordingly, Size, Weight and Power (SWaP) requirement can be reduced while achieving an increased network capacity.

CHAPTER 1

INTRODUCTION

1.1 Introduction

The free space optical communication (FSOC) technology market is in the midst of significant growth over a forecast period 2018-2023, increasing from USD 0.27 billion to USD 1.45 billion [1]. This expansion can be attributed to the ever growing demand of fast, flexible, and secure wireless communication technologies across various applications, including intelligence, surveillance, reconnaissance, last mile connectivity, backhaul, disaster recovery, satellite, and airborne communications, among others [2]. Currently, most communication links are based on Radio Frequency (RF) technology. While RF is suitable for many applications, the migration toward high and secure data-rate, high bandwidth, and dense connectivity is crucial for future communication networks [3]. Several solutions have been proposed for overcoming the RF data-rate and spectrum scarcity bottleneck [4]. Research groups have investigated methodologies for more efficient usage of the available spectrum (e.g., multiple antenna systems, adaptive modulation, coding systems, and others) in [5], [6] or for more aggressive temporal and spatial sprectrum reuse (e.g., cognitive radio systems, device to device communication, femto cells, and others) in [7], [8], [9]. Other research has focused on using unregulated bandwidth in the upper portion of the electromagnetic spectrum (e.g., microwave, millimeter wave, optical spectrum, and others) [6], [10], [11]. FSOC is the wireless communication technology that uses the infrared portion of the optical spectrum with frequency among 300 GHz and 430 THz corresponding to 700 nm to 1 mm wavelength range [11]. FSOC has been widely recognized as a promising technology when compared to the other approaches, primarly because it offers extremely high bandwidth, high data-rate, easy and quick deployment, unlicensed spectrum allocation, high beam directivity, reduced

power consumption (i.e., 1/2 of RF), reduced size (i.e., 1/10 of RF antenna diameter), and improved channel security [2], [12]. Table 1.1 summarizes the key features of FSO and RF communication technologies [13].

Table 1.1: Comparison of FSO and RF communication technologies

Property	FSO	RF
Operating frequency	THz	GHz
Bandwidth	Unregulated and unlimited	Regulated and limited
Data rate	Medium to high (> Gbps)	Low to medium (Gbps)
Transmitted beam size	Small (2 m)	Large (>2 m)
Data density	High	Low
Electromagnetic interference	No	Yes
Line of sight	Yes	No
Distance	Short to long	Short to long
Security	Excellent	Poor
Path loss	High	High
Multipath fading	No	Yes
Beam pattern	High degree of control with lenses	Difficulty to constrain on antenna size
Obstacle interference	Medium	Low
Services	Communication, sensing	Communication, localization
Noise sources	Sunlight, ambient light	Electrical, electronic appliances
Power consumption	Low	Medium
Mobility	Limited	Good
Latency	Low	High

State-of-the-art available Free Space Optics (FSO) solutions for space- and air-based networks have been introduced by private companies and government agencies. Project Loon by X aims to address internet connectivity scarcity for a significant part of the unserved world's population, as well as for emergency disaster, with a network of high-altitude balloons traveling the stratosphere (See Fig. 1.1a). FSOC has been adopted for inter-balloon crosslinks by offering high data-rates and long communication ranges, making it well suited for communication between high-altitude platforms. Results from Project Loon's early-phase experimental inter-balloon links at 20 km altitude demonstrated full duplex 130 Mbps throughput at distances in excess of 100 km over the course of several day flights [14]. FSOC

(a) Loon

(b) LLCD

Figure 1.1: FSOC aerial and space applications

for space applications is also gaining much interest [15]. NASA Space Communications and Navigation (SCaN) developed and tested optical communication technology using lasers with the Lunar Laser Communications Demonstration (LLCD) from October 2013 through April 2014 during the Lunar Atmosphere and Dust Environment Explorer (LADEE) mission (See Fig. 1.1b). The LLCD demonstration consisted of a space terminal on the LADEE spacecraft on the Lunar orbit and three ground terminals on Earth with transmission rate in uplink up to 622 Mbps [16]. In conjunction with NASA's Space Technology Mission Directorate (STMD), SCaN is working on the Laser Communications Relay Demonstration (LCRD). LCRD will be NASA's first long-period optical communications project aimed at demonstrating benefits for both deep space and near-Earth missions. LCRD will also validate that advanced relay operations are possible, and that it could be used for future relays, like on Mars. The project will reuse ground terminals developed for LLCD, demonstrating uplink communication up to 1.25 Gbps. These recent successful and promising results demonstrate the feasibility of FSOC for space and aerial applications to meet the increasing demand for wireless capacity and high-speed data transfer, and to be quickly and easily deployed for emergency communication during disasters.

The downside of current FSOC systems is the need for strict pointing, acquisition

and tracking (PAT) systems, which require bulky mechanical gimbals and Fast Steering Mirrors (FSM) for ensuring coarse and fine allignment, for maintaining link availability, and for guaranteeing wide or omni-directional coverage [17]. PAT systems are known to violate mobile communication network Size, Weight and Power (SWaP) requirements [18]. To advance optical wireless networking capabilities and to make FSO a viable substitute for RF technology without affecting such restrictive SWaP specifications, omni-directional and multi-user communication should be provided [19]. Multi-user FSOC, a leap from the current single user limitation, will guarantee high aggregate bandwidth performance, increased capacity, dense connectivity, and fast establishment of communication links among multiple users in the network. Despite these advantages, multi-user capabilities will also cause increased system complexity and heterogeneity with regard to communicating devices, varied transmission technologies, diverse quality of service (QoS) requirements from each user and diverse data processing requirements. Consequently, it is highly desirable to utilize an intelligent and flexible omni-directional, multi-user FSO system providing a) autonomous and real-time number of communicating users detection; b) dynamic and autonomous Optical-Multiple Access Control (O-MAC) techniques selection; c) real-time dynamic adjustment of transmitting/receiving parameters; d) agile, on-demand diverse service requirement fulfillments; and e) autonomous transmitter/receiver add and drop [20]. Thus, introducing self-configuration, self-optimization, and automated decision-making capabilities for supporting heterogeneous users and services presents a significant challenge for future optical wireless networks [20], [21], [22], [23]. Current research efforts are focusing on investigating and implementing technologies and methods that enable high capacity and cognitive multi-user FSOC.

1.2 Motivation

A cognitive, multi-user FSO system would enhance current FSOC system capabilities by concurrently guaranteeing:

1. **Low SWaP**.

Multi-user along with omni-directional Line of Sight (LoS) capabilities will eliminate

the need for bulky and expensive mechanical PAT systems to maintain link connectivity among nodes.

2. **Increased system capacity**.

   Users sharing allocation resources and simultaneously communicating into the receiver can be detected, decoded, and demodulated using traditional and novel O-MAC and Machine Learning (ML) algorithms. Multi-user communication will foster increased system bandwidth and aggregate data-rate.

3. **Robust communication**.

   Point to multi-point communication can be leveraged for implementing diversity gain schemes to improve signal quality and link reliability. Spatial diversity has been considered an attractive technique to mitigate fading and detrimental noise effects on the optical received signal.

4. **Dense connectivity**.

   Contrary to traditional MAC methods relying on orthogonality constraint, non-orthogonal O-MAC techniques do not limit the number of users that can be served by available resources. Superimposing the signal of multiple users on a same resource block results in efficient utilization of available resources and increased connectivity for users.

5. **Intelligent communication**.

   ML algorithms will make optical nodes aware of real-time network conditions and, consequently, adjust and optimize receiver parameters for maximizing communication performance and number of supported users.

1.3 Research Objective

The contribution of this work aims at answering the following research questions:

1. Given the point-to-point inherent limitation of FSOC, can we extend FSOC capabilities

to enable point to multi-point, multi-point to point, and multi-point to multi-point optical links?

2. Can we build an intelligent FSOC system to observe, plan, decide, and act autonomously for optimizing multi-user communication performance and minimizing the need for human supervision?

3. How can research advancements in the FSOC domain be tested and validated for subsequent deployment for implementation in future optical networks?

This dissertation addresses the aforementioned research questions by deriving theoretical and empirical models; by developing and/or implementing proposed and state-of-the-art signal processing and ML algorithms; by testing implemented methodologies through experiments and simulations; and by conducting extensive performance analysis.

1.4 Contribution

This dissertation poses the investigation, implementation, development, experimental testing, and validation of O-MAC techniques, signal processing, and ML algorithms for supporting cognitive and multi-user FSOC. Moreover, this work aims to test and prove omni-directional and multi-user capabilities for FSOC and to validate the developed methodologies and algorithms, by presenting the design, development and testing of an optical wireless communication (OWC) testbed. Investigations have produced the contributions listed below to the field of FSOC. Successful research outcomes can be easily extended into the OWC field for various applications and domains.

1. Investigate, experimentally test, and validate O-MAC and signal processing techniques for enabling multi-user communication into an optical-access point (O-AP) that shares channel allocation resources, such as:

    - Independent Component Analysis (ICA)
    - Non-Orthogonal Multiple Access (NOMA)

2. Establish a novel analytical model for network initialization or for blind user discovery in a communication protocol in future multi-user FSOC networks.

3. Derive an empirical equation for identifying optimal receiving parameters for accurate user discovery.

4. Establish ML-based methodologies for enhancing cognitive capabilities at the Physical (PHY) layer of FSOC networks, beyond existing efforts into cognitive, fiber-based networks for future OWC systems, like:

    - Users Number
    - Users SNRs
    - Modulation Format

5. Detail extensive experimental testing and analysis for diverse communication scenarios by clearly identifying system performance and limitations in real-time system design and implementation.

6. Present the design, implementation, and evaluation of a multi-user OWC testbed, testing for the following:

    - single or multiple users,
    - atmospheric turbulence,
    - diversity combining,
    - real-time analysis,
    - off-time analysis,
    - omni-directional receivers,

1.5 Dissertation Outline

The balance of this dissertation is organized as follows. Chapter 2 presents related work on multi-user OWC methods, omni-directional FSOC technologies, machine learn-

ing applications in optical communication, and state-of-the-art OWC testbeds. Chapter 3, presents three O-MAC techniques, namely: ICA, NOMA, and a combination of the two, as well as the methodology and experimental setup utilized in the study. Experimental results, along with the performance analysis for each technique, are also described. Chapter 4 introduces several methodologies exploiting unsupervised and supervised ML algorithms for introducing cognition at the PHY-layer. A novel methodology for estimating number of concurrently transmitting users is theoretically investigated and experimentally validated. Extensive analysis is presented to highlight system configurations and limitations. The chapter also illustrates a method for estimating Quality of Transmission (QoT) in an experimental FSO communication link. Finally, the chapter concludes with a Convolutional Neural Network (CNN)-based technique that classifies number of simultaneously communicating users and their modulation format. Chapter 5 provides a detailed description of the design, capabilities, and preliminary results of the developed OWC testbed. Finally, Chapter 6 summarizes conclusions of this dissertation, along with possible future developments.

1.6 Dissemination

Research outcomes have been disseminated through the following conferences proceedings, and peer reviewed articles.

- Aveta, F., Refai, H. H., & LoPresti, P. (2017, June). Multi-user FSO communication link. In 2017 Cognitive Communications for Aerospace Applications Workshop (CCAA) (pp. 1-5). IEEE [24].

- Aveta, F., Refai, H. H., LoPresti, P., Tedder, S. A., & Schoenholz, B. L. (2018, February). Independent component analysis for processing optical signals in support of multi-user communication. In Free-Space Laser Communication and Atmospheric Propagation XXX (Vol. 10524, p. 105241D). International Society for Optics and Photonics [25].

- Aveta, F., Refai, H. H., & LoPresti, P. G. (2019). Multiple access technique in a

high-speed free-space optical communication link: independent component analysis. Optical Engineering, 58(3), 036111 [26].

- Aveta, F., & Refai, H. H. (2019, March). Free space optical non-orthogonal multiple access experimentation. In Free-Space Laser Communications XXXI (Vol. 10910, p. 109101O). International Society for Optics and Photonics [27].

- Aveta, F., Refai, H. H., & LoPresti, P. (2019, June). Multi-user detection in optical wireless communication. In 2019 15th International Wireless Communications & Mobile Computing Conference (IWCMC) (pp. 214-219). IEEE [28].

- Aveta, F., Refai, H. H., & LoPresti, P. G. (2019). Number of Users Detection in Multi-Point FSOC Using Unsupervised Machine Learning. IEEE Photonics Technology Letters, 31(22), 1811-1814 [29].

- Aveta, F., & Refai, H. H. (2020). Modulation format and number of users classification in multipoint free-space optical communication using convolutional neural network. Optical Engineering, 59(6), 060501 [30].

- Aveta, F., Refai, H. H., & LoPresti, P. (2020). "Cognitive Multi-Point Free Space Optical Communication: Real-Time Users Discovery using Unsupervised Machine Learning," in IEEE Access, doi: 10.1109/ACCESS.2020.3038624.[31]

- Aveta, F., Chan, S. & Refai, H. H., (2020). Cognitive multi-user free space optical communication testbed. In Free-Space Laser Communications XXXII. International Society for Optics and Photonics. Accepted.

CHAPTER 2

LITERATURE REVIEW

2.1 Multi-User FSO Technology

Existing efforts to develop and support multi-user FSOC primarily focus on enlarging individual receiver Field of View (FoV) and designing multi-directional transmitters and receivers that satisfy the strict SWaP requirements of space- and air-based operations. In addition to investigations centered on physical layer efforts, recent research efforts are focused on developing signal processing and O-MAC techniques to support multi-user communication at an FSO node.

2.1.1 O-PHY Layer

Several PHY layer design approaches aimed at multi-directional transmitters and receivers have been proposed. A multi-element spherical array transceiver for indoor Visible Light Communications (VLC) was proposed in [32], [33]. The transmitter consisted of a hemispherical bulb with narrow FoV LEDs arranged in circular layers to maximize transmitting coverage area. The authors used computer simulations to demonstrate good link quality and high spatial reuse for indoor applications. However, the short-range nature of LEDs makes the method unsuitable for long-range communication links. Another proposed solution for achieving omni-directional optical transceivers employs optical fiber bundles to collect light from multiple directions and deliver it to one or more detectors. In [34], [35], the optical receiver design is composed of a tree with 850 fibers splayed apart, forming a hemispherical shape at one end and a photodetector placed on the other end for receiving light from combined optical fibers output. Experimental results demonstrated only 100 kbps over 1 m. Notably, only static nodes were tested, demonstrating this solu-

tion is not suitable for mobile applications. In [36], a fiber bundle receiver with tolerance to both physical misalignment and turbulence effects was demonstrated. The receiver was composed of a hexagonal array of 19 lenses coupling light to Multimode Fibers (MF) with a 400 μm core, a 0.37 Numerical Aperture (NA), and an optical system for focusing light from the bundle onto a fast detector. The system demonstrated an FoV up to $\mp$ 10° and a reduction in collected power variations in the presence of turbulence with respect to a standard Single Mode Fibers (SMF) based receiver for 850, 1310, and 1550 nm wavelengths. In [37], [38], the authors introduced Modular Optical Wireless Elements (MOWE) comprised of smart and electrically interconnected optical modules that combined to form modular, inexpensive, programmable, lightweight, wide-area, and omni-directional arrays. Each element represented a single optical-point transmitter, receiver, or combined transceiver that incorporated a low-power microcontroller. Detailed simulations and experiments demonstrated the potential for using MOWE for omni-directional optical antennas, beam steering, user tracking, and mobility support. Recent research on photonic lanterns demonstrated potential for enhancing the FoV and coupling efficiency of a fiber-coupled FSO receiver. Photonic lanterns provide low-loss transition from an N MF to N SMF. In [39] a comparison of coupling a 1550 nm beam over a 1.6 km link distance for both 3-MF and SMF receivers was presented. Experimental results showed that the 3-MF fiber coupled 3 dB more power and had lower sensitivity to tilt errors when compared to the SMF receiver. Another group designed and experimentally tested a toroidal-shaped omni-directional optical receiver [40], [41]. The optical receiver included an arrangement of Wavelength Shifting (WLS) fibers for enabling the use of small, active area, high-speed photodetectors. Experimental results showed a flat azimuthal angular data-rate response that proved receiver feasibility for sustaining omni-directional optical wireless communication. Notably, the optical receiver should be encased within a protective shroud to protect the WS fibers in all directions from the dynamic environment. The design presented significant SWaP challenges, making it unsuitable for space- and aerial-network applications. One group [42] proposed an omni-directional, optical-sensor array system to implement a full FoV light field camera. The omni-directional

image sensor comprises a hemispherical arrangement of a large number of CMOS imagers connected to a layered arrangement of high-end FPGA systems for data and image processing. The limited data-rate of Optical Camera Communication (OCC) resulting from low frame rates of conventional cameras makes the system unsuitable for Gbps long-range FSOC. In [43], [44], an inter-satellite, omni-directional communicator was designed and developed. The system was composed of an optical transceiver system, including a fast processor chip and a set of optical transceivers suitably located such that omnidirectional coverage could be achieved. Each transceiver consisted of a fast PIN photodiode detector and gimbal-less Micro-ElectroMechanical System (MEMS) for scanning mirrors and single-mode laser diodes. The fast processor chip could be either a FPGA or a microcontroller. Simulation results using an optical link budget model showed communication at Gbps rates over long distances with Non-Return-to-Zero On-Off Keying (NRZ-OOK) modulation scheme. Having a single, central processing unit could result in an increased computational load when compared to a local, distributed and parallel processing unit system.

2.1.2 O-MAC Layer

In [45], a Coherent Optical-Orthogonal Frequency Division Multiplexing Access (CO-OFDMA) technique is adopted in the FSOC system. M-ary Phase Shift Keying (MPSK) with M=4, 8, 16 downstream signals were transmitted at 40 Gbps for both 100 meter and 300 meter links under five weather conditions. Simulation results were provided through Bit Error Rate (BER) performance. [46] introduced a Space Division/Time Division Multiple Access (SD/TDMA) scheme for achieving a point to multi-point connection between long distance points by changing the path of infrared rays with reflectors. With regard to experimental results of received power, BER and throughput indicated that the proposed scheme is able to provide a low-cost and efficient method for point to multi-point FSOC. [47] presented the design of an optical Code Division Multiple Access (CDMA) over FSOC system at data-rate of 2.5 Gbps for 8 km link. BER simulation results showed that system performance is primarily limited by the multi-access interference (MAI) from multiple users. [48] introduced

Wavelength Division Multiplexing (WDM) technique for achieving a FSOC link with aggregate data-rate up to 200 Gbps. Eight channels with wavelengths in the C-band with 50 GHz channel interval, with 25 Gbps data-rate, and with 4-Pulse Amplitude Modulation (PAM) format were utilized in the 50 meter, outdoor experiment. Experimental results showed stable BER performance and clear eye-diagram for each channel, demonstrating the feasibility of WDM for FSOC. Such channel access techniques are termed Orthogonal Multiple Access (OMA) schemes. When OMA is employed, various users are allocated orthogonal resources (i.e., time, bandwidth, space resources) and permit a receiver to entirely separate received signals according to various basis functions. Current research has focused on a NOMA technique, wherein users share time, bandwidth, space, and other resources and are multiplexed in the power domain [49]. NOMA is able to achieve higher spectral efficiency and system capacity than other OMA techniques. Altough NOMA has been widely studied in the VLC domain to support multiple users [50], [51], [52], [53], little attention has centered on the NOMA technique in the FSOC field. In [54], researchers considered a multi-point to point FSOC system using NOMA and a power control scheme. Analytical results examined outage probability, ergodic sum data-rate, and BER. Findings showed that NOMA achieves a superior ergodic sum data-rate when compared with OMA. Authors in [55] employed NOMA for FSO backhaul and developed a dynamic optimal decoding scheme. Simulations suggested the feasibility of a dynamic NOMA scheme over Gamma-Gamma turbulence. Notably, most research that aims at extending NOMA in FSOC has been conducted through analytical and computer simulations. No experimental investigations have explored NOMA in a FSOC link.

2.2 Cognitive O-PHY Layer

ML methodology has been widely employed to introduce intelligence in the network, making systems capable of independently performing cognitive tasks. Current research is developing techniques to embed intelligence in optical networks at the PHY layer domain [20], [22], [21]. For example, applications of ML at the PHY include QoT estimation, Mod-

ulation Format Recognition (MFR), and Optical Performance Monitoring (OPM), to name just a few.

OPM in an optical communication system has become crucial for ensuring robust and reliable system performance. OPM consists of estimating physical parameters without prior knowledge of incoming optical signals (e.g., BER, Optical Signal-to-Noise Ratio (OSNR), Polarization Mode Dispersion (PMD), Chromatic Dispersion (CD), and Q-factor, among others). Estimated parameters will be employed for activities, like adjusting transmitted power, routing traffic, and changing modulation format. Researchers in [56], [57] proposed using an Artificial Neural Network (ANN) for simultaneously monitoring OSNR, CD, and PMD. In [56], the author trained ANN using asynchronous amplitude histogram. Simulation results for both 40 Gbps Return-to-Zero Differential Quadrature Phase-Shift Keying (RZ-DQPSK) and 40 Gbps 16 Quadrature Amplitude Modulation (16-QAM) systems demonstrated high monitoring accuracies. In [57], an ANN was trained using the first five empirical moments of the asynchronously sampled signal amplitude. The first five amplitude signal empirical moments traversing through an offset fiber branch were added to the ANN training phase for discriminating the sign of accumulated CD. Simulations in a 40/56 Gbps RZ-DQPSK and 40 Gbps RZ- Differential Phase-Shift Keying (DPSK) systems proved good simultaneous, along with independent in-band OSNR and signed CD and PMD monitoring accuracy. Authors experimentally demonstrated the use of a Deep Neural Network (DNN) for OSNR monitoring in [58] and the use of a CNN for OSNR estimation and modulation format/symbol rate classification in [59] using asynchronously sampled raw data collected by a coherent receiver. 512 samples x 4 channels corresponding to the Horizontal (H) and Vertical (V) polarization of the In-phase (I) and Quadrature-phase (Q) components of the optical field (e.g., HI, HQ, VI and VQ) were used as input for NN. In [58] a five-layer DNN proved to successfully estimate OSNR in 16 GBd Dual-Polarization Quadrature Phase-Shift Keying (DP-QPSK) with a measured averaged error of 1.6 dB. The CNN in [59] proved to successfully estimate OSNR in 14 and 16 GBd DP-QPSK, 16-QAM, and 64-QAM systems with a Mean Square Error (MSE) of less than 0.3 dB for all tested modulation formats. A

classification accuracy $> 95\%$ was achieved for modulation format/symbol rate classification.

MFR aims at estimating the modulation format at the receiver side, without prior information from transmitters, with a goal of improving signal demodulation accuracy and signal processing. Some Digital Signal Processing (DSP) algorithms utilized in a coherent receiver, (e.g., adaptive equalization, carrier phase recovery, and symbol detection) are modulation-format dependent. In [60] authors experimentally demonstrated MFR in a 312.5 MBd QPSK, 8 Phase Shift Keying (PSK) and 16-QAM system over 40 km of SMF using a clustering technique. A K-means algorithm was adopted to estimate the number of clusters in the 2-dimensional I and Q constellation diagram. BER results proved successful demodulation for all tested modulation formats. Authors in [60] implemented a simultaneous MFR and OSNR estimation using a CNN and eye-diagram for training. Eye-diagrams were simulated for a wide range of OSNR and four modulation formats, namely RZ-OOK, NRZ-OOK, RZ-DPSK, and 4-PAM. MFR accuracy and OSNR estimation of 100% were achieved. Authors in [61] used an NN-based, nonlinear regression and Support Vector Machine (SVM) classifier to experimentally demonstrate independent in-band OSNR estimation and MFR. Four modulation formats QPSK, 8-QAM, 16-QAM and 64-QAM were experimentally tested and eight features were extracted from the power eye-diagram of the directly-detected optical signals. Results showed that the NN proved accurate OSNR estimation with a mean error of 0.7 dB, and the classifier obtained an average classification accuracy of 94%.

QoT estimation in an optical link includes predicting some PHY parameters of a candidate light path (e.g., OSNR, BER, Q-factor, and others), that may affect signal detection at the receiver side. Thus, these parameters represent a metric to check if a required QoT would be guaranteed. In [62] a QoT estimation technique that considers both linear and nonlinear impairments was proposed. Synthetic BER data were calculated with varying total link length, span length values, channel input powers, data-rate and modulation formats. Three ML-based classifiers, Random Forest (RF), SVM and K-Nearest Neighbor (KNN) were used to predict whether or not light path BER will exceed a stated threshold. Results proved that SVM outperforms the other two classifiers. Classification accuracy of

99.15% was achieved. Authors in [63] proposed and experimentally validated an ANN-based transfer learning method to predict the Q-factor in different optical transmission systems without re-training the all ANN model. The ANN was trained in a 4-span Large Effective Area Fiber (LEAF) 100 Gbps QPSK testbed, and was then used to predict Q-factor in three optical systems, namely 4-span LEAF 200 Gbps 16-QAM, 2-span LEAF 200 Gbps 16-QAM, and 3-span Dispersion-Shifted Fiber (DSF) 100 Gbps QPSK. A Q-factor prediction accuracy of 0.42 dB, 0.37 dB, and 0.67 dB was achieved, respectively. Current ML applications in optical communication consider mainly point to point and fiber-based networks. Extension of ML applications in the FSOC domain is still in its infancy.

2.3 OWC Testbed

In [64] the authors present a testbed fabricated at the Johns Hopkins University Applied Physics Laboratory to emulate an FSO mobile tactical network. The testbed aims to evaluate network topology and restoration at the PHY, Logical Link, and Networking layers. Software tools were developed for network management, including the Tactical Edge Network Emulation Tool (TENET) [65] and Distributed Adaptive Pre-computed Restoration (DAPR) algorithm [66]. TENET models a mobile directional network in a 3D terrain; DAPR evaluates the network and dynamically optimizes its physical topology to maximize performance. Active X control was used to synchronize software tools with the LabVIEW controlled static mesh network. The FSO network consists of six nodes connected to an MEMS optical switch for dynamically configuring the links between fixed nodes. Mobility is emulated in a static infrastructure. Notably, practical issues related to mobility (e.g., misalignment) that could affect the network topology reconfiguration are not addressed in this work. The National Institute of Information and Communication Technology has been working throughout the country of Japan with a Terrestrial Free-Space Optical Communications Network (INNOVA) testbed to implement a site diversity technique with several optical ground stations [67], [68]. Receiver diversity aims to perform high-speed data transmission in future airborne- and satellite-based optical communication. A ground station network

was equipped with several large aperture telescopes (e.g., 1 m) linked through a wired network and controlled remotely by an optical ground station control center. The switching mechanism among the ground stations was headed by the weather and channel atmospheric conditions. Environmental data collection stations will be installed at several Japan sites for collecting climate data from sensors network. No PAT mechanisms have been considered or proposed for performing channel switching. [69], [70] presented an experimental testbed to prove high-speed (e.g., >1.6 Tbps) FSO communication in an uplink GEO satellite; however, the authors proposed to use transmitter diversity to reach their projected throughput performance. The testbed is part of the Terabit Throughout Satellite Technology (THRUST) project undertaken by the German Aerospace Center (DLR) and will consist of three main subsystems, namely communications, optomechanical, and metrology. To perform transmit diversity Dense Wavelength Division Multiplexing (DWDM) with 40 channels in the optical C-band is proposed. The optomechanical subsystem will provide an accurate and high precision alignment mechanism for both Satellite (SAT) and Optical Ground Stations (OGS). SAT and OGS will both be mounted on a Coarse Pointing Assembly (CPA) to ensure fast and coarse alignment. A Fine Point Assembly (FPA) will be included for obtaining a more precise and accurate alignment. To further optimize the FPA, an additional fine-pointing mechanism based on a PIN diode was introduced in the SAT. Ultimately, the metrology subsystem on both SAT and OGS will be equipped with a weather station (e.g., camera, scintillometer, power meter, thermometer) to measure real time weather and atmospheric channel characteristics. A data acquisition device will collect raw data.

Several research groups have proposed and implemented a testbed to further characterize and study the atmospheric turbulence profile. In [71], an electro-optic testbed is presented to measure an integrated turbulence error profile. Researchers proposed an expansion of the existing testbed located at the John Bryan Observatory in Ohio. A Shack-Hartmann wavefront sensor coupled with a dynamically range-gate Rayleigh beacon was used to capture the pupil image from a 24-inch quad-axis telescope. Various beam waist sizes and range-gated time intervals resulted in a conical volume over which the refractive

index fluctuations were integrated to obtain a turbulence induced wavefront error profile. Authors in [72] reported on the Atmospheric Laser Optics Testbed (A-LOT) located in the Army Research Laboratory (ARL) facility. A-LOT includes a 2.3 km horizontal propagating path that connects the laboratory building, which is 12 m above the ground, to a 73 m water tower. The laboratory site is equipped with a transceiver from the TereScope 3000 laser communication system designed to provide a communication link with the tower, a transceiver for live imagery transmission and adaptive optics, a scintillometer, and several high-speed CCD cameras for measuring intensity scintillations. The tower is equipped with a retro-reflector to double the propagation path length to 4.6 km; a laser communication transceiver as part of the TereScope 3000 system; and a Terrain 1000X laser transceiver for experimental investigation of beam steering and tracking. A sensors network for continuous real-time monitoring of atmospheric conditions and laser beam parameters is equipped with a scintillometer, visibility sensor, weather station, and a system for providing meteorological data. Artificial smoke, fog, and rain generators were installed in the laboratory facility to simulate controllable weather conditions. A maritime Lasercom Test Facility (LCTF) at the U.S. Naval Research Laboratory is presented in [73], [74], [75]. The LCTF is characterized by a 16 km one-way and 32 km round-trip links over water. The transmitting side is located on a building 30 m above water level with an FSM that controls pointing and system alignment. On the other side, optical receivers, atmospheric diagnostic equipment, and computer control systems positioned at approximately water level guarantee the 16 km communication link and the analysis of atmospheric conditions. On that same side, an array of retro-reflectors is mounted at 15 m above the sea level to double the propagation path to 32 km. Testbeds focus exclusively on the atmospheric turbulence effects of propagating optical signals.

Other research groups have introduced optical testbed facilities for supporting a wide variety of applications that are different from FSO communication. For example, the Optical Systems Test (OSTF) facility has been established at the MIT Lincoln Laboratory [76]. The facility consists of four separate test areas, namely an active range (Laser Radar Test Facility), a passive range (Seeker Experimental System), an aerosol range (Standoff

Aerosol Active Signature Testbed [SAAST]), and an Optical Material Measurement Range (OMMR). The active range was built to test and evaluate complete or partially integrated laser radar systems [77]. The test facility has a control room with ladar operation stations, a 50 m range with a bistatic ladar system on one side and a dynamic target manipulator at the opposite end. A passive range was designed for ballistic missile interceptor seeker evaluation. The optical system was equipped with a dynamic scene generator module and blackbody sources that are imaged, through a Cryogenic Scene Projection System (CSPS), onto the seeker under test. The SAAST area was established to measure the polarization-dependent, optical scattering cross section of samples generated in the laboratory at diverse wavelengths and angles [78]. The testbed was set in a vacuum chamber and included aerosol samples, scatter monitors, polarization analyzer, and avalanche photodiode mounted on a rotating table. The OMMR testbed was created to perform measurements of emissivity and reflectance of complex surfaces and materials ranging from a visible to infrared band. A scanning electron microscope was used to perform measurements; later, a Fourier Transform Interferometer was added to extend the measurement into the infrared band. In [79] a multi-cell lightening testbed was implemented to investigate LiFi technology (i.e., VLC) and indoor positioning techniques (i.e., visible light positioning [VLP]). The testbed was composed of a 3x5 array of 15 LED-based luminaries on the ceiling of a room modulated by Software Defined Ratio (SDR) based on Universal Software Radio Peripheral (USRP) hardware. A mobile receiver was implemented to rotate and tilt toward arbitrary angles on a fixed plane positioned below the luminaries plane. Authors in [80] introduced an extension of an existing Software Defined Communication (SDC) testbed for implementing FSOC. To support the high-bandwidth demand of FSOC, FPGA technology (i.e., Xilinx ML605 FPGA) was proposed. This solution offers a high level of parallelization and pipelining to provide an efficient and fast reconfigurable communication platform. Furthermore, implementation of scalable OFDM PHY in FSOC through a combination of custom hardware and software development, was also investigated.

CHAPTER 3

O-MAC TECHNIQUES

3.1 ICA

ICA is an unsupervised signal processing technique recognized as the most widely used for performing Blind Source Separation (BSS), where estimation of source signals is required from observed mixtures sans information about channel state and original transmitted signals [80]. ICA has been leveraged for a variety of applications, including robotics, biomedical signal processing, speech processing, and wireless communication. For RF wireless communication, ICA has been adopted, in particular, for wireless sensor networks (WSNs), cognitive radio networks (CRNs), multiple input and multiple output systems (MIMO), and CDMA [80]. ICA relies on simple assumptions based on signal statistical properties, assuming statistically independent sources with only one Gaussian distribution [81]. This method can be executed in two ways [82]: information theoretic or higher order statistics (HOS). The information theoretic approach uses statistically independent measures to separate signals based on information theory. Well-known algorithms in this class include Infomax [83] and minimizing Kullback-Leibler (KL) divergence [84]. HOS methods, on the other hand, estimate directions for maximizing a component's non-Gaussianity by using negentropy or kurtosis. The most widely used HOS algorithms are Joint Approximate Diagonalization of Eigenmatrices (JADE) [84] and FastICA [85]. Extension of the use of ICA method in FSOC for multi-user detection in a multi-point system is studied in this dissertation.

3.1.1 Methodology

The ICA model is based on a statistical "latent variables" system. Assume N transmitters broadcast statistically independent signals $s_1(t), s_2(t), ..., s_N(t)$ with M receivers

observing signals $x_1(t), x_2(t), ..., x_M(t)$, which are linear and instantaneous mixtures of the original sources. Considering transmitted and observed signals as random variables, the ICA model can be represented in a matrix form, as follows [81]:

$$x = As \tag{3.1}$$

where $x = [x_1, x_2, ..., x_M]^T$ is the observed mixtures vector; $s = [s_1, s_2, ..., s_N]^T$ is the unknown source signals vector; and A is the mxn unknown mixing matrix. Hence, the objective is to recover original components s_i and matrix A by using only mixed received signals. To solve this problem, the following assumptions should be made. Original sources s_i should be statistically independent and should not have Gaussian distribution—with only one exception—so that mixing matrix A can be estimated. In fact, HOS are always zero for Gaussian distribution; this information is essential for statistic independence. Notably, these distributions are considered unknown. For simplicity, mixing matrix A is assumed square, and number of observing sensors is equal to the number of sources ($m = n$). Moreover, the mixing matrix is assumed to be non-singular. After estimating the mixing matrix, it is possible to compute its inverse $A^{-1} = W$, where W represents the un-mixing matrix. Therefore, independent components vector s is:

$$s = Wx \tag{3.2}$$

The model's solution is characterized by ambiguities, namely scale and permutation. Scale ambiguity causes uncertainties in component magnitude and sign because determining independent component variance is impossible. In fact, given that s_i and A are unknown, any scalar α_i multiplied by s_i can be deleted by dividing the respective column a_i of A by the same scalar.

$$x = \sum_i (\frac{1}{\alpha_i} a_i)(\alpha_i s_i) \tag{3.3}$$

Permutation ambiguity causes uncertainty in original component order because it is impos-

sible to determine. In fact, in Eq. 3.3, it is possible to change the order of the terms and to consider any independent component as the first one. Moreover, Eq. 3.1 can be rewritten, as follows:

$$x = AP^{-1}Ps \tag{3.4}$$

where P is the permutation matrix and P^{-1} is its inverse. Thus, elements of Ps are the original independent components in another order, and AP^{-1} is a new, unknown mixing matrix. Although such ambiguities are not a crucial problem in the instantaneous ICA model, this problem must be considered and solved for some applications wherein the mixing process is not linear [86]. FastICA and JADE algorithms were employed in this work and are described in Appendix A.

3.1.2 Experimental Setup

The FSOC experimental setup is shown in 3.1. 3.1a depicts a flow diagram; 3.1b shows a picture of hardware device configuration. The setup consists of two independent users based on an Intensity Modulation with Direct Detection (IM/DD) scheme. A high-speed (e.g., 12.5 Gbps) Digital Reference Transmitter, namely Thorlabs MX10B, that includes an integrated tunable C band laser source, was driven by a pseudo random bit sequence (PRBS) with $2^{31} - 1$ bits in length and 5 Mbps data-rate. PRBS was generated by a USRP, namely Ettus Research USRP X310. USRP was connected to a personal computer via Ethernet, and LabVIEW software was used to generate the signal. A 1310 nm optical module transceiver (SFP) via SMA to SFP board was driven by a PRBS with $2^{31} - 1$ bits in length and initial 100 Mbps data-rate. The sequence was generated by a Bert Scope pattern generator, namely SyntheSys Research BSA12500A. Both signal sequences were split with power splitters to facilitate oscilloscope data collection. Generated optical signals were sent using a wideband, single-mode, 2x2 fiber optic coupler, which centers at 1550 nm and 1310 nm with a bandwidth of $\mp$40 nm. Both outputs of the fiber coupler act as a power splitter with 50:50 coupling ratios. Hence, transmitted signals were mixed in the first section of the coupler, and later the mixed signal was split into two outputs with equal power. Regarding

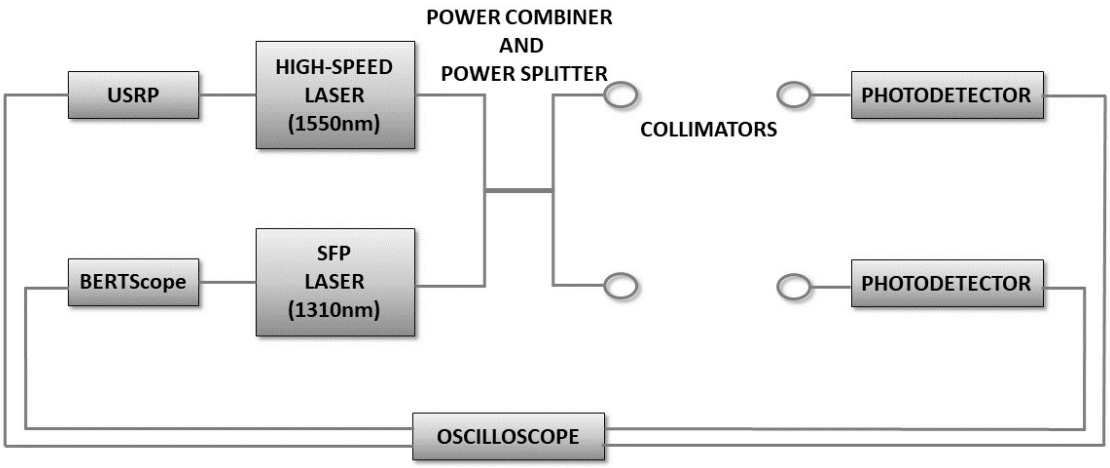

(a) Depiction

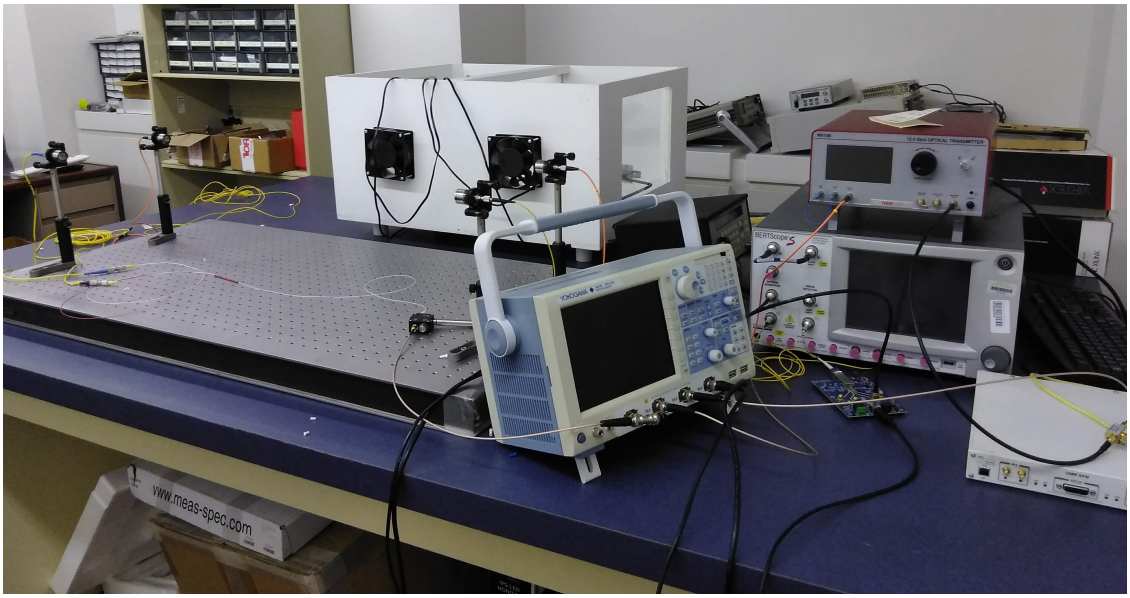

(b) Picture

Figure 3.1: Experimental setup

outputs, two collimators with wavelength dependence of the anti-reflection (AR) coating for minimizing surface reflections were used. One collimator with 37.17 mm focal length (i.e., 1550 nm wavelength dependent) and another with 36.90 mm focal length (i.e., 1310 nm wavelength dependent) were used. Mixed signal propagation will be affected differently by the collimators according to design wavelength. Mixed signals were propagated through free space for 1.5 m, and then collected by two 5 GHz InGaAs photodetectors, namely Thorlabs DET08CFC. A four-channel digital oscilloscope with 5 GSample/s sampling rate was used to record data collected from the photodetectors and the transmitted PRBS. Data were

post processed to perform ICA offline with MATLAB software on a 2.60 GHz Intel Core i7 processor.

3.1.3 Results

The effectiveness of the FastICA algorithm, effects of signal power, data-rate, turbulence levels, and a detailed turbulence analysis, as well as computational complexity, and system capacity were investigated. Moreover, performances of a second JADE algorithm were considered to validate the ICA method for signal demodulation in an FSO link. As such, diverse performance indexes were used to evaluate results. The parameter used for evaluating ICA mixing matrix reconstruction was the Signal Interference Ratio (SIR). Normalized Root Mean Square Error (NRMSE) and cross-correlation were used for evaluating source signal reconstruction accuracy. SIR is expressed as follows [86]:

$$SIR = 10\log_{10}\left(\frac{E[(|y|_{\sigma(j),j})]^2}{E[(|y|_{\sigma(j),k})^2]}\right) \tag{3.5}$$

Eq. 3.5 indicates the amount of useful signal on the j^{th} channel relative to other k^{th} components considered as interfering signals following signal separation. Thus a higher SIR value for the j^{th} channel is desired for good separation and results in the algorithm's ability to successfully eliminate interference on useful signals.

Data collection and post-processing were performed using MATLAB. A Graphical User Interface (GUI) was realized to facilitate data processing, allowing loading and plotting transmitted and received mixed signals. Power in dBm, data-rate in Mbps, and turbulence level are shown in the GUI. FastICA and JADE algorithms can be performed, and reconstructed signals and original transmitted sequences can be plotted. Moreover, performance evaluation parameters (e.g., SIR, NRMSE, and cross-correlation) are shown in the GUI. Fig. 3.2 shows an example of GUI data acquisition and processing.

1. **Power Ratio**

Power selection analysis was conducted to define the power pair value for guaranteeing

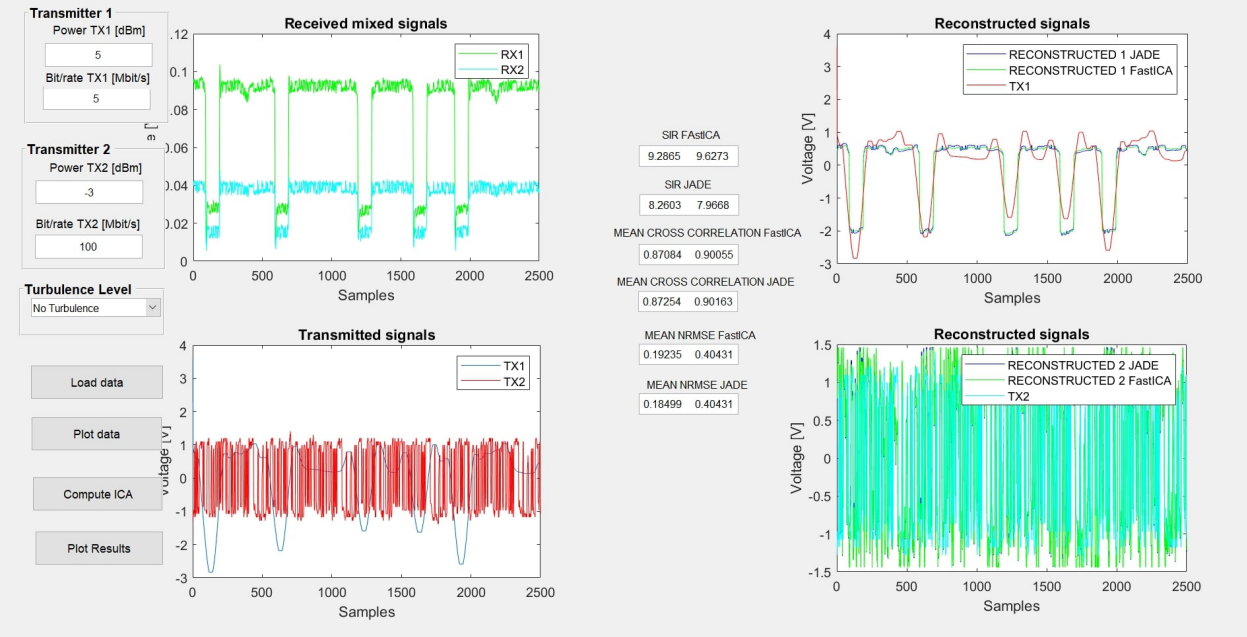

Figure 3.2: GUI

signal reconstruction with the highest accuracy (i.e., cross-correlation). User 1 has a tunable transmission power P_1 that ranges between -3 and 5 dBm, and user 2 has a fixed transmission power P_2 of -3 dBm. To relate users' power, a power ratio (PR) coefficient was defined as $PR = P_2/P_1$. Given $P_1 \geq P_2$, PR is defined in the range [0.16 ,1]. Testing began with $P_1 = 5$ dBm. For each subsequent acquisition, P_1 was reduced with steps of 1 dB until a power ratio of 1 was reached. Cross-correlation and NRMSE were computed. Their trends versus PR coefficient are shown in Fig. 3.3. In Fig. 3.3a, black and blue continuous lines represent cross-correlation between reconstructed signals by FastICA algorithm and original transmitted signals of user 1 and user 2 respectively; black and blue dashed lines represent the same for JADE algorithm. The red continuous and dashed lines represent mean cross-correlation between the two users for both FastICA and JADE, respectively.

Cross-correlation greater than 0.84 was achieved for all PR coefficients tested, proving ICA capability to successfully separate and reconstruct the original transmitted signals from the received mixtures. However, user 1 signal reconstruction proved more accurate than that of user 2 for PR values less than 0.2. Notably, the opposite behav-

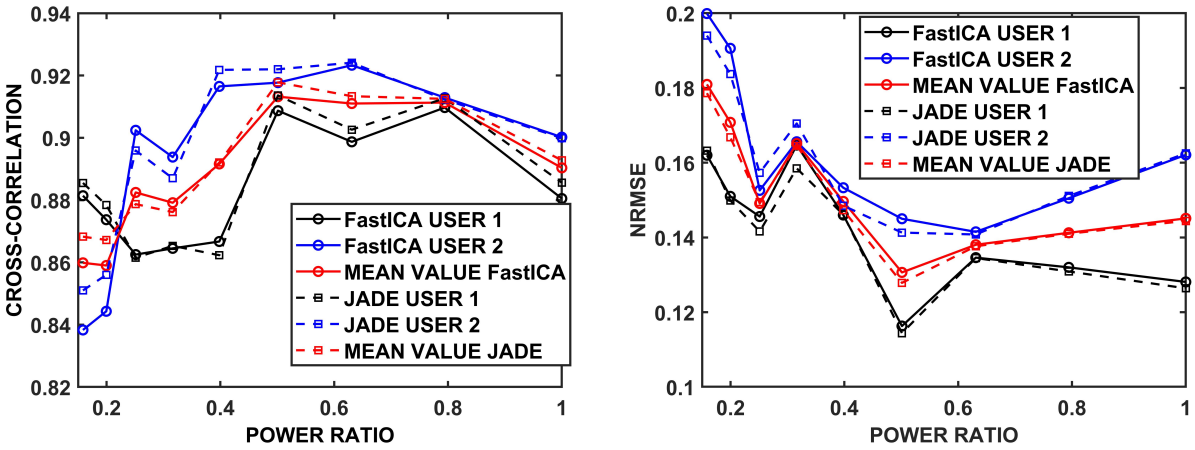

(a) Cross-correlation (b) NRMSE

Figure 3.3: Power ratio analysis

ior occurs with an increasing PR coefficient. For a small PR value, user 2 has very low power when compared with user 1, such that the algorithms might consider it as additive noise. Given algorithm assumption of a noiseless system, a less accurate reconstruction of the weak signal was expected. When PR increases (i.e., P_1 decreases), user 2 accuracy overcomes user 1. In fact, after signal separation, interference on reconstructed signals was observed in the tested PR range; reconstructed user 1 exhibited higher interference when compared to user 2. Considering the trend of the mean value of cross-correlation for both FastICA and JADE, a more accurate signal reconstruction occurs when PR =0.5 (i.e., P_1 = 0 dBm and P_2 = -3 dBm). After optimum value is attained, cross-correlation begins to decline due to the transmitting power approach of P_1 and P_2 to the same value. Notably, both algorithms have comparable separation results in terms of signal accuracy. A maximum difference in cross-correlation of 0.01 between the two algorithms was measured for PR=0.16. NRMSE versus PR is illustrated in Fig. 3.3b. Note that error decreases until a minimum value of PR = 0.5, at which point error commences to increase again. Greater NRMSE is obtained when P_1 and P_2 are either too close or too far. Since a similar behavior was observed for cross-correlation, it is reasonable to conclude that optimum PR for reconstruction is 0.5.

The section above describes results when separating two signals without considering interference. This section studies the effect of interference on separation analysis. Interference—characterized by the relative presence of the k_{th} source signal in the estimated j_{th} source signal—was observed after signal separation. Thus, signal separation accuracy is also related to the ability of ICA algorithms to cancel interference. The SIR parameter in Eq. 3.5 describes how the algorithm reconstructs the un-mixing matrix, specifically coupled terms w_{12} and w_{21}, which contain information about cross-talk components.

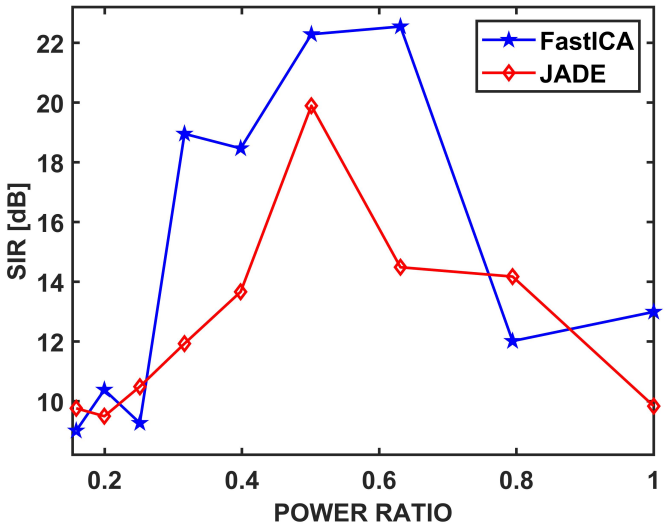

Figure 3.4: SIR

SIR was computed and is shown compared with PR in Fig. 3.4. The blue line is the average SIR between user 1 and user 2 using the FastICA algorithm, and the red line represents results using the JADE algorithm. Acceptable values of SIR were obtained for all PR with higher values for FastICA for most PR values. Optimal performance was obtained when PR=0.5. Separation results produced by FastICA method are similar to those achieved using the JADE algorithm. However, the FastICA algorithm is more capable of suppressing interference, and, in turn, generating a higher SIR.

Computational time is another important requirement for future hardware implementations and real-time processing applications. Fig. 3.5a illustrates algorithm compu-

tational time for each PR value. Computational time [s] for FastICA are illustrated as red dots and for JADE as light blue dots. Results show that FastICA has a 0.16 s mean computational time, and JADE has 0.02 s time. This indicates that JADE is one order of magnitude faster than FastICA in computational performance. The graph in Fig. 3.5a relates algorithm execution time with PR and cross-correlation. Computational time was related to signal reconstruction accuracy, and maximum value for PR was calculated as 0.5. Fig 3.5b illustrates achievable system capacity [bps/Hz] for both algorithms when compared with the mean NRMSE for each PR (in the color bar). System capacity was computed as [87]:

$$C = C_1 + C_2 = log_2(1 + SINR_1) + log_2(1 + SINR_2) \tag{3.6}$$

where $SINR_1 = \frac{P_1}{P_2+N_0}$; $SINR_2 = \frac{P_2}{P_1+N_0}$ and N_0 is noise power density. Notably, NRMSE capacity increases when $PR \geq 0.5$ and decreases when $PR < 0.5$. As such, maximum acceptable error will define achievable capacity for the proposed system.

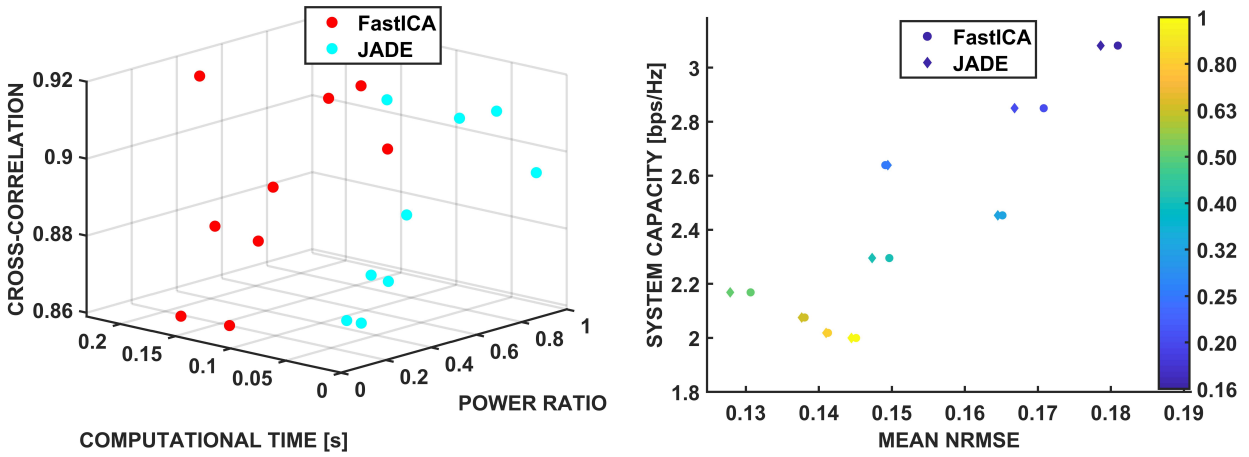

(a) Computational time [s]

(b) System capacity [bps/Hz]

Figure 3.5: Power ratio analysis

2. **Data Rate**

Analysis of signal separation performance for high data-rate and for varying rate differences between user 1 and user 2 was conducted. A PR of 0.5 was used, and data-rate

for user 1 was set to 5 Mbps. For user 2, data-rate varied from 5 Mbps to 400 Mbps with data-rate difference ranging from 0, 95, 195, 295, and 395 Mbps. Cross-correlation and NRMSE versus data-rate difference are shown in Fig. 3.6. A high value for cross-correlation was obtained when users had the same or similar data-rate, with maximum difference of 95 Mbps. At that point, performance began to decrease, given an increasing data-rate difference between users. Faster decay was observed for user 2 with changing communication speed. NRMSE in Fig. 3.6b illustrates the same behavior. An increasing NRMSE was obtained as the difference in data-rate range increased.

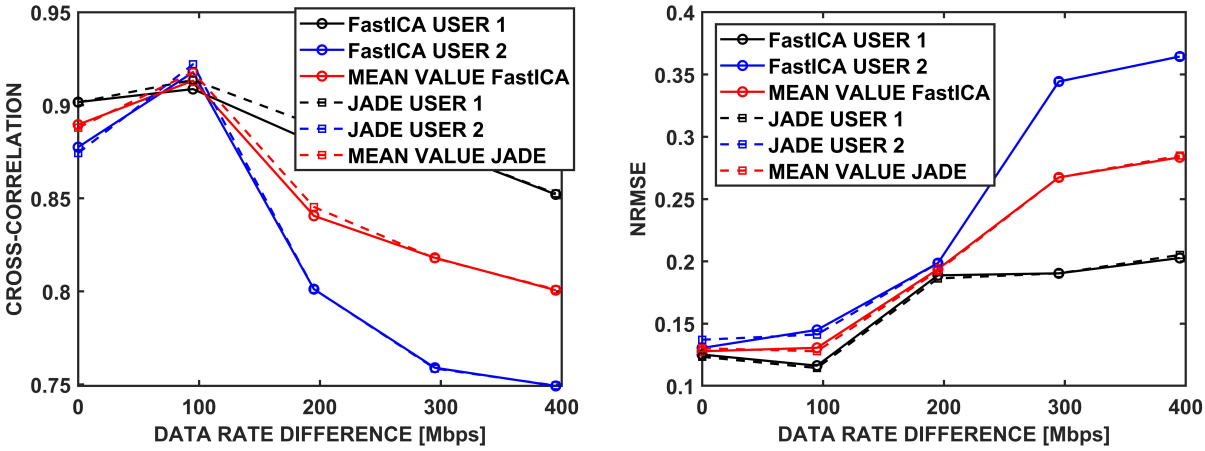

(a) Cross-correlation (b) NRMSE

Figure 3.6: Data rate analysis

Thus, it is possible to conclude that leveraging ICA methods for signal separation provides good results, given that user 1 and user 2 have either the same or a comparable bit rate. When data-rates commence to differ (e.g., $>$ 95 Mbps), signal separation quality worsens.

3. **Atmospheric Turbulence**

FSOC links can be significantly affected by atmospheric turbulence-induced scintillation, which leads to power loss, random fluctuation of the received intensity, and degraded communication performance[12]. As such, a turbulence box for emulating atmospheric turbulence was built. To evaluate and characterize the generated turbu-

lence a beam profiler and two experimental parameters, namely scintillation index σ_I^2 [88] and refractive index structure constant C_n^2 [89], were employed. The box was designed with two chambers separated by a plexiglass pane, making each independently programmable and controllable. Both chambers were equipped with a heating element on the bottom, enabling an adjustable temperature range that could vary between 10 [°] and 230 [°]. The chambers were also furnished with two AC fans able to operate at a maximum wind speed of 33 m/s; a variable humidifier; and a ventilation aperture, as shown in Fig. 3.7a. The ventilation box was equipped with sensors controlled by Arduino microcontroller for implementing a weather station to measure and store real time wind speed, humidity and temperature data, as illustrated in Fig. 3.7b. Generated atmospheric turbulence was characterized by low, medium, and high turbulence; wind speed, humidity, and temperature were measured in each regime. Table 3.1 summarizes the sensors reading values.

(a) Beam-profiler (b) Weather station

Figure 3.7: Turbulence box

Table 3.1: Turbulent regime characterization

TURBULENCE	Temperature[°]	Wind Speed[m/s]	Humidity[%]
LOW	37.12	5.32	60.94
MEDIUM	58.61	14.21	80.56
HIGH	74.08	25.89	96.77

For each regime, the beam profiler, namely Spiricon LT665-1550, was used to capture and analyze the beam shape coming from the 1550 nm laser diode. The beam profiler was placed behind the turbulence box (i.e., 1 m from the 1550 nm laser diode) with the camera plane orthogonal to the beam propagation direction. Data was collected and recorded for five minutes, and 1-D, 2-D and 3-D beam profiles were captured. Optical beam was a Gaussian CW with 1550.11 nm wavelength and transmitted power of 5.3 dBm. Fig. 3.8 illustrates the measured 3-D beam profiles with no turbulence, 3.8a; low turbulence, 3.8b; medium turbulence, 3.8c; and high turbulence, 3.8d. Notably, the Gaussian beam is attenuated and distorted as a result of increasing turbulence.

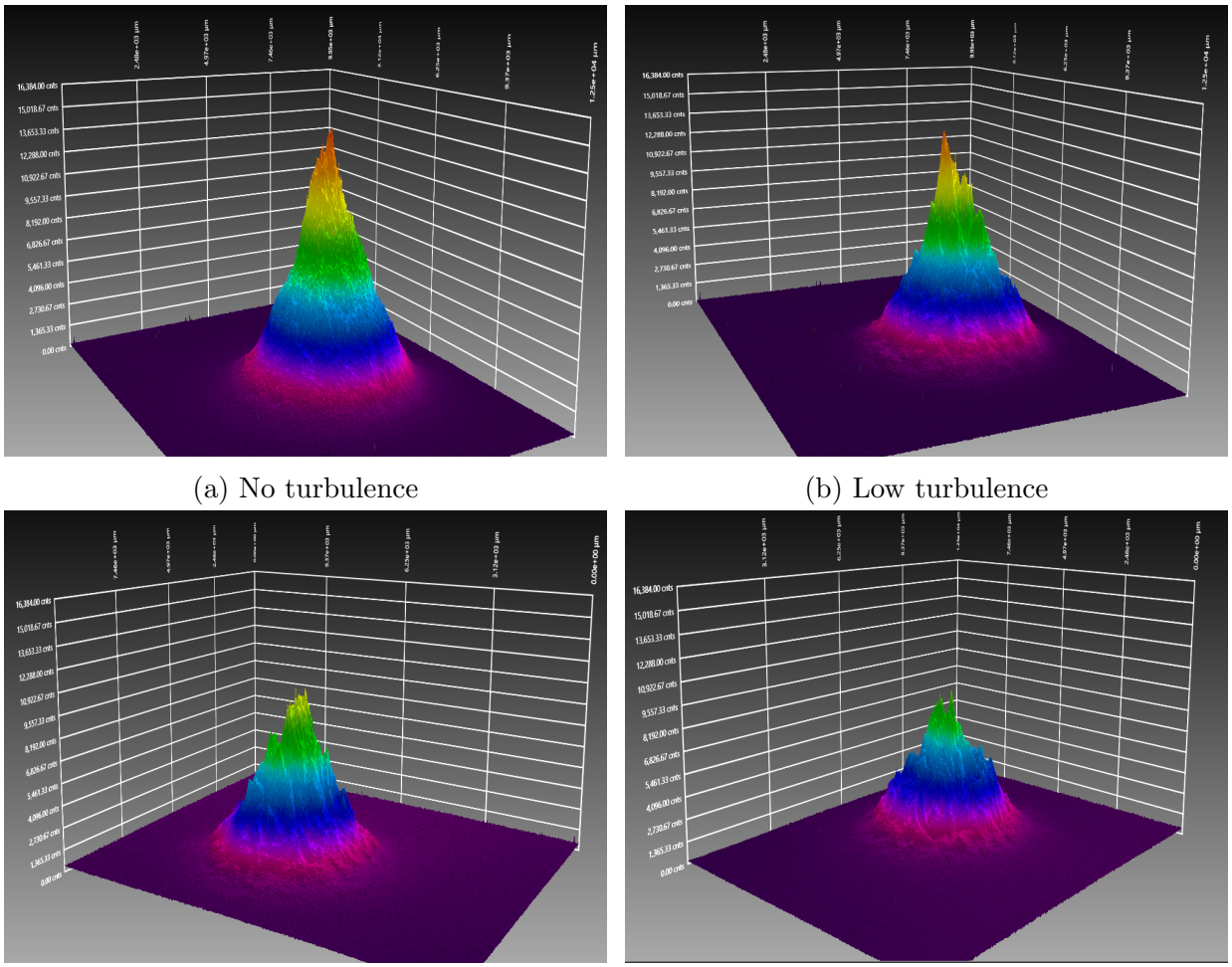

(a) No turbulence

(b) Low turbulence

(c) Medium turbulence

(d) High turbulence

Figure 3.8: 3-D beam profiler

After beam profiler collection, data were acquired with the oscilloscope for processing,

and then σ_I^2 and C_n^2 were calculated. CW optical signal was modulated with a square wave of 20 Mbps, and probability density functions of the collected signals were computed to show the impact of turbulence on intensity fluctuations. Fig. 3.9a illustrates the pdfs of received signals for low turbulence (indicated by blue bars), medium turbulence (indicated by magenta bars), and high turbulence (indicated by green bars). Broadening and attenuation of the 1's signal amplitude are shown in Fig. 3.9a. Broadening is due to increasing intensity fluctuations, as demonstrated by the increasing scintillation index σ_I^2. Attenuation is mainly caused by the humidity generator. For example, when humidity in the box increased, fog gradually occured, attenuating the optical beam and increasing path loss attenuation [90]. Fig. 3.9b illustrates that for the three turbulence levels employed in the experiment σ_I^2 (indicated by orange bars) and C_n^2 (indicated by blue bars). A σ_I^2 of 0.0078, 0.1330, and 0.2611 $[m^2]$, and a C_n^2 of $3.6091x10^{-13}$, $6.1876x10^{-12}$, and $1.2151x10^{-}11$ $[m^{-2/3}]$ were obtained for low, medium, and high turbulence, respectively. Given an increase in turbulence, an increase in C_n^2 and σ_I^2 is observed. Results confirm the capability of the box to generate various levels

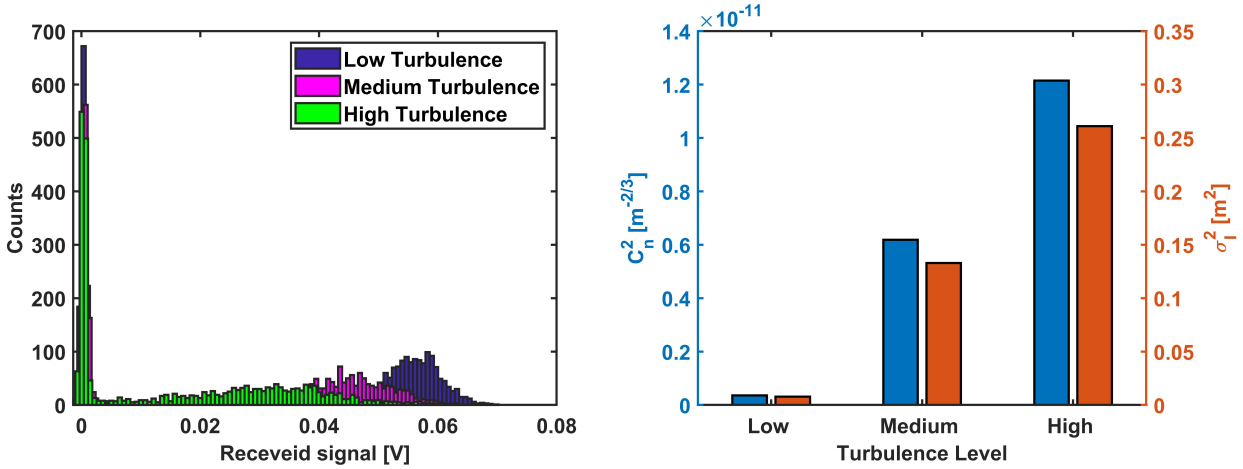

(a) pdfs of received signals

(b) C_n^2 and σ_I^2

Figure 3.9: Turbulence characterization

of turbulence. The analysis was conducted under three turbulent regimes and with the two chambers set with the same parameters. Notably, other configurations could be further tested and analyzed.

Data using optimal PR and data-rate difference were collected, and FastICA and JADE algorithms were employed. Fig. 3.10a and Fig. 3.10b show received mixed signals in the presence of high turbulence. Fig. 3.10c and Fig. 3.10d show reconstructed signals with FastICA algorithm (indicated by the blue line) and the original transmitted signals (indicated by the red line). Fig. 3.10b illustrates magnification of the graph in 3.10a to better demonstrate how the weaker signal is strongly affected by the turbulence, which is particularly evident in the blue line that represents the received signal placed in closer proximity to the humidifier. Notably, signal separation was successfully performed for both user 1 (See Fig. 3.10c) and user 2 (See Fig. 3.10d).

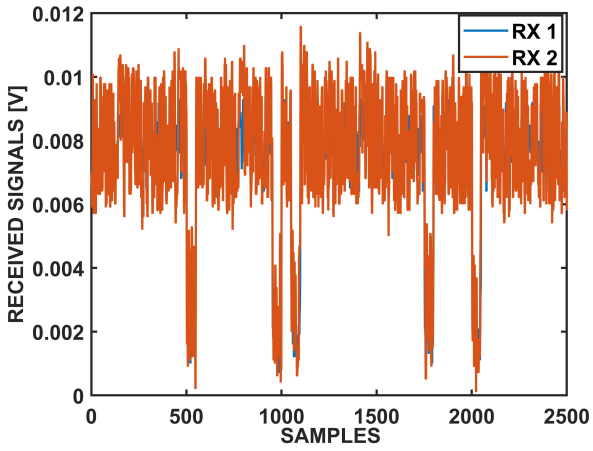

(a) Mixed received signals

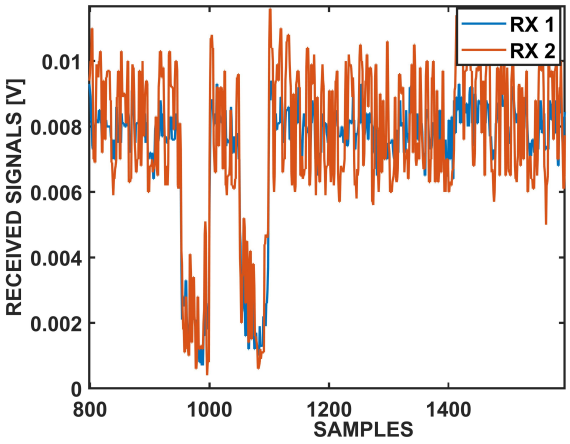

(b) Zoom of 3.10a

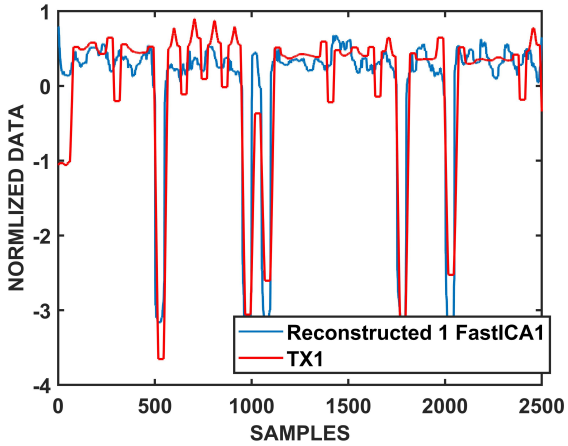

(c) Reconstructed user 1

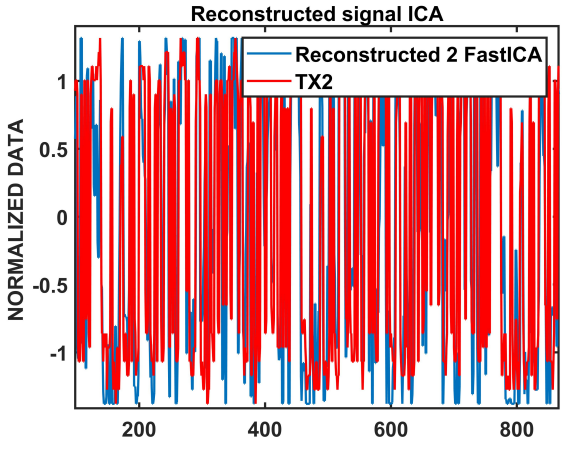

(d) Zoom of reconstructed user 2

Figure 3.10: Turbulence effects ICA

To quantify the error introduced as a result of turbulence, cross-correlation and the er-

ror respective of the non-turbulence scenario were analyzed. Fig. 3.11a illustrates the cross-correlation versus turbulence level. The continuous black line (indicating user 1) and continuous blue line (indicating user 2) were reconstructed via FastICA algorithm. The dashed black line (indicating user 1) and dashed blue line (indicating user 2) were the reconstructed via JADE algorithm. The continuous and dashed red lines illustrate the mean cross-correlation between the two users for FastICA and JADE algorithms, respectively. Cross correlation worsens with the degree of turbulence for both users. However, user 2 performance decreases more rapidly than user 1 performance. User 2 achieved a cross-correlation of less than 0.75 when compared to 0.9 reached by user 1. In fact, user 2 demonstrated a weaker signal and was more affected by the turbulence, as shown in Fig. 3.10a and Fig. 3.10b. Accordingly, mean error between users increases with the turbulence level for both algorithms, given with the same trend. Nevertheless, signal separation accuracy resulting from both algorithms was acceptable in all turbulence regimes tested.

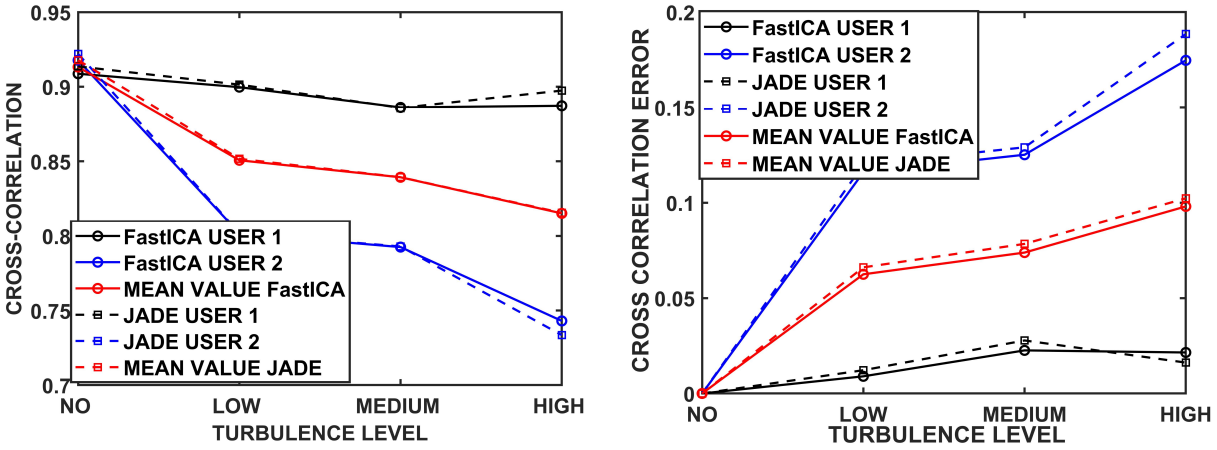

(a) Cross-correlation

(b) Cross-correlation error

Figure 3.11: Turbulence effects ICA

3.2 NOMA

Recently, a new MA technique, namely NOMA, has been introduced for 5G wireless networks with the goal of enhancing spectral efficiency [91],[92],[49]. NOMA is

also under consideration for VLC, to support multi-user communication [93],[94]. With this technology, users simultaneously share available resources and are multiplexed in the power domain by transmitting at various power levels or by exploiting diverse channel gains. The non-orthogonality of transmitted signals by different users results in inter-user interference. Hence, dedicated multi-user detection (MUD) techniques are required for retrieving transmitted signals. At the receiver, successive interference cancellation (SIC) is performed for signal detection of users in several stages, according to signal strength [95]. After channel state information (CSI) is obtained, the desired received signals are reconstructed and subtracted from the received signal. Once each user's received data is estimated, transmitted signals can be decoded [49]. NOMA outperforms conventional OMA techniques in the following scenarios [96]: higher spectral efficiency; increased number of simultaneously served users; and lower latency. Moreover, NOMA can guarantee QoS via intelligent power allocation schemes by allocating more power to users that require high QoS and less power to users that require low QoS.

3.2.1 Methodology

NOMA permits a number of users to share the same frequency and time channel in the power domain while multi-user detection is performed with SIC at the receiver. Each user transmits with power P_k. Hence, a superposition of the transmitted signal is collected at the single node receiver. The received signal at the photodetector is expressed as:

$$y = \sum_{k=1}^{N} (\eta h_k P_k s_k + n) \tag{3.7}$$

where N is the total number of users; η is the photodetector responsivity $[A/W]$; h_k is the channel gain; P_k is the allocated power for the $k-th$ user; s_k is the transmitted data sequence; and n is additive channel noise. Assuming a two-user scenario with $\eta = 1$, received signal is indicated by:

$$y = h_1 P_1 s_1 + h_2 P_2 s_2 + n \tag{3.8}$$

CSI is required for performing SIC. FSO is characterized by a slow fading channel (i.e., coherence time of atmospheric turbulence is greater than duration of a typical data symbol), so it can be easily estimated [97]. Thus, receiver starts decoding the strongest signal first and considers a weaker signal as interference. After the first user's signal is decoded, the signal is subtracted from the received signal. This must occur before the second user's signal is decoded. Assuming $h_1P_1 > h_2P_2$ and $\hat{h}_1$ is the estimated channel 1 gain, user 1 $\hat{s}_1$ will be decoded first using a single user decoder by treating user 2 as noise. By re-modulating estimated sequence $\hat{s}_1$ and subtracting reconstructed user 1 to received signal y, it is possible to detect user 2 data sequence $\hat{s}_2$ as follows:

$$y' = y - \hat{h}_1 P_1 \hat{s}_1 = (h_1 P_1 s_1 - \hat{h}_1 P_1 \hat{s}_1) + h_2 P_2 s_2 + n \approx h_2 P_2 s_2 + n \tag{3.9}$$

In this way, both users are decoded. Assuming perfect cancellation of user 1, user 2 is reconstructed along with additive noise. Let $P_1' = h_1P_1$ and $P_2' = h_2P_2$ be the received powers at the photodetector from user 1 and user 2, respectively. B is the receiver bandwidth, and N_0 is the channel noise. When both users transmit simultaneously, the receiver decodes the strongest signal first and considers the weaker signal as interference. According to Shannon Theory [87], by decoding the stronger signal under the assumption of no propagation errors, maximum achievable data-rate for user 1 can be determined by:

$$\hat{R}_1 = B \log_2 \left(1 + \frac{P_1'}{P_2' + N_0} \right) \tag{3.10}$$

Stronger signal P_1' can be successfully decoded, given that its data-rate $R_1 \leq \hat{R}_1$. After assuming perfect cancellation of P_1', maximum achievable data-rate for user 2 is:

$$\hat{R}_2 = B \log_2 \left(1 + \frac{P_2'}{N_0} \right) \tag{3.11}$$

For successful decoding, user 2 should follow the rule that $R_2 \leq \hat{R}_2$. To improve SIC decoding performance, user 2 might have a higher R_2 data-rate compared to user 1 data-

rate R_1. Achievable data-rate defines maximum feasible system capacity. With SIC, channel capacity can be expressed as follows:

$$C_{SIC} = \hat{R}_1 + \hat{R}_2 = B\log_2\left(1 + \frac{P_1'}{P_2' + N_0}\right) + B\log_2\left(1 + \frac{P_2'}{N_0}\right) = B\log_2\left(1 + \frac{P_1' + P_2'}{N_0}\right) \tag{3.12}$$

Given a common receiver with neither SIC or MA techniques, only one of the two transmitters can transmit and be successfully decoded. Thus, capacity is given by the maximum data-rate among the two users:

$$C_{NO-SIC} = max\left(\hat{R}_1, \hat{R}_2\right) = max\left(B\log_2\left(1 + \frac{P_1'}{N_0}\right), B\log_2\left(1 + \frac{P_2'}{N_0}\right)\right) \tag{3.13}$$

Since $C_{SIC} > C_{NO-SIC}$, higher capacity is achieved with SIC receiver. Fig. 2.14(b) demonstrates the CDF of normalized achievable capacity [bps/Hz] for NOMA both with SIC receiver and without SIC receiver.

3.2.2 Experimental Setup

The FSO experimental setup used in the research is shown in Fig. 3.12. In Fig. 3.12a, the depiction of the setup is presented, and in Fig. 3.12b, the hardware devices used for the two users are shown. The setup consists of two independent users based on an IM/DD scheme. The high-speed (e.g., 12.5 Gbps) digital reference C-band optical transmitter, was driven by a PRBS with $2^{31} - 1$ bits in length and 5 Mbps data-rate. PRBS was generated by the Ettus Research USRP X310. USRP was connected to a personal computer via Ethernet, and LabVIEW software was used to generate the signals. A 1310 nm SFP via SMA to SFP board was driven by a PRBS with $2^{31} - 1$ bits in length and initial 100 Mbps data-rate. The sequence was generated by the SyntheSys Research BSA12500A Bert Scope pattern generator. Both signal sequences were separated with power splitters to facilitate oscilloscope data collection. One collimator with 37.17 mm focal length (i.e., 1550 nm wavelength dependent) and another with 36.90 mm focal length (i.e., 1310 nm wavelength dependent) were used. The optical signal propagated through free space for 1.5 m. Then, the

received signals were mixed at the receiver side through a wavelength division multiplexer designed for combining two signals at 1310 nm and 1550 nm with a $\mp$15.0 nm bandwidth around the center wavelength of each channel. The 5 GHz InGaAs Thorlabs DET08CFC photodetector was used to collect the mixed signal. A four-channel, digital oscilloscope with 5 GSample/s sampling rate was used to record data collected from the photodetector and the transmitted PRBS. Data were post-processed to perform SIC offline with MATLAB software.

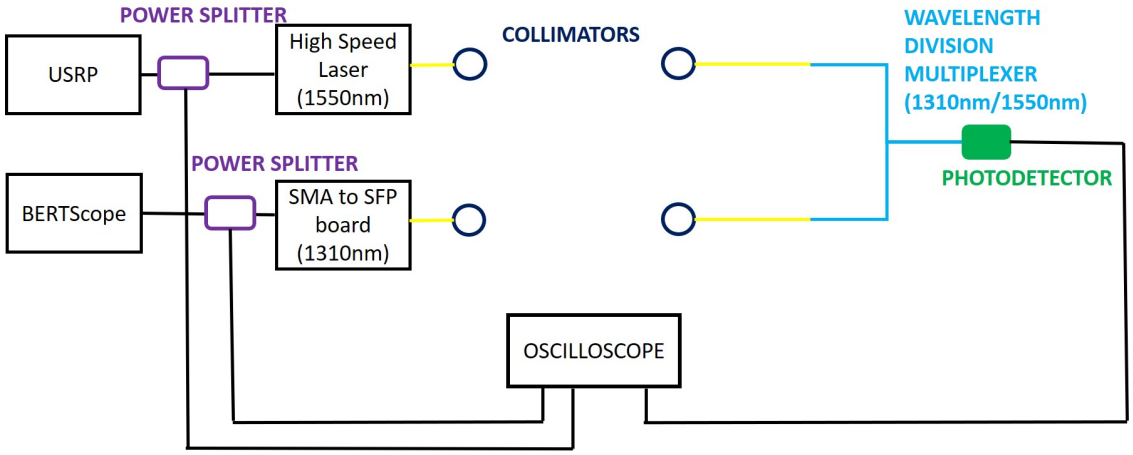

(a) Depiction

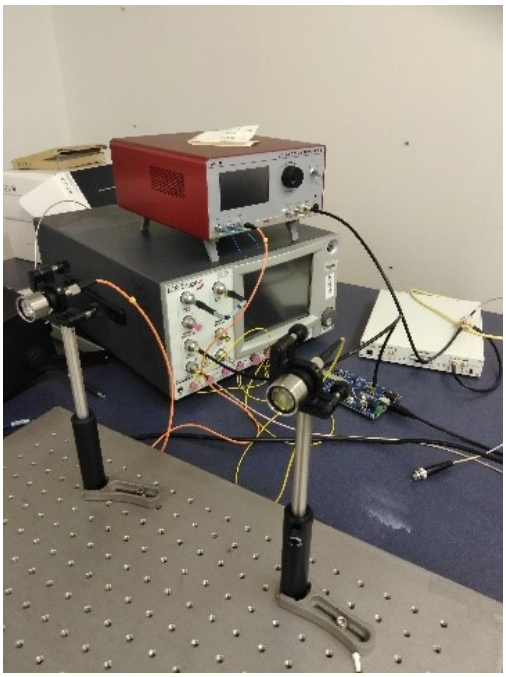

(b) Users

Figure 3.12: Experimental setup

3.2.3 Results

Experimental results with varying parameters, including transmitted power, data-rate, and CSI error, are presented. Given the internal memory of the oscilloscope for data acquisition (i.e., 2500 samples), normalized cross-correlation and NRMSE were used for evaluating performance. Pilot training sequences were sent at the beginning to obtain CSI. Next, data sequences were transmitted, and SIC was performed at the receiver side. The strongest signal was demodulated first, and the weakest signal later. An example of demodulated signals after SIC is shown in Fig. 3.14. Fig. 3.13 shows the received mixed signal from the photodetector. Fig. 3.14a and 3.14b show the reconstructed source signals (indicated by the blue line) and the original transmitted signals (indicated by the orange line) for user 1 and user 2, respectively. For user 1, a transmitted power P_1 of 4 dBm and data-rate of 5 Mbps were used; for user 2, a transmitted power P_2 of -3 dBm and data-rate of 100 Mbps were adopted. Thus, user 1 was the strongest signals and was decoded first, and, subsequently user 2 was decoded. Notably, signal separation was successfully performed.

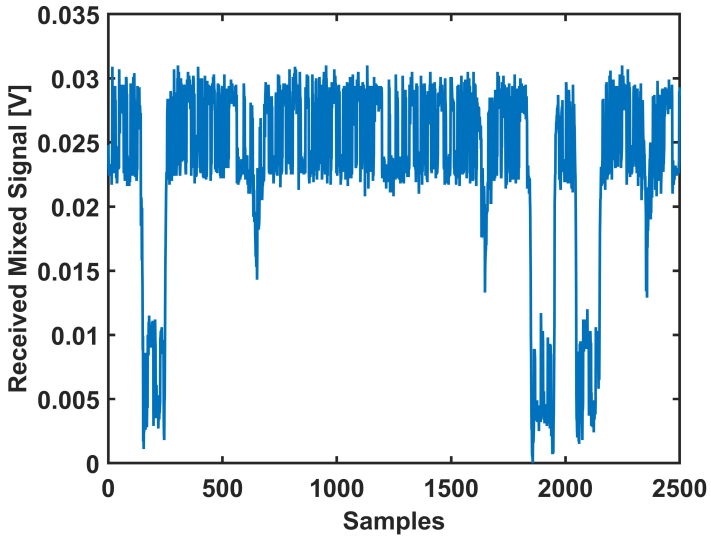

Figure 3.13: Mixed received signals

Eqs. 3.9 - 3.13 aid in understanding that transmitted power, channel estimation, and data-rate variation can impact signal demodulation accuracy. In the experiment, detailed in this dissertation, detailed analysis was performed to understand how signal power,

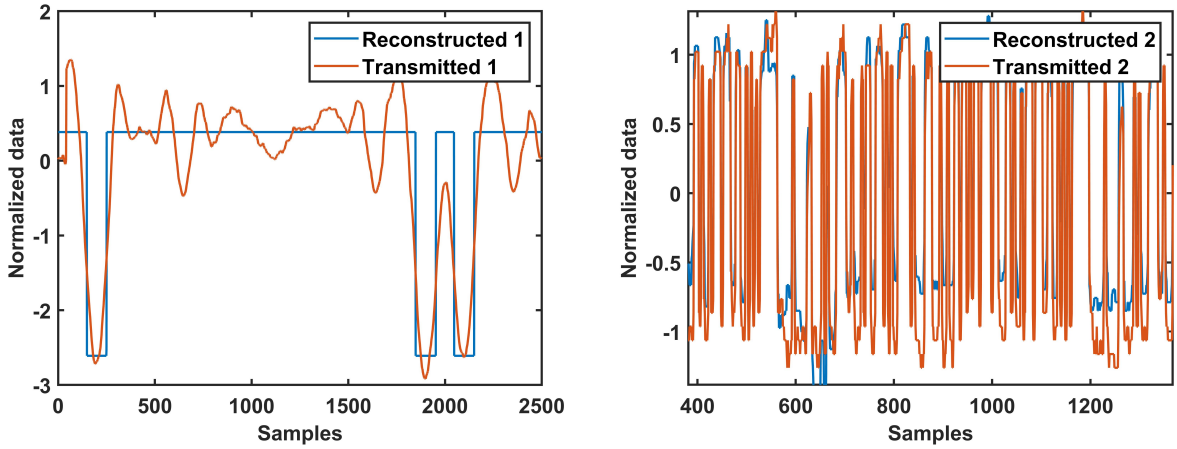

(a) Reconstructed user 1

(b) Reconstructed user 2

Figure 3.14: Reconstructed signals

channel estimation, and data-rate affect signal separation quality. Achievable system capacity was studied for NOMA and for non-SIC receiver.

1. **Power Selection and CSI**

   Because NOMA multiplexes users in the power domain, power allocation represents a critical issue. Static power allocation was performed, and various power ratio (i.e., $\left(\frac{P_2}{P_1+P_2}\right)$) were analyzed. Notably, the high-speed digital reference transmitter has an embedded optical attenuator that allows attenuation to vary between 1 dB and 15 dB. For the C-band laser (namely user 1), the transmitted power P_1 was set in a range between 4 dBm and -2 dBm with 1 dB steps. The 1310 nm transceiver (namely user 2) had a fixed transmitted power P_2 = -3 dBm. For each power pair, SIC was performed, and the normalized cross-correlation was computed to evaluate signal separation accuracy. Fig. 3.15a illustrates the normalized cross-correlation for user 1 (indicated by blue line) and user 2 (indicated by black line) versus the allocation power coefficient. The blue line decreases with the power allocation ratio because less power is allocated to user 1. Hence, less accuracy of signal reconstruction is expected. The black line increases with the power allocation coefficient until a maximum value for power allocation ratio of 0.33 is reached, before decreasing begins. This phenomenon indicates that user 2 is reconstructed less accurately when its power is too low and when its power

reaches values that are close to user 1 power. Reconstruction of user 1 is performed more accurately than for user 2 because user 1 is the strongest when compared with the weaker user 2, which is considered interference in the demodulating process. When user power values converge toward similarity, they are characterized by similar performance. Results proved that the most accurate reconstruction was achieved with a normalized

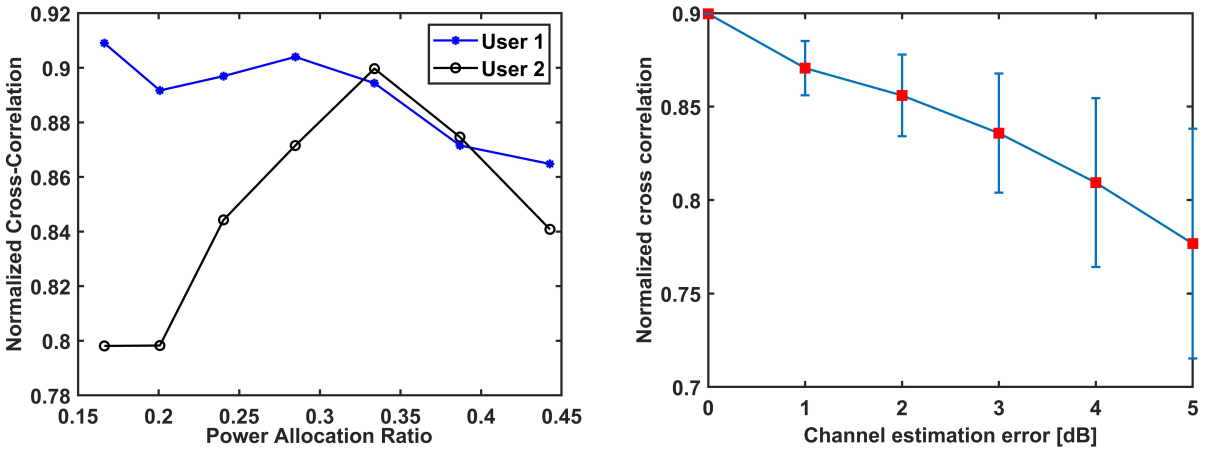

(a) Power ratio (b) Channel estimation error

Figure 3.15: Normalized cross-correlation

cross-correlation close to 0.9 for an allocation power coefficient of 0.33 (i.e., $P_1 = 0$ dBm and $P_2 = -3dBm$). Once the optimum power ratio coefficient was found, the effect of channel estimation error on the accuracy of signal demodulation was analyzed. This means that an error in CSI will cause a cancellation error in the SIC. Consequently, the cancellation error is expected to propagate in the demodulation process, affecting signal reconstruction accuracy of upcoming users. Considering CSI was estimated by the training sequence as the perfect CSI, an error of 1 dB was introduced, and the normalized cross-correlation and absolute error were computed, as shown in Fig. 3.15b. Notably, normalized cross-correlation decreases with the channel estimation error [dB], reaching a value of 0.78 for an error of 5 [dB]. Thus, cross-correlation error (i.e., vertical error bars) increases with channel estimation error.

2. **Data Rate and Capacity**

As shown in Eqs. 3.10 and 3.11, the stronger transmitter's data-rate may have to be lower than that of the weaker transmitter to ensure better SIC performance. Data-rate R_1 for user 1 was set to 5 Mbps, and data-rate R_2 for user 2 to 100 Mbps, with power ratio fixed to 0.33. Data-rate for user 2 was varied with a 100 Mbps step until 500 Mbps was reached. A data-rate difference ranging from 95, 195, 295, 395, and 495 Mbps was exploited. For each data acquisition, SIC was performed. NRMSE was computed between reconstructed signals and original transmitted signals, as shown in Fig. 3.16a. As expected, NRMSE was higher for user 2 because it is the weaker signal of the two. Increasing bit rate difference causes a slight increase in NRMSE. Notably, the increased error is too insignificant to claim it is the result of data difference variation. It is more likely that the increasing error is due to the limitations of hardware devices (e.g., oscilloscope bandwidth [1 GHz]), given an increasing communication speed. NOMA proved to outperform OMA techniques for simulations presented in [54],[55]. Experimental validation of achievable data-rate was performed. Fig. 3.16b shows the empirical cumulative distribution function (CDF) of the achievable system data-rate [bps/Hz]. The green line represents the achievable sum data-rate with NOMA, as expressed in Eq. 3.12, and the magenta line represents achievable data-rate without NOMA, as expressed in Eq. 3.13. Without NOMA, either user 1 or user 2, but not both, can transmit in a given time frame, for successful detection. Achievable data-rate is given by the maximum between the users 1 and 2. Thus, achievable data-rate is greater with NOMA than without it.

3.3 Limitations

ICA, NOMA, and signal subtraction [98] proved to successfully and accurately support high data-rate multi-user FSOC. However, these techniques were tested separately with various experimental setups and each one posses limitations and assumptions that do not allow us to generalize obtained results to a wide range of scenarios. NOMA assumes that the mixing matrix A is non-singular and square, leading to an assumption of the same

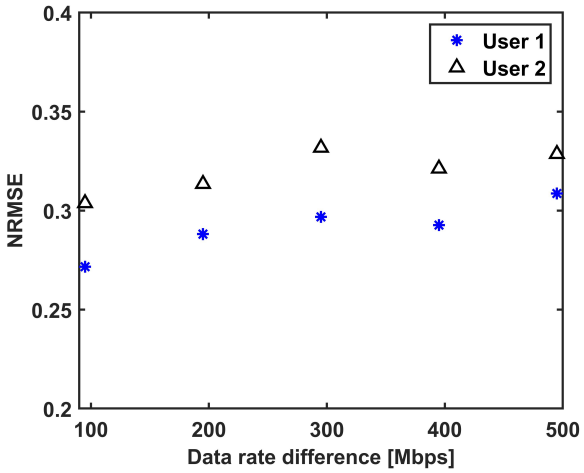

(a) Data rate

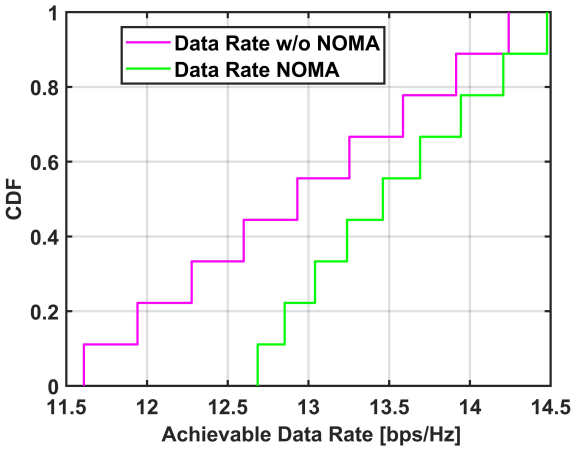

(b) CDF of achievable system data rate

Figure 3.16: Data rate and system capacity analysis

number of transmitters and receivers. SIC for NOMA requires CSI at the receiver to correctly reconstruct transmitted signals. Therefore, to overcome presented O-MAC techniques limitations (e.g., required CSI, identical number of transmitters and receivers) and to satisfy various transmitters' and receivers' configurations, and to consider potential CSI availability at the receiver side, combinations of the various O-MAC techniques were proposed and experimentally evaluated. Four demodulation methodologies were tested, evaluated, and compared: ICA and NOMA, hereafter referred as I+N; ICA and signal subtraction, as I+S; NOMA application on one received mixed signal, as N1; and NOMA application on two received mixed signals, as N2.

3.3.1 Experimental Setup

The experimental setup reported in this dissertation, shown in Fig. 3.17, is composed of three independent, optical transmitters and a dual-path fiber bundle receiver. In the block diagram in Fig. 3.17, the black solid lines used to connect the blocks represent the electrical links; the gray solid lines represent the optical fiber connections and the dashed lines represent the free space optical links. The optical sources consisted of three electrical-to-optical converters with fiber-coupled laser diodes operating at the three optical transmission windows wavelengths, namely 1550 nm, 1310 nm, and 850 nm. Intensity

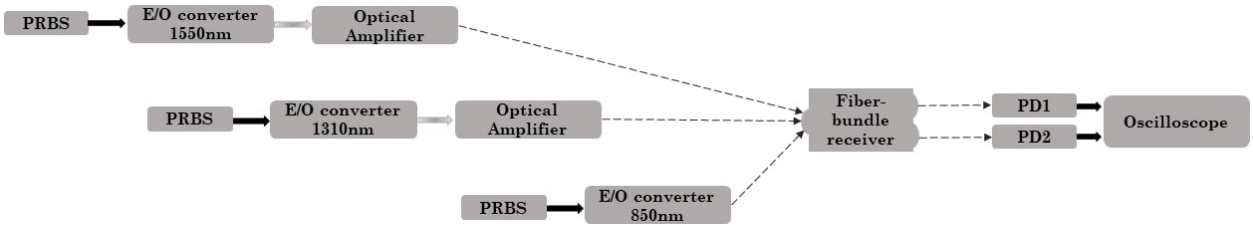

Figure 3.17: Depiction of the experimental setup

Modulation (non-return-to-zero [NRZ-OOK]) with Direct Detection (IM/DD) scheme was employed for transmission. These laser sources were directly modulated by three independent PRBS that were $2^{31} - 1$ bits in length. Various bit rates were tested. The 1550 nm optical output was connected to a doped fiber optical amplifier, and the 1310 nm to a semiconductor optical amplifier. No amplification was performed on the 850 nm signal. Output power of each source was coupled to an optical telescope to collimate the propagating beams to the receiver. The dual-path fiber bundle receiver, shown in Fig. 3.18, was composed of a hexagonal array of 19 small lenses (e.g., focal length of 3 mm) that coupled the signal in an array of 19 multi-mode fibers (e.g., core diameter 400 /*mu*m and numerical aperture of 0.37) [36]. The fibers split into two paths (i.e., 10 fibers in one path and 9 in the other path); and then, fibers transmitted the signals to an array of graded index lenses, which collimated the optical signals in two aspheric lenses (focal length of 20 mm and diameter of 25.4 mm). Outputs from the arrays were focused to the collecting area of two photodetectors: Thorlabs PDA10CF (PD1) and PDA015C (PD2). A 10[°] wedge prism was placed in front of the receiving lens array to vary the angle between the optical signals received by photodiode one and two. Transmitter beam diameters were adjusted such that optical power of 1550 nm and 1310 nm lasers sources coupled efficiently into photodetectors PD1 and PD2 and optical power of 850 nm laser source coupled efficiently into only photodetector PD2. A National Instruments Virtual Bench oscilloscope with sampling rate of 1 GSample/s was used to record data collected from the two photodetectors and the transmitted PRBS. Data processing was performed off-line using MATLAB Software and the available Statistical and Machine Learning MATLAB Toolbox.

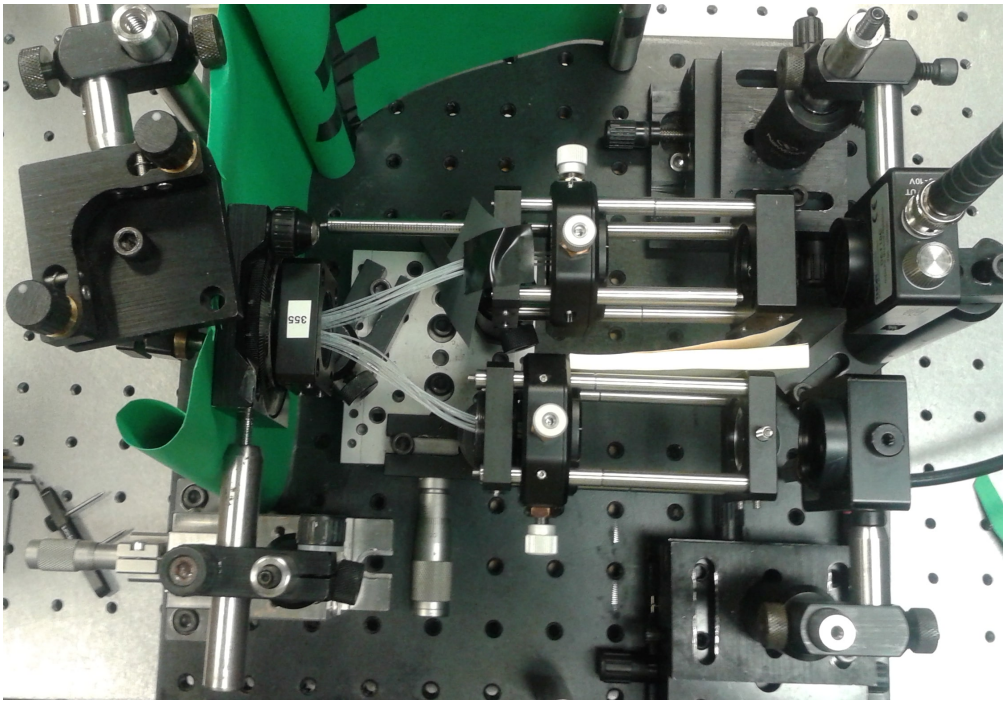

Figure 3.18: Fiber-bundle receiver

3.3.2 Results

Static power allocation scheme was employed, and two data-rate case scenarios were analyzed: users with same data-rate (i.e., $R_1 = R_2 = R_3 = 150kb/s$) and users with different data-rate (i.e., $R_1 = 110kb/s, R_2 = 130kb/s, R_3 = 150kb/s$). An example of transmitted and received mixed signals is shown in Fig 3.19a and 3.19b for users with a different data-rate and 3.19c and 3.19d for users with the same data-rate. In Fig. 3.19a and 3.19c, the green, blue, and orange lines represent the transmitted PRBS from TX1, TX2, and TX3, respectively. In Fig. 3.19b and 3.19d, the blue and red lines represent the received mixed signals at RX2 and RX1, respectively. Multi-user detection on the received signals was performed using four methods: I+N, I+S, N1 on RX2, and N2 on both RX1 and RX2. These combinations were tested to evaluate the best method for performing multi-user communication and to consider potential CSI available at the receiver side. In the event that no CSI is available, I+S can be used. In the event that CSI for one user is available at one receiver, I+N can be used. In the event that CSI of all users is available at only one receiver, N1 can be used. Finally, in the event that CSI of all users is available

at both receivers, N2 can be used. For each tested method, 10 acquisitions were collected. Separation performances were measured using cross-correlation (i.e., mean and standard deviation) between reconstructed signals and their corresponding transmitted sequences.

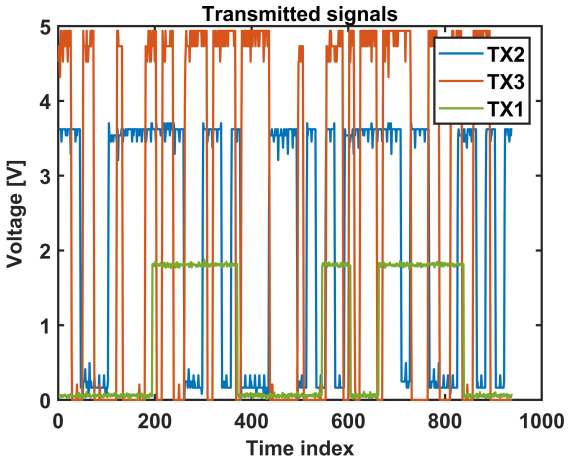

(a) Transmitted signals different data rate

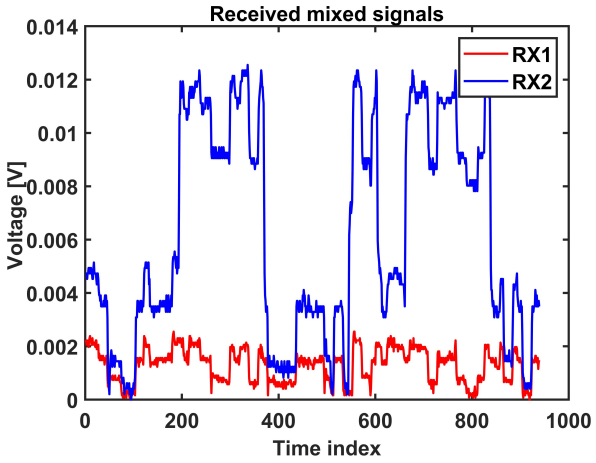

(b) Received mixed signals different data rate

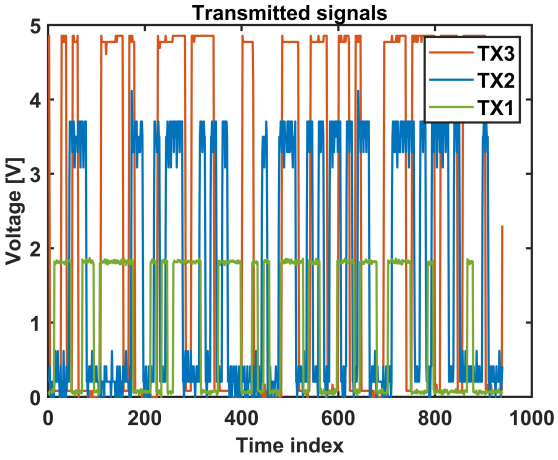

(c) Transmitted signals same data rate

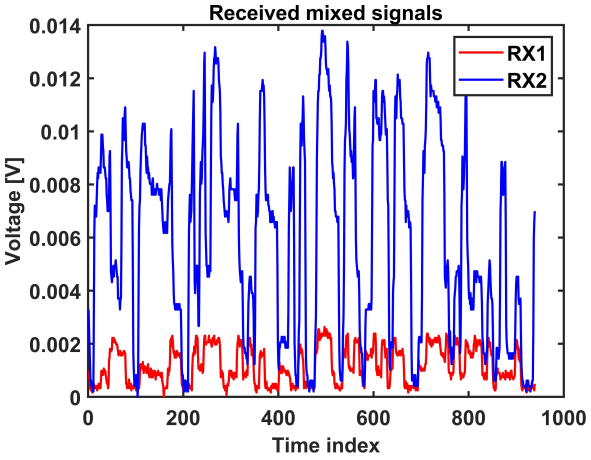

(d) Received mixed signals same data rate

Figure 3.19: Examample of transmitted and received signals

1. **ICA+NOMA**

   A FastICA algorithm was performed on received signals RX1 and RX2 to extract the first two transmitted signals TX1 and TX2. Although the signals were accurately decoded, some interference from the other users was observed. Next, having CSI of user 2 at RX1, SIC was performed to detect user 3. Thus, user 2 was re-modulated and subtracted from RX1 received mixed signal, as in Eq. 3.9. Mean and standard

deviation of the computed cross-correlation for the three users are shown in the boxplot in Fig. 3.20a for different data-rate and Fig. 3.20b for same data-rate. High values of cross-correlation were obtained for all users. For example, in Fig. 3.20a a cross-correlation of 0.99 was obtained for user 1; 0.98 for user 2; and 0.91 for user 3. Hence, this combination of two methods proved to perform multi-user detection with high accuracy.

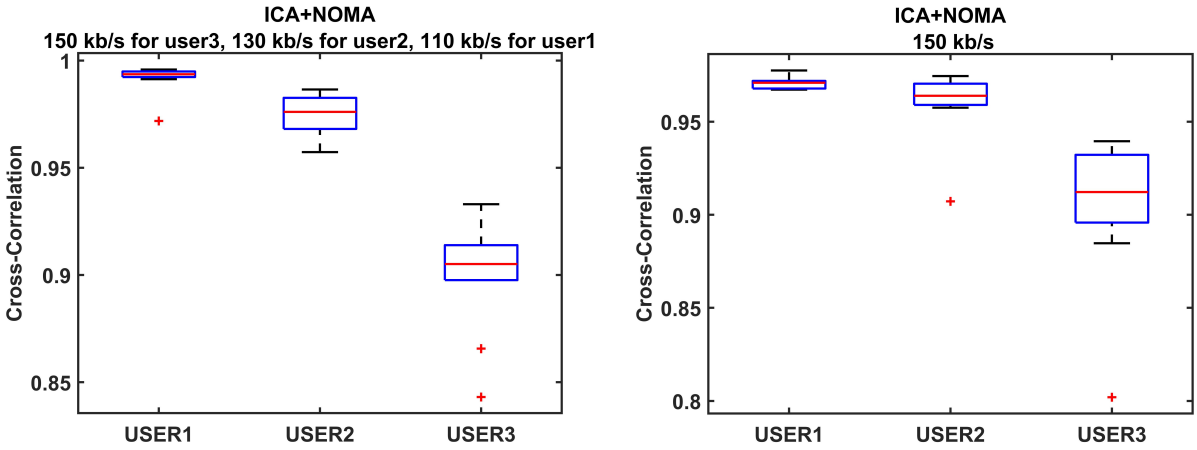

(a) Different data rate

(b) Same data rate

Figure 3.20: ICA+NOMA: Cross-correlation

2. ICA+SUBTRACTION

Unlike the previous method, I+S doesn't require CSI to detect user 3. Again, FastICA was first performed on the received mixed signals RX1 and RX2 to decode the two transmitted sequences TX1 and TX2. Next, Z-scores normalization (i.e., $ZS = (x - \mu)/\sigma$, with μ mean vale and σ standard deviation of signal x) [99] was performed on the received signal RX1 and on the reconstructed signal from user 2. Normalized reconstructed sequence TX2 was then subtracted from normalized RX1, resulting in a signal from user 3. Fig. 3.21 illustrates mean value and standard deviation of cross-correlation for the three users. High values of cross-correlation were obtained for all users and all data-rate scenarios. For example, in Fig. 3.21a, a cross-correlation of 0.99 was obtained for user 1, 0.98 for user 2 (like that in I+N), and 0.88 for user 3.

It is clear that, even without CSI, good accuracy reconstruction was achieved for all users.

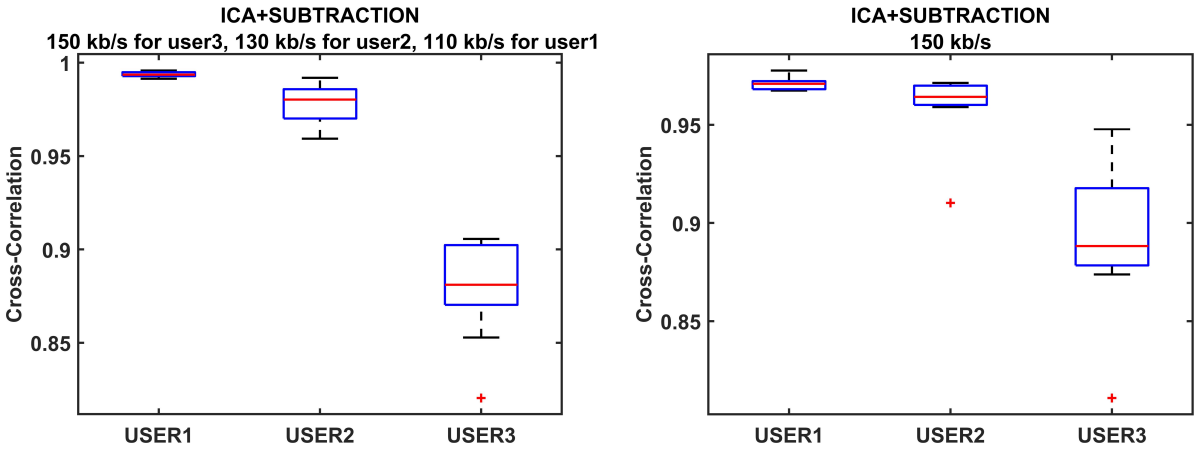

(a) Different data rate

(b) Same data rate

Figure 3.21: ICA+SUBTRACTION: Cross-correlation

3. **NOMA**

SIC was utilized at the receiver side for user decoding with two approaches: N1 using only the mixed signal RX2 (i.e., to decode the three users) and N2 using both received mixed signals (i.e., RX2 to decode user 1 and RX1 to decode user 2 and 3). The first approach required CSI of user 1 and 2 at receiver RX2; the second approach required CSI of user 1 at receiver RX2 and of user 2 at RX1. Once CSI was known, signal demodulation was performed for both approaches. Fig. 3.22 illustrates mean value and standard deviation of cross-correlation for the three users with different data-rate (See Fig. 3.22a) and with same data-rate (See Fig. 3.22b) when only RX2 is used in the demodulation process. Cancellation errors, which are a substantial drawback in NOMA, will propagate during the demodulation process, decreasing reconstruction accuracy. For example, in the event that different data-rate for user 1 and user 2, cross-correlation greater than 0.95 is obtained and for user 3, cross-correlation is 0.8. Performance when users have same data-rate worsen; in particular, cross-correlation for user 3 is around 0.5.

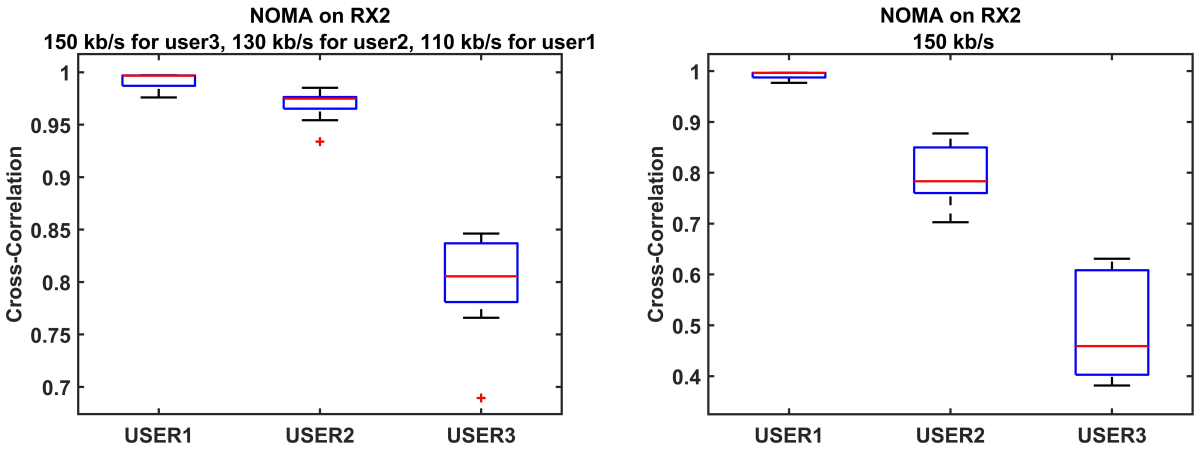

(a) Different data rate (b) Same data rate

Figure 3.22: NOMA1: Cross-correlation

Fig. 3.23 shows mean value and standard deviation of cross-correlation for the three users with different data-rate, 3.23a; and with same data-rate, 3.23b, when both the received signals RX1 and RX2 are used. Unlike previous results, accurate reconstruction was obtained for all users with cross-correlation greater than 0.9 for both scenarios.

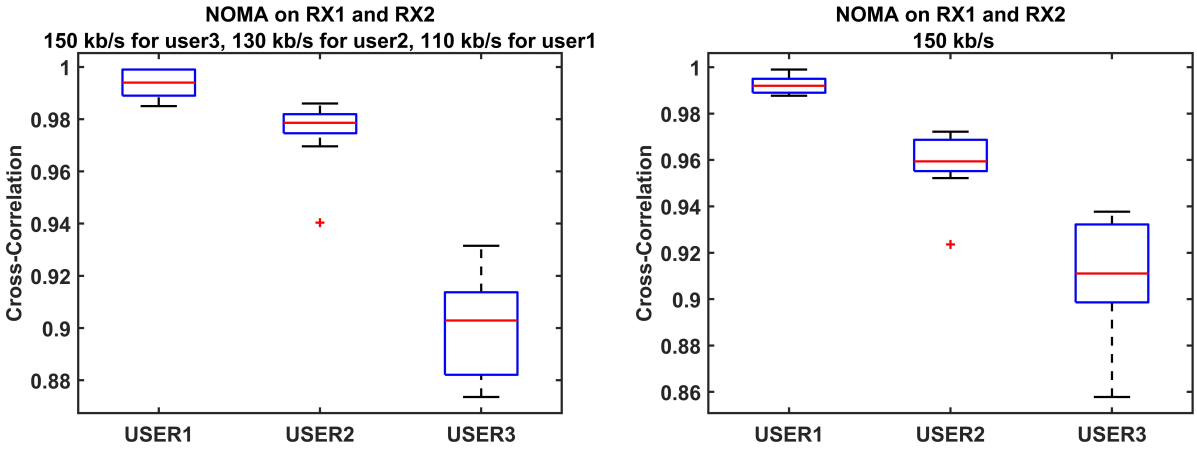

(a) Different data rate (b) Same data rate

Figure 3.23: NOMA2: Cross-correlation

3.3.3 Discussion

Accuracy reconstruction of the three users was evaluated for each tested method. Subsequently, a comparison between diverse combinations is analyzed for each user. Fig.

3.24 shows mean cross-correlation versus decoded users with a different data-rate, 3.24a; and the same data-rate, 3.24b. The blue bars represent results for I+S; orange bars I+N; yellow bars N1; and purple bars N2.

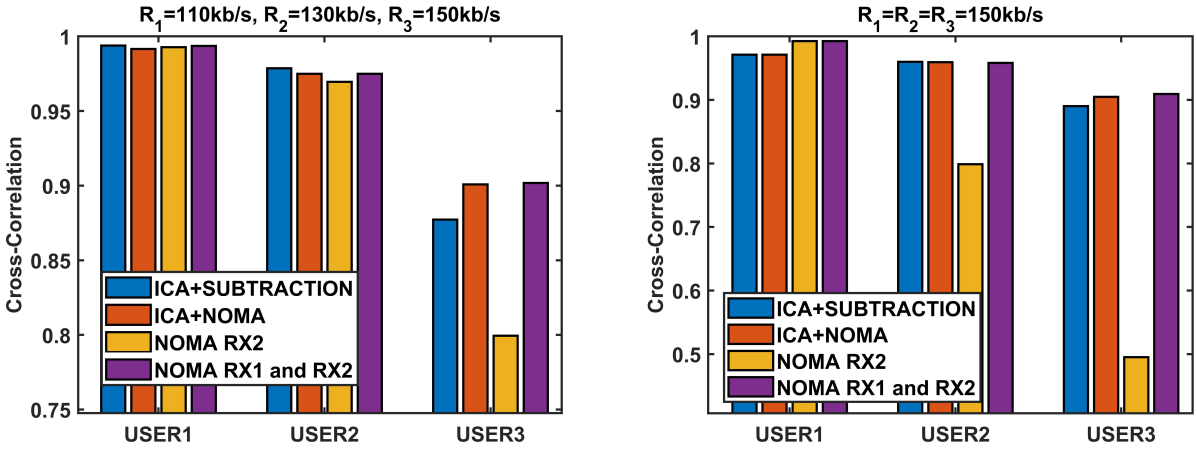

(a) Different data rate

(b) Same data rate

Figure 3.24: Cross-correlation versus users

User 1 was reconstructed with high accuracy in all cases—a cross-correlation close to 1 was obtained. User 2 was reconstructed with cross-correlation greater than 0.95 when users had a different data-rate; all the tested methodologies proved high accuracy. When users had the same data-rate, user 2 was well reconstructed with high value of cross-correlation, except when N1 was employed. In this scenario, a decreased cross-correlation was observed. User 3 was reconstructed with good accuracy (i.e., cross-correlation of 0.9) with N2 and with I+N combination. Slightly lower performances were obtained when I+S was used; cross-correlation was just below 0.9. Low accuracy for user 3 was obtained when N1 was computed. For example, when users had the same data-rate, a cross-correlation of 0.5 was measured. This means that user accuracy reconstruction decreases with the order of demodulation for all studied techniques. Overall system accuracy was calculated to evaluate which multiple access technique guaranteed the optimal signal separation performance. Fig. 3.25 shows the mean cross-correlation of all three users under the four detection methods tested. The blue lines represent users with the same data-rate, and orange lines represent users with different data-rate. The highest accuracy for signal reconstruction was

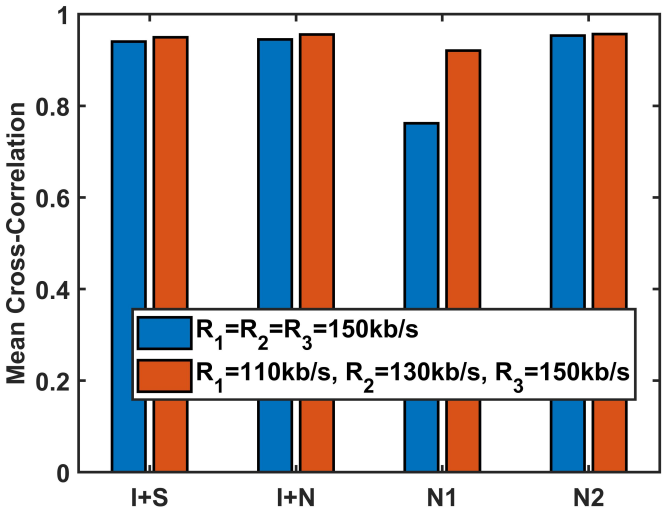

Figure 3.25: Mean cross-correlation between users

achieved from N2. In fact, propagation error resulted on only the third user. Notably, CSI was required at both receivers. Although NOMA (i.e., N2) proved to be the best O-MAC technique, it is important to recognize that is also the most computationally complex (i.e., determining real-time SIC). I+N and I+S proved to have similar performances in terms of mean cross-correlation. I+N requires CSI at one receiver. I+S's advantage is that it doesn't require knowledge about channel or transmitted powers. Ultimately, N1 performed poorly, particularly for users with the same data-rate. Given that SIC was performed on the same signal for extracting all three users, cancellation errors propagated in the demodulation process for both user 2 and user 3. Furthermore, while the other three techniques employed both received signals to decode transmitted sequences, N1 used information from only one signal. Three of the studied optical multiple access techniques successfully supported multi-user FSOC.

CHAPTER 4

COGNITIVE O-PHY

Multi-user FSOC networks are expected to face increased system complexity and need for flexibility and heterogeneity in terms of supported services, applications, devices, and transmission technologies. Such networks should be capable of dynamically adjusting, transmitting, and receiving parameters, such as spectrum allocation, modulation format, and symbol rates, to name just a few, for satisfying systems and user requirements. Cognitive FSOC networks with autonomous and intelligent configuration and operation capabilities constitute a remarkable solution to tackle this increased system complexity. Several ML-based methodologies for embedding intelligence into the system at the PHY layer have been proposed, developed, and experimentally validated.

4.1 User Discovery Algorithm

Proposed O-MAC techniques (i.e., ICA, NOMA, and combination thereof) assume that the number of transmitting users is known at the receiver side for properly selecting the most suitable method to accurately decode multiple users. However, this phenomenon does not necessarily hold true in real and dynamic communication scenarios where communicating users are mutually independent and result in random user add/drop. Thus, to adaptively select the proper O-MAC technique (or combination of several) for performing multi-user FSOC, cognition should be embedded at the receiver side (i.e., ability to identify some PHY information as the number of transmitting users). Using unsupervised ML for detecting the number of transmitting users is proposed to perform real-time, dynamic and autonomous O-MAC technique selection.

4.1.1 Methodology

NRZ-OOK modulation was adopted as the modulation scheme in the study reported in this dissertation. OOK is a binary level modulation format widely used in FSOC due to its simplicity and high-power efficiency [12].When employing OOK with one user, two possible optical outputs are expected: P_T (transmitted power) when "1" is transmitted and $\alpha_e P_T$ (α_e= optical source extinction ratio $0 \leq \alpha_e \leq 1$) when "0" is transmitted [100]. With N users transmitting simultaneously, there will be $k = 2^N$ possible optical power outputs. Hence, k power levels will be detected at the receiver side. Conversely, if k power measurements are detected, it is possible to retrieve the number of transmitting users as $N = log_2 k$. The research reported herein proposes using unsupervised learning (i.e., clustering techniques) to extract power levels from the received mixed signals, and then calculating the number of broadcasting users. The steps carried out in this proposed methodology are shown in Fig. 4.1. Data pre-processing was required to compute the number of expected clusters as input to clustering algorithms. Four clustering methods (e.g., K-mean, K-medoid, hierarchical, and fuzzy) were subsequently evaluated [101]. Moreover, a weighted clustering was developed to correct user underestimation when received amplitudes a) were of equal power and b) equality $N = log_2 k$ was no longer valid. Although cases with one, two, and three transmitting users were analyzed, only three-user case scenario results will be shown hereafter. Before applying clustering algorithms, some data pre-processing was required to

Figure 4.1: Proposed methodology

make raw data suitable for the analysis, and some data post-processing was necessary to extract useful information for computing and analyzing the results.

1. **Data Pre-Processing**

Noise reduction on the collected data was performed. A third-order median filter was applied on the received mixed signals to remove impulsive noise resulting from electrical devices or communication transmission [102]. Fig. 4.2a shows an example of de-noised, received mixed signal when three users are simultaneously transmitting. Then, since the goal was to detect power levels (i.e., constant power values) of transmitting users, low frequency components of the received signal (i.e., amplitude values that are changing slowly or slightly with time) were considered. Numerical differentiation of the de-noised received signal was performed, and the high- and low-frequency components of the data were extracted, as in Eq. 4.1. Standard deviation of the first derivative of the received signal, shown in Fig. 4.2b, was set as a threshold.

$$y(n) = \begin{cases} y_{LF}[n], & if \left(\frac{dy[n]}{dn}\right) < std\left(\frac{dy[n]}{dn}\right) \\ y_{HF}[n], & if otherwise \end{cases} \tag{4.1}$$

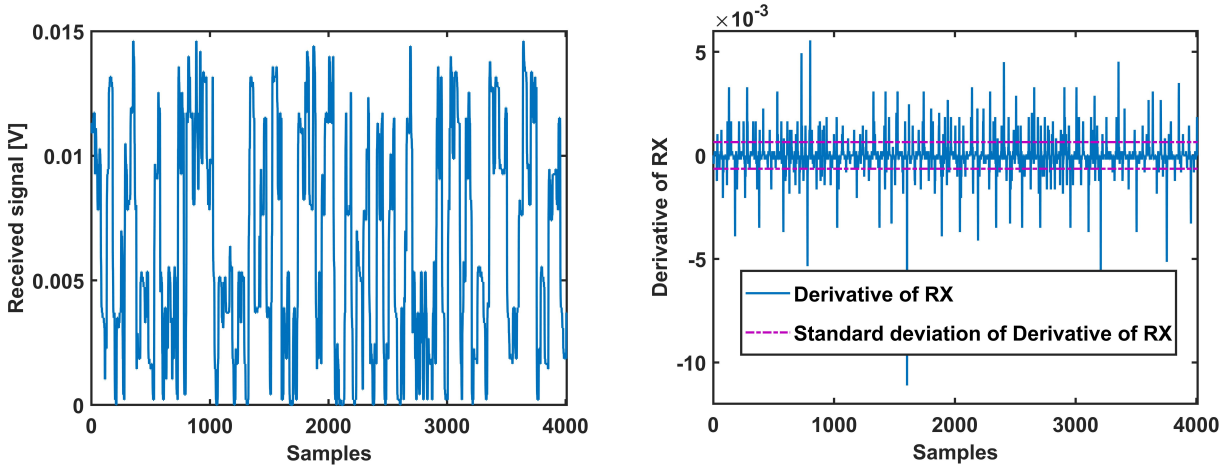

(a) Received mixed signal

(b) Derivative of received mixed signal

Figure 4.2: Pre-processing steps

Low frequency components of the signal $y_{LF}[n]$ (i.e., samples whose derivative values are within its standard deviation) were considered for pre-processing analysis. To extract power levels, the occurrence of the low frequency components of the signal were measured, and the empirical 1-D histogram $H_L[y_{LF}]$ was computed, as illustrated

in Fig. 4.3a. Then, local maxima of the $H_L[y_{LF}]$ were calculated, as detailed in Eq. 4.2, to perform peak detection as shown in Fig. 4.3b.

$$\arg\max_{y_{LF}} H_{LF}[y_{LF}] = p_m \tag{4.2}$$

p_m is the peak position with the integer $m \in$[1, number of detected peaks]; the number of peaks in the histogram was expected to be $m = k = 2^N$. Accordingly, the number of detected peaks was provided as input for the clustering algorithms as the number of expected clusters. In this case, $m = 8$ was obtained, as shown in Fig. 4.3b.

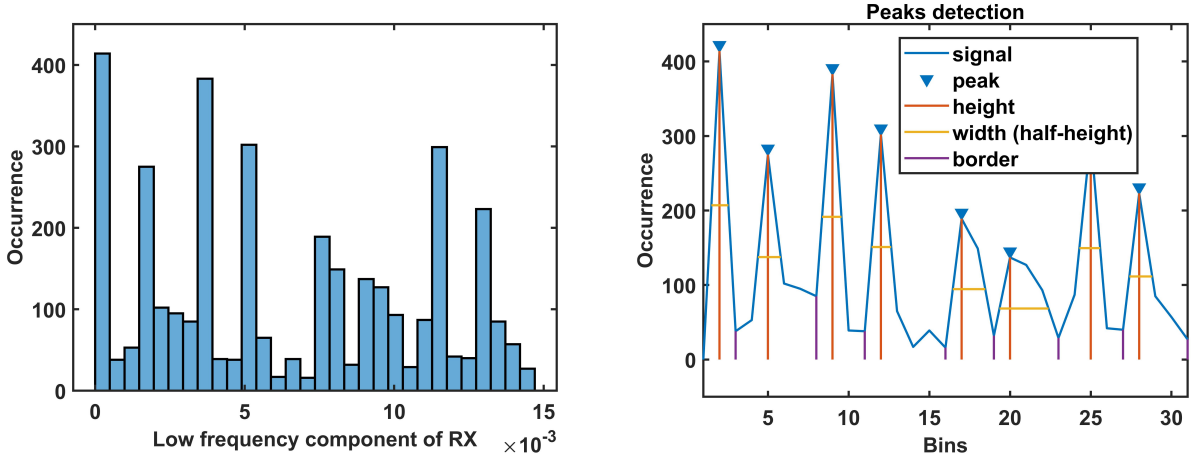

(a) 1-D histogram $H_{LF}[y_{LF}]$ (b) Peak detection of $H_{LF}[y_{LF}]$

Figure 4.3: Pre-processing steps

2. **Weighted clustering**

As previously mentioned, clustering algorithms were tested (e.g., K-means, K-medoids, hierarchical and fuzzy). Given that a power allocation scheme is not employed, and more than one user with the same power is collected at the receiver side, overlapping of received signals in the power domain will occur. In fact, when two users are received with the same power, both will be clustered together, leading to an under-estimation of user number. T o evaluate if more than one signal is overlapped in each cluster,

each cluster is assigned a weight ρ_i, defined as:

$$\rho_i = \frac{L_i}{L}, \quad 1 \leq i \leq K \tag{4.3}$$

where L is the total number of samples of the processed data; L_i is the number of samples belonging to cluster i; and K is the total number of obtained clusters. Thus, weights ρ_i will satisfy the following conditions: $\sum_{i=1}^{K} \rho_i = 1$ and $0 < \rho_i \leq 1$. As previously mentioned, with N transmitting users, $k = 2^N$ possible output powers are expected. Assuming that the probability of transmitting a 1 or a 0 is equally likely per user, the probability of each possible output E_l with $1 \leq l \leq k$ is equal to $P(E_l) = \frac{1}{k} = \frac{1}{2^N}$. Thus, the expected weight $\hat{\rho}_i$ for each cluster given there is no power overlap and $k = K$ and $1 \leq i \leq K$ and $1 \leq l \leq k$, is expressed as:

$$\hat{\rho}_i = \rho_i = P(E_l) = \frac{1}{2^N} \tag{4.4}$$

If multiple signals are overlapped in the clusters, the equality in Eq. 4.4 no longer holds true. Since the probability of all users concurrently transmitting 0 is $P(E_1) = \frac{1}{2^N}$ besides their transmitting power, the reference weight $\hat{\rho}_i$ is defined as :

$$\hat{\rho}_i \approx P(E_1) = min{\rho_i}_{i=1}^{K} \tag{4.5}$$

To identify the number of signals hidden in each cluster, overlapping parameter λ_i was introduced and is defined as:

$$\lambda_1 = \left[\frac{\rho_i}{\hat{\rho}_i}\right], \quad 1 \leq i \leq K \tag{4.6}$$

Parameter λ_i should satisfy the following conditions:

$$\sum_{i=1}^{K} \lambda_i = k = 2^N, 1 \leq \lambda_i \leq 2^N \tag{4.7}$$

4.1.2 Experimental Setup

The experimental setup illustrated in Section 3.3.1 was employed in the analysis. Output signals from both photodetectors were used for analysis.

4.1.3 Results

Validation of the proposed methodology was performed on one-user, two-user, and three-user scenarios. Users with both the same and different power values were tested. For the sake of conciseness, only the following three-user scenarios are illustrated: 1) three users with different power; 2) three users with same power; and 3) three users two of which have same power.

1. **Three users different power**

   Transmitted power was tuned to assure three users arrived at the fiber-bundle receiver with different power levels. Fig. 4.3a shows that the number of detected peaks in the 1-D histogram function is $m = 8$. Hence, "8" is used as input for the clustering algorithms as the number of maximum expected clusters. Results of the clustering techniques are shown in 4.4, where red markers represent cluster centroids. Fig. 4.4a shows the obtained clusters for fuzzy, 4.4b for hierarchical, 4.4c for K-medoid, and 4.4d for K-means clustering.

   All algorithms produced similar results, namely the ability to identify the same clusters. Fig. 4.5 shows obtained cluster centroids (See red markers in Fig. 4.4) and the histogram peaks values versus the number of clusters. Results illustrate that the clustering centroids and the histogram peak values match with only a very small error. However, before defining the number of users, each cluster was assigned a weight ρ_i with $1 \leq i \leq 8$ for evaluating if signals are hidden. Cluster weights versus identified clusters obtained for each algorithm are illustrated in the 4.6a bar graph. Blue bars show results from fuzzy clustering; orange show hierarchical; yellow represent K-medoids; and purple represent K-mean clustering. All bars have comparable cluster heights. Accordingly, similar weights ranging from 0.1 to 0.15 were obtained. Moreover, by observing

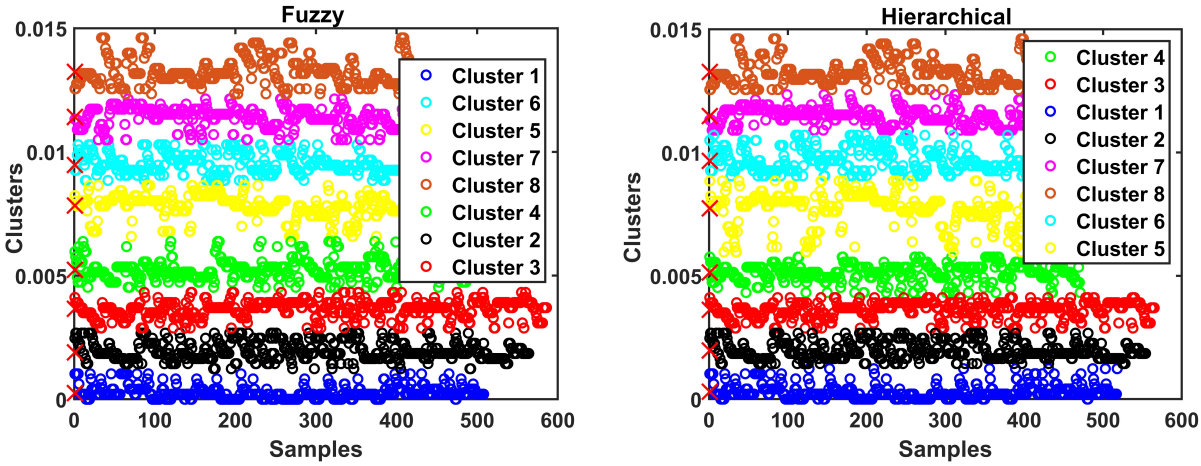

(a) Fuzzy

(b) Hierarchical

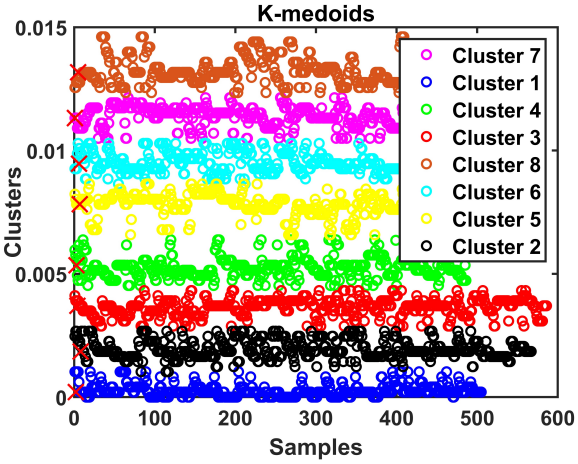

(c) K-medoids

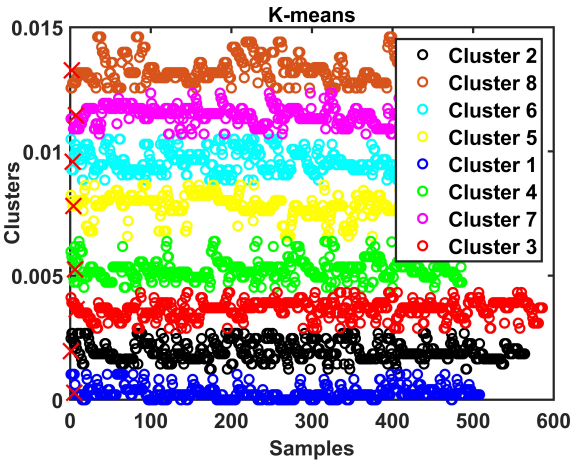

(d) K-means

Figure 4.4: Clustering results

produced weights for each cluster, it was concluded that all algorithms performed in a similar way. Reference weight $\hat{\rho}_i$ was set as expressed in Eq. 4.5, and the obtained overlapping parameter λ_i where $1 \leq i \leq 8$ were calculated. Results are shown in 4.6b. The illustration shows that each cluster has an overlapping parameter equal to one and that all transmitting users have different powers. Given Eq. 4.7, $\sum_{i=1}^{8} \lambda_i = \sum_{i=1}^{8} 1 = 8$ were obtained. Knowing that $8 = 2^N$ and that $\lambda_i = 1$ for $1 \leq i \leq 8$, we can conclude that the number of received users is equal to $N = log_2 8 = 3$.

2. **Three users two with same power**

Transmission power of the laser sources were tuned, such that at the receiver side

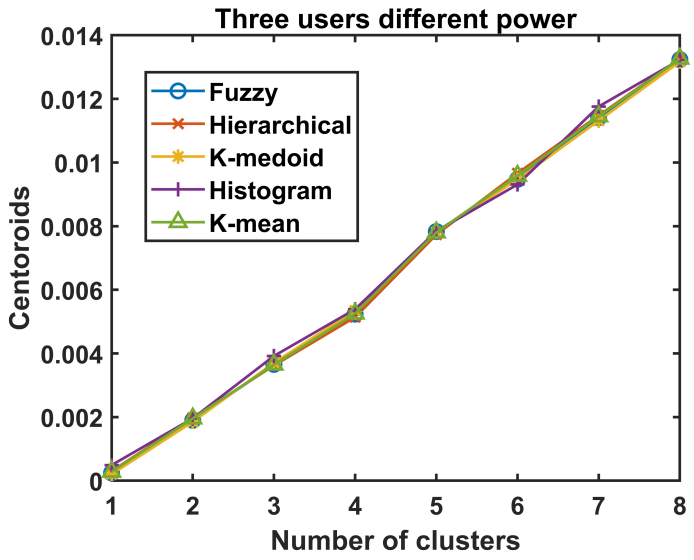

Figure 4.5: Clusters centroids

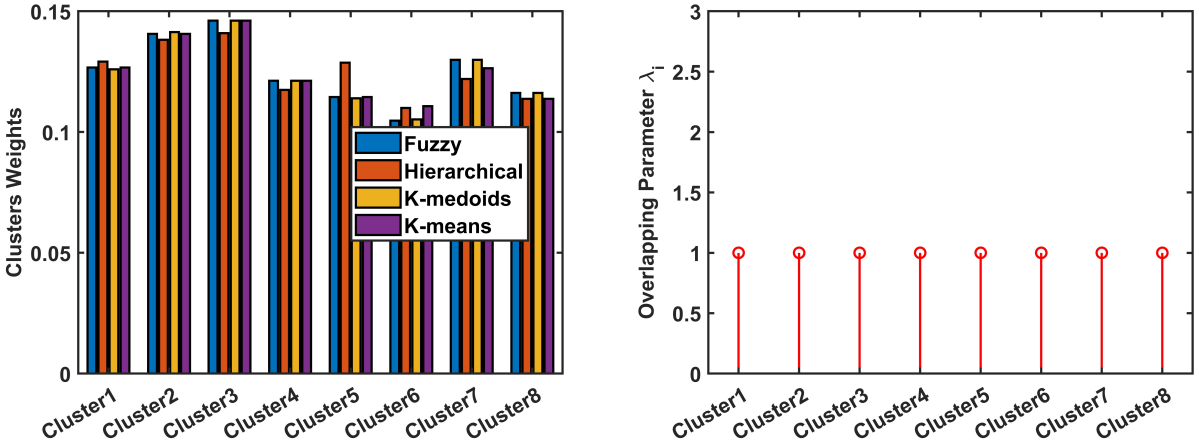

(a) Cluster weight ρ_i

(b) Overlapping parameter λ_i

Figure 4.6: Number of users calculation

two users were received with same power values and the third user with a different power value. Peak detection of the 1D empirical histogram function $H_L[y_L F]$ was performed, and the number of detected peaks in the histogram was $m = 6$. This parameter was provided as input to the clustering algorithms as the number of expected clusters. Results of clustering techniques are shown in 4.7. Specifically, Fig. 4.7a shows the obtained clusters for fuzzy, 4.7b for hierarchical, 4.7c for K-medoid, and 4.7d for K-means clustering. Results in 4.8 illustrate that all clustering algorithms had comparable results and that the cluster centroids matched with peak values obtained

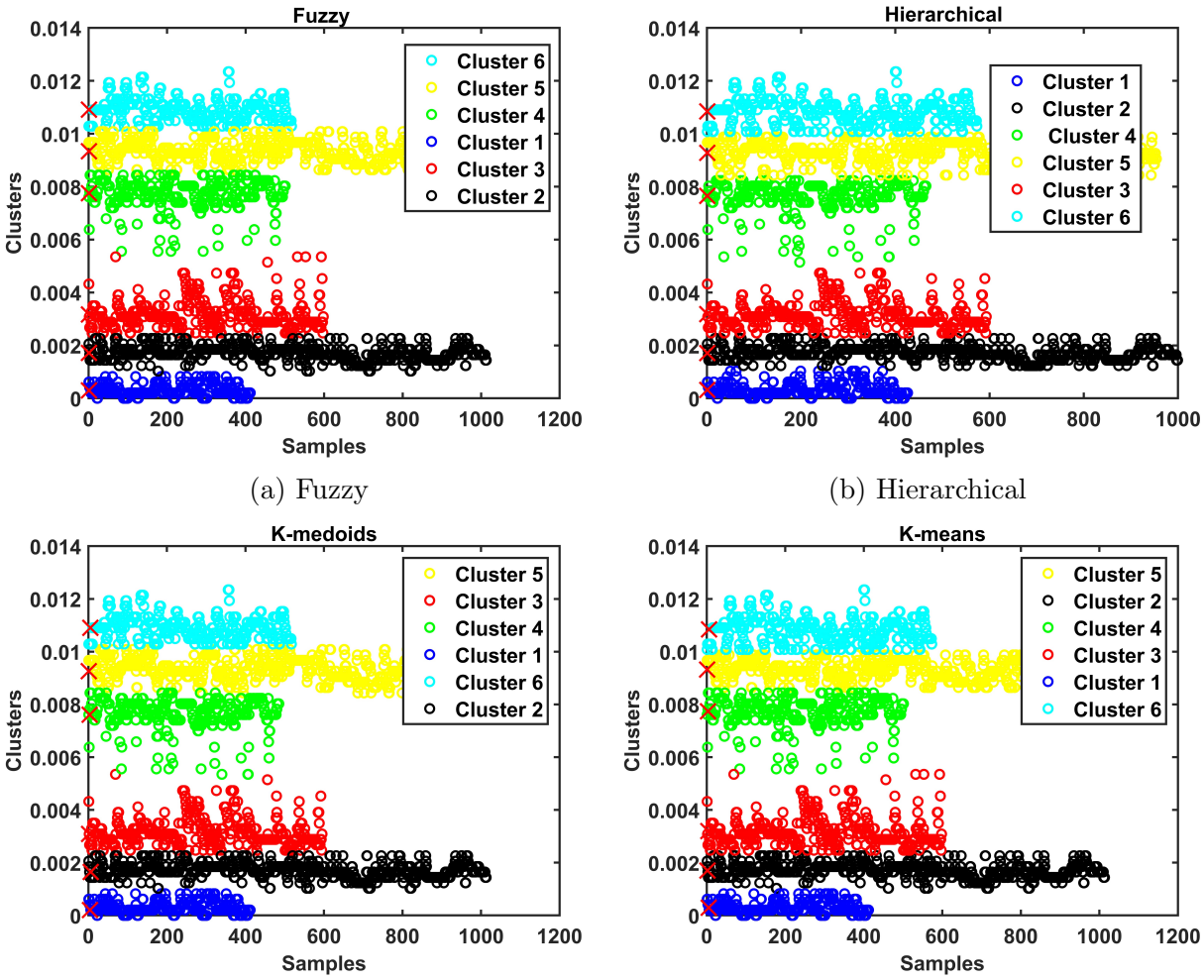

(a) Fuzzy

(b) Hierarchical

(c) K-medoids

(d) K-means

Figure 4.7: Clustering results

from the histogram. Two clusters have a greater number of samples. Accordingly, an overlapping of more than one signal is highly likely. Cluster 2 (See black markers) and cluster 5 (See yellow markers) have a higher number of samples when compared with other clusters. Eq. 4.6 suggests that clusters 2 and 5 should outweigh other clusters. Weight analysis was performed and obtained weights for each cluster are shown in 4.9a. Blue bars indicate results for fuzzy clustering; orange for hierarchical; yellow for K-medoids; and purple for K-mean clustering. All clusters had similar weights, ranging from 0.1 to 0.15, except for clusters 2 and 5, which had greater weights (e.g., 0.25). The overlapping parameter λ_i, where $1 \leq i \leq 6$, was computed (See 4.9b). Results indicate that $\lambda_2 = 2$ and $\lambda_5 = 2$, while $\lambda_i = 1$, meaning that two signals present in clusters 2

and 5 are hidden. Thus, from Eq. 4.7, $\sum_{i=1}^{6} \lambda_i = 1+2+1+1+2+1 = 8$. Knowing that $8 = 2^N$, $\lambda_2 = 2$, and $\lambda_5 = 2$, we can conclude that the number of broadcasting users is equal to $N = log_2 8 = 3$ and that two users are transmitting with the same power.

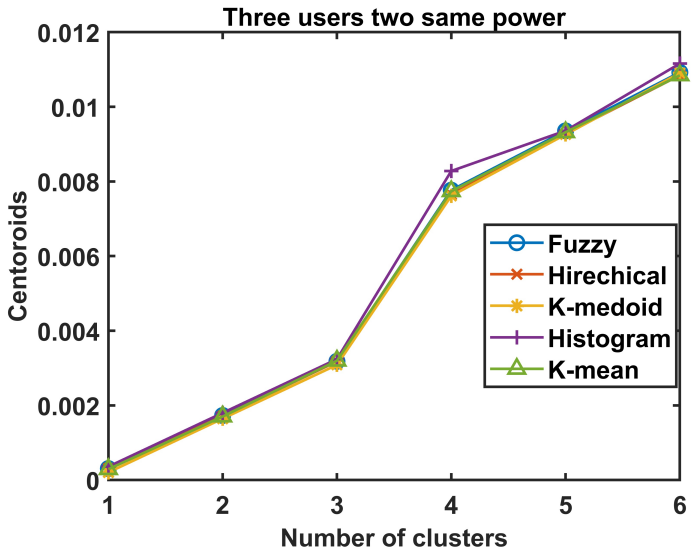

Figure 4.8: Clusters centroids

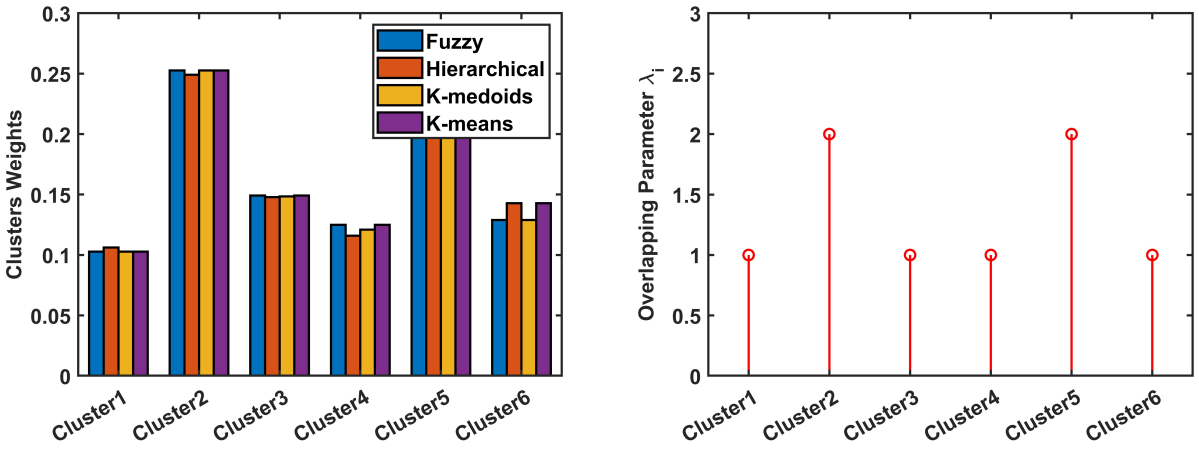

(a) Cluster weight ρ_i (b) Overlapping parameter λ_i

Figure 4.9: Number of users calculation

3. **Three users same power**

Finally, given a case where all received users had the same power, clustering algorithms were able to identify four expected clusters from the peak detection analysis. Fig.

4.10a shows the obtained clusters for fuzzy, 4.10b for hierarchical, 4.10c for K-medoid, and 4.10d for K-means clustering. Fig. 4.11 shows that all cluster centroids match

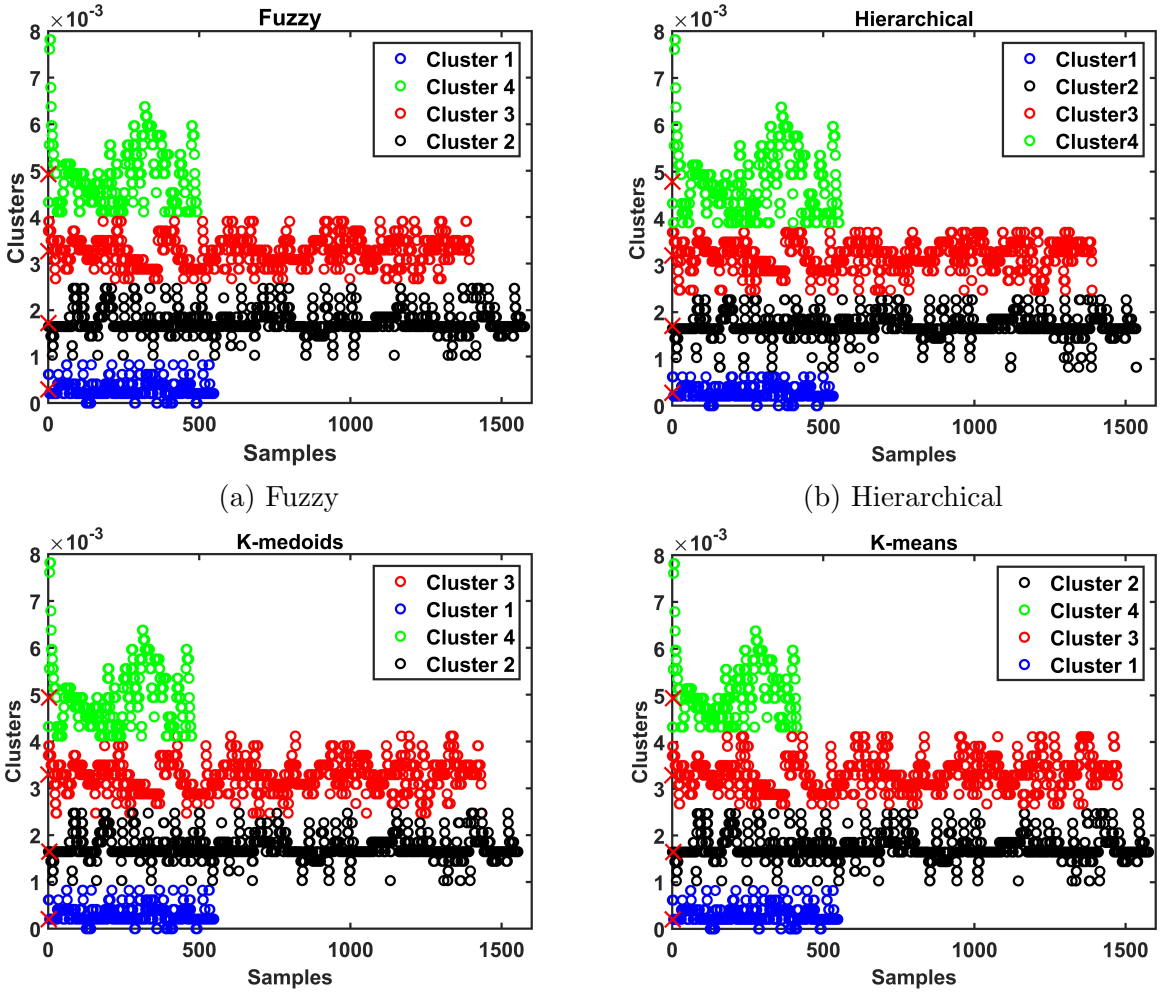

(a) Fuzzy

(b) Hierarchical

(c) K-medoids

(d) K-means

Figure 4.10: Clustering results

extremely well with peak location values obtained in the histogram. Given cluster weights illustrated in Fig. 4.12a, we can observe that cluster 2 (See black markers) and cluster 3 (See red markers) outweigh the other two clusters with weights ranging from 0.35 to 0.4. The calculated overlapping parameter λ_i where $1 \leq i \leq 4$ is shown in Fig. 4.12b. Notably, $\lambda_2 = 3$ and $\lambda_3 = 3$, while $\lambda_1 = 1$ and $\lambda_4 = 1$, meaning that three signals are hidden in clusters 2 and 3. From Eq. 4.7, we obtained $\sum_{i=1}^{4} \lambda_i = 1+3+3+1 = 8$. Hence, knowing that $8 = 2^N$, $\lambda_2 = 3$, and $\lambda_3 = 3$, it can be concluded that the number of users was equal to $N = log_2 8 = 3$ and that three users were received with the same

power values.

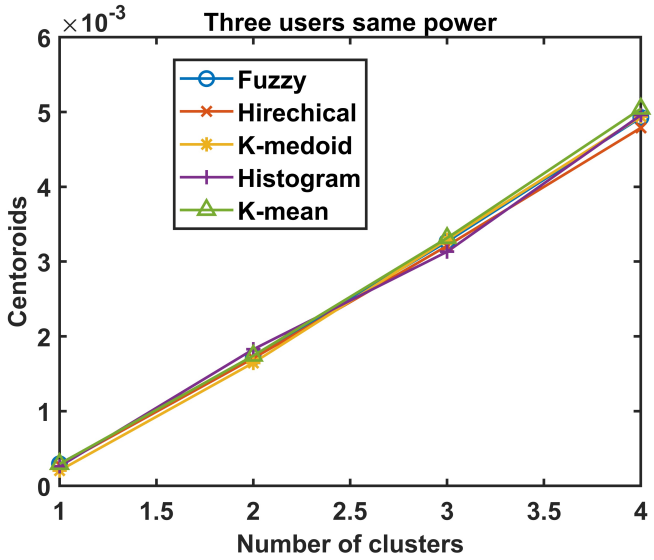

Figure 4.11: Clusters centroids

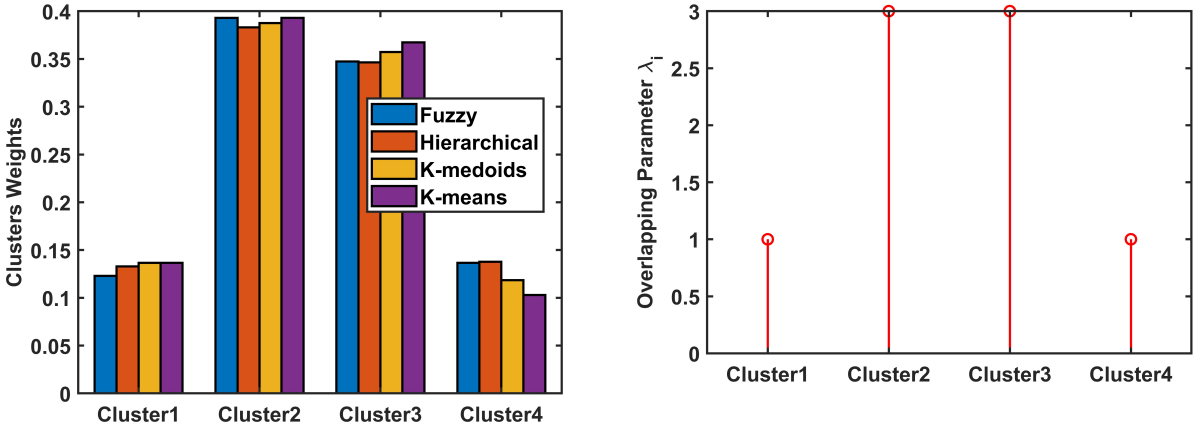

(a) Cluster weight ρ_i (b) Overlapping parameter λ_i

Figure 4.12: Number of users calculation

4. **Turbulence effects**

FSOC can be significantly degraded due to its optical beam atmospheric turbulence sensitivity. Inhomogeneities in atmospheric temperature and pressure lead to random changes in the refractive index, which then cause random variations in the amplitude and phase of optical wave propagating in the turbulent medium. The result is a degraded optical signal [12]. Fluctuation of the received signal intensity (i.e., scintillations

[103]) affects FSOC system performance quality and heavily reduces communication performance. The proposed amplitude-based method was evaluated under atmospheric turbulence scenarios. Description of the atmospheric turbulence generation and analysis are detailed in Chapter 3. Received mixed signal under moderate atmospheric turbulence was analyzed. Moderate atmospheric turbulence is characterized by 58.61 ° temperature; 14.21 m/s wind speed, and 80.56% humidity, which resulted in a scintillation index σ_I^2 equal to $0.1330[m^2]$ and refractive index structure constant parameter C_n^2 equal to $6.19x10^{-12}$ $[m^{-2/3}]$. Fig. 4.13 illustrates peak detection for 4.13a two users and 4.13b three users—two of which have the same power for turbulent (See red line) and non-turbulent (See blue line) scenarios. Note that turbulence effect on the empirical distribution of the received mixed signal causes received signal amplitude attenuation and a broadening of obtained peaks. Broadening is clearly visible by comparing peak spacing distances and reduced peak occurrence value of the turbulence compared to non-turbulence. Broadening is primarily due to increasing intensity fluctuations (i.e., temperature and wind); attenuation is mainly caused by the humidity generator (i.e., fog). Weighted clustering analysis was computed, and overlapping parameter $\lambda_i = 1$ with $1 \leq i \leq 4$ was calculated for Fig. 4.13a and $\lambda_1 = \lambda_2 = \lambda_5 = \lambda_6 = 1$ and $\lambda_3 = \lambda_4 = 2$ were computed for Fig. 4.13b, confirming two and three communicating users, respectively.

The significance of the developed methodology, although simple, is its effectiveness to estimate transmitting users regardless of their transmission times; hence no synchronization or prior knowledge of transmission times are required. The algorithm can be implemented at the PHY-layer to continuously monitor power levels and their associated weights for determining the number of users as transmissions are asynchronously added or dropped. Accuracy analysis was conducted on 45 tested cases to evaluate overall performance of the proposed methodology. Accuracy was defined as the number of cases in which the number of transmitting users was correctly estimated over the total number of studied cases. Results are shown in Table 4.1. The 45 cases were separated in the following way: 20 for two user scenarios

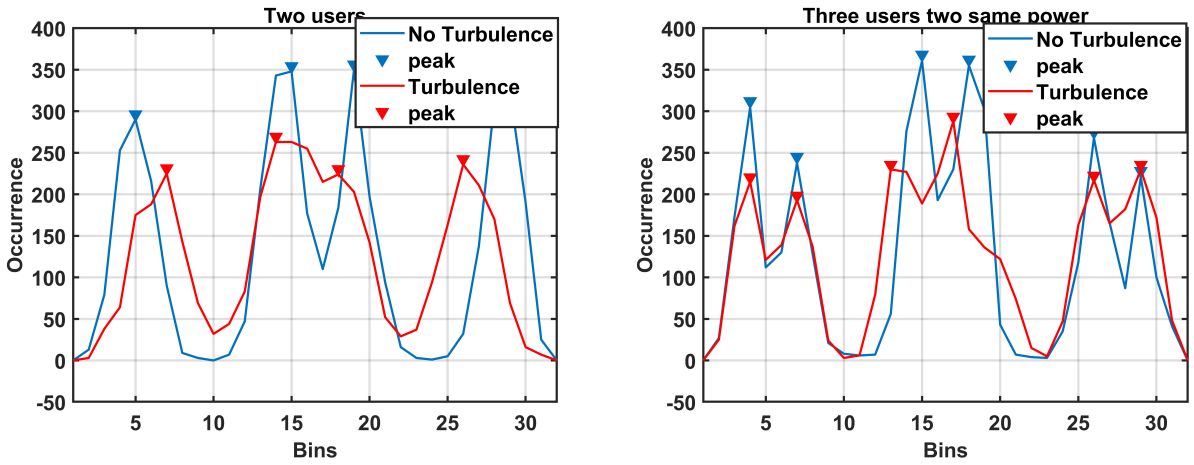

(a) Two users

(b) Three users

Figure 4.13: Turbulence effects

and 25 for three user scenarios. High accuracy greater than 92 % was achieved for all cases.

Table 4.1: Accuracy Analysis

NUMBER OF USERS	2	3
ACCURACY [%]	100	92

4.2 User Discovery Algorithm: Sample Complexity Analysis

A crucial issue in ML algorithms is determining the amount of data needed to achieve a specific required performance (i.e., sample complexity [104]) [63], [63], [63], [63]. In fact, data sets that require lengthy processing time or excessive memory represent a significant limiting factor for real-time applications, even though improved accurate performance is guaranteed. Required storage for many clustering algorithms is more than linear. For example, hierarchical clustering memory requires $O(m^2)$, where m is the number of data objects. Large dataset scalability for clustering algorithms has been investigated. Given cluster weight ρ_i definition in Eq. 4.3, the number of processed samples represents a fundamental parameter for achieving accurate estimation in the proposed methodology. Furthermore, accurate peak detection in the preprocessing analysis (See Eq. 4.2) is a crucial step for clustering initialization. Optimal threshold selection is pivotal. Experimental analysis for identifying required

sample size and receiver sampling rate was conducted to obtain accurate estimation of number of users. The objective was to identify the minimum sample number of the received signals (i.e., preamble signal length) collected and processed with a given receiver sampling rate for accurately detecting histogram peaks of $H_L[y_{LF}]$ in the pre-processing analysis. Two approaches were experimentally tested—(separately and combined): 1) varying sample size N_s ($N_s = L$ of Eq. 4.3) of received signal and 2) varying-sampling reduction factor M for measuring m power levels detected at the receiver side in the pre-processing step. These are illustrated in Fig. 4.3b. To perform peak detection (i.e., local maxima of the $H_L[y_{LF}]$), three thresholds were evaluated. Threshold is defined as the level of occurrences in the 1D histogram $H_L[y_{LF}]$ after a crossed peak is detected. Three evaluated thresholds—50, 100, and adaptive (i.e., median value of $H_L[y_{LF}]$ occurrence) were chosen. Afterwards, a comparison between detected m and expected peaks k was computed, where number of expected peaks was $k = 2^2 = 4$ for two users and $k = 2^3 = 8$ for three users. Analysis was conducted for one, two, and three users. Results for two- and three-user scenarios are discussed and illustrated in the next sections.

4.2.1 Sampling Rate Analysis

The first analysis decreased the sampling rate of the time series-received mixed signal shown in Fig. 4.2a by a factor M. Data were collected, and sampling rate reduction was performed as a pre-processing step. $M = 1, 2, 3$ were tested and results are illustrated in Fig. 4.14. Figs. 4.14a and 4.14b show the local maxima of the empirical $1D$ histogram $H_L[y_{LF}]$ for $M = 1, 2, 3$ for two and three users, respectively. When comparing results shown in Figs. 4.16, one can see that reducing under-sampling factor M causes the histogram shape to change and the location of detected peaks to shift in a uniform way. This phenomenon is true because samples belonging to each peak are sampled with equal probability. Consequently, peak locations are not shifting significantly. To define the number of detected peaks, three different thresholds—50, 100, and adaptive—were evaluated. The adaptive threshold is illustrated in Figs. 4.14a and 4.14b for each histogram computed at each M value (See

dotted horizontal lines in Fig.4.14). Ten acquisitions were collected, and detected peak mean values and standard deviations were computed. Fig. 4.15a and Fig. 4.15b illustrate

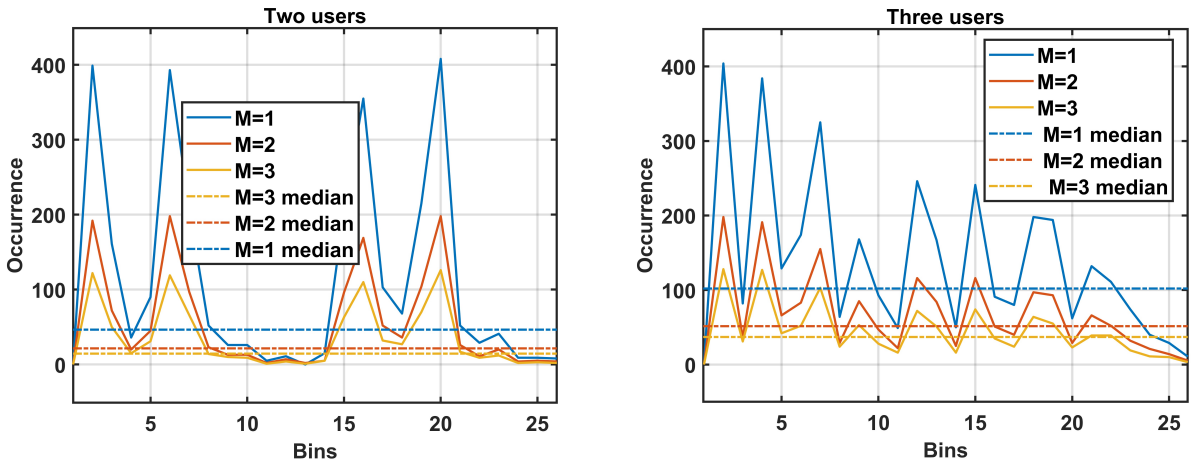

(a) Two users peak detection

(b) Three users peak detection

Figure 4.14: Under-sampling factor M

the number of detected peaks obtained with the three thresholds and number of expected peaks (See magenta dotted line) versus the sampling reduction factor M for two and three users. Given that M increases, the fixed thresholds underestimated the number of peaks, while the adaptive threshold correctly detected the number of peaks for all tested M values. To identify the number of samples that nullify the error between detected m and correct k number of peaks, the absolute error was defined as $Err = |k - m|$ for the adaptive threshold. Computed absolute error is illustrated in Fig. 4.18a, which shows that zero error was subsequently obtained for all M values in both two-(See blue line) and three-(See magenta line) user scenarios.

4.2.2 Number of Samples Analysis

The second analysis varied number of samples N_s of the time series received mixed signal for three users, as shown in Fig. 4.2a. Starting sample size N_s = 3,208 and 4,010 samples were used for two- and three-users, respectively. Sample size was consecutively reduced by steps of 500 samples, and the local maxima of empirical 1-D histogram $H_L[y_{LF}]$ were computed, as shown in Figs. 4.16. Similar to the previous case, the histogram shape

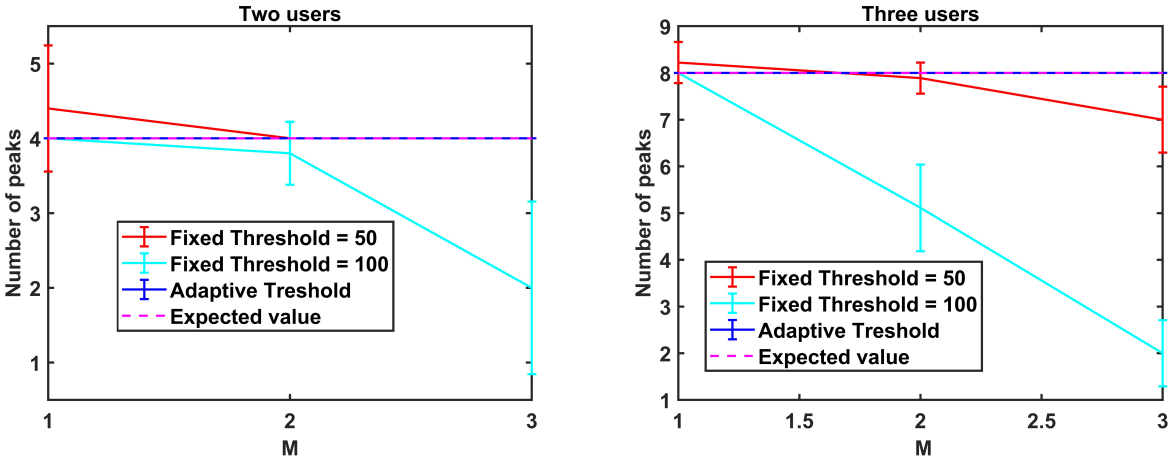

(a) Peaks detection analysis two users (b) Peaks detection analysis three users

Figure 4.15: Under-sampling factor M

and peak locations change; however, this phenomenon occurs in a less uniform way when compared to the previous analysis. Ten acquisitions were collected and processed for each scenario. Mean value and standard deviations of detected peaks were computed. Fig. 4.17a

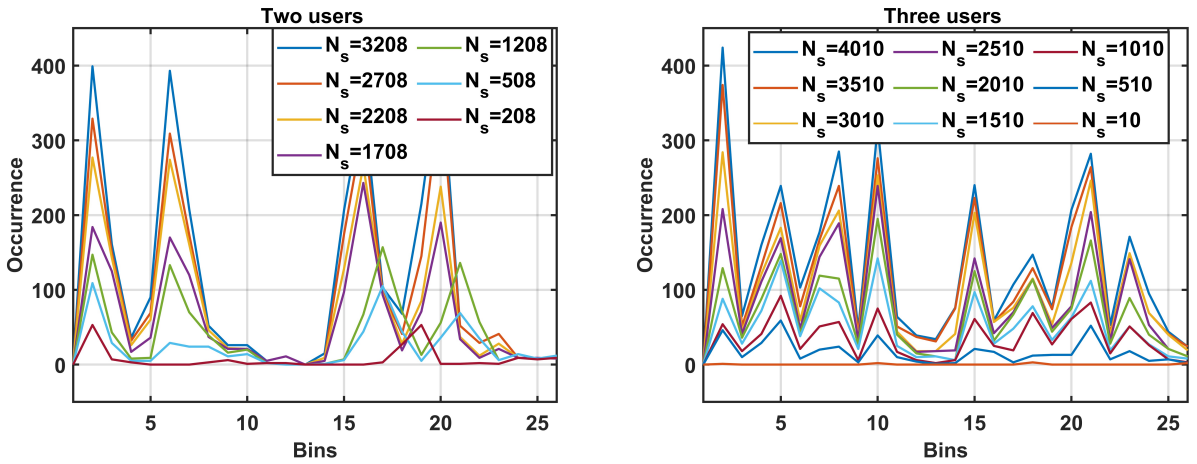

(a) Two users peak detection (b) Three users peak detection

Figure 4.16: Number of samples N_s

illustrates the number of detected peaks and expected peaks obtained with three thresholds versus sample number N_s for two users, and Fig. 4.17b shows with three users. Results demonstrate that the adaptive threshold (See blue line) converges faster to the correct number of peaks (See magenta dotted line) than the fixed thresholds. The fixed threshold of 100 (See light blue line) converges to the correct number of peaks slowly, whereas the fixed

threshold of 50 (See red line) first converges, and then over-estimates number of peaks. The latter is primarily due to the fact that it might detect small peaks caused by noise. Absolute error was computed, and results show that it is equal to zero, given that the number of analyzed samples is equal to or greater than N_s = 1,208 for two users (See blue line) and N_s = 2,510 for three users (See magenta line), as shown in Fig. 4.18b.

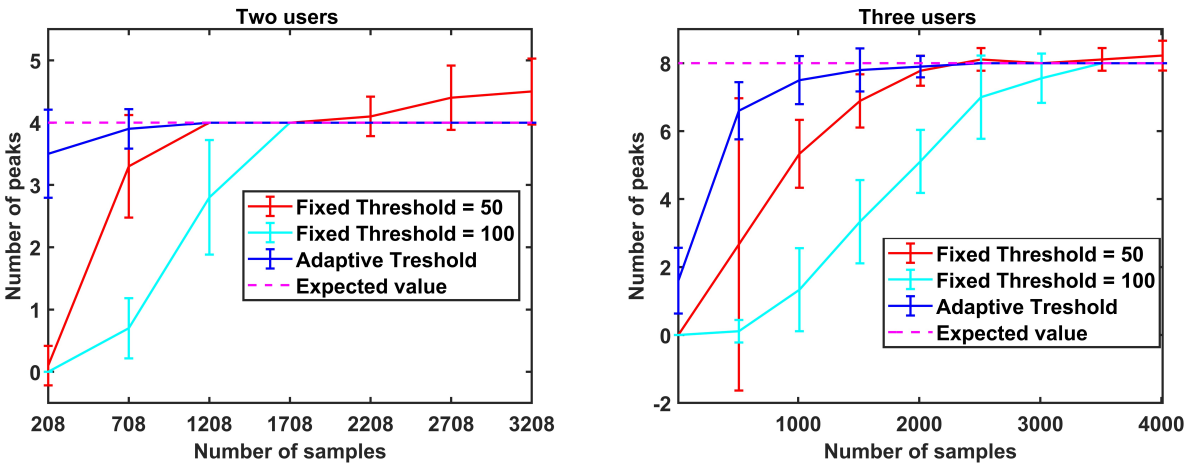

(a) Peaks detection analysis two users (b) Peaks detection analysis three users

Figure 4.17: Number of samples N_s

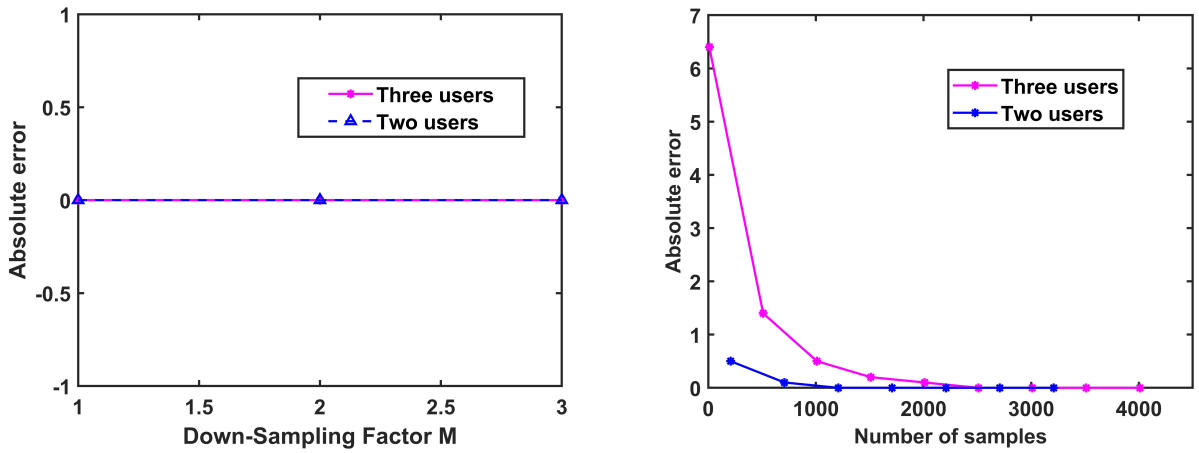

(a) Sampling rate M (b) Number of samples N_s

Figure 4.18: Absolute error

4.2.3 Combined Analysis

Finally, a combined analysis of number of samples N_s with various sampling rate

reduction M was conducted. Figs. 4.19a and 4.19b show the number of detected peaks using all three thresholds versus the number of samples for different factors M for two and three users, respectively. Adaptive thresholds (See blue lines) converge faster than fixed thresholds to the correct number of peaks for all tested M. Fixed threshold 50 (See red line) converges slowly to the correct number of peaks, and then overestimates them, while fixed threshold 100 (See light blue line) converges slower than other thresholds for all tested sampling reduction factors M. The same behavior was observed for a given threshold and with varying M values. Sample numbers above which zero error were obtained was considered the minimum number of samples for each sampling rate to obtain an accurate estimation of number of peaks for a three-user scenario (See Fig. 4.20). As such, those values were employed for the final analysis.

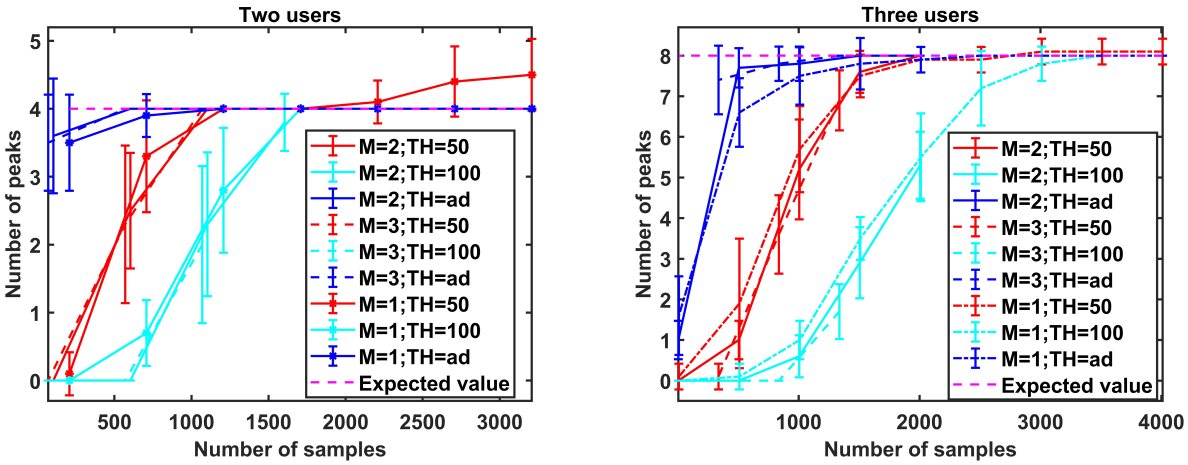

(a) Two users

(b) Three users

Figure 4.19: Combined analysis

4.2.4 Results

This analysis aimed to derive an empirical equation for predicting the number of required samples, given the receiver sampling rate, for correctly estimating the number of concurrently transmitting users. Nonlinear regression analysis was adopted as the methodology for deriving the function: $N_{users} = f(N_s, M)$ that best fit data points .Fig. 4.21 demonstrates the number of detectable users versus the number of samples required

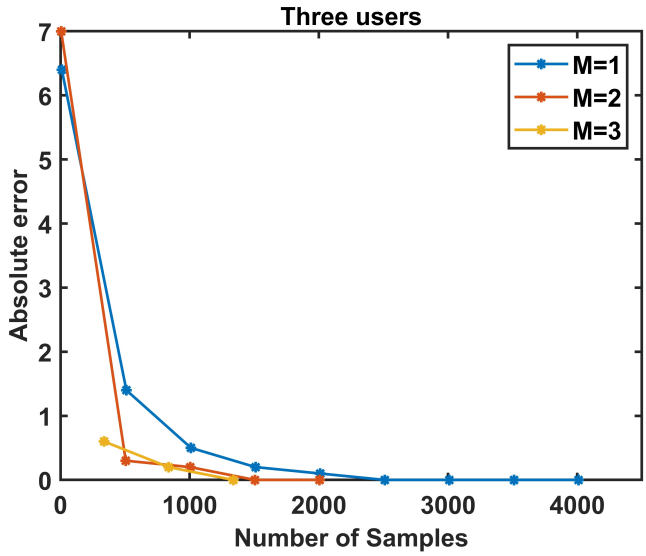

Figure 4.20: Absolute error for three users

for correct detection when $M = 1, 2, 3$ (See red, blue, and black lines, respectively). Both experimental data and obtained fitting curves are illustrated therein. Best fit was obtained for each curve using the following power law: $y = ax^b + c$, where y is the number of users; x is the number of samples; and a, b, c are coefficients. Hence, each curve can be mathematically expressed, as follows.

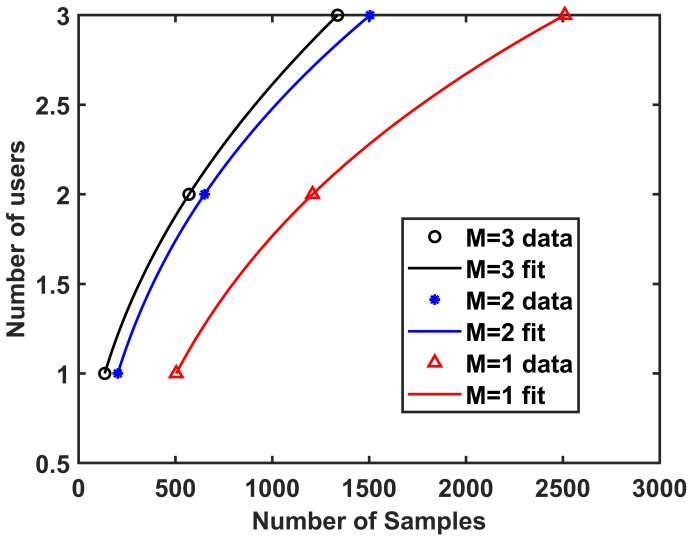

Figure 4.21: Fitting

$$N_{users}(N_s, M = i) = a_i * {N_s}^{b_i} + c_i \tag{4.8}$$

where $i = 1, 2, 3$. Table 4.2 shows calculated R-square values for evaluating fitting performance. R-square indicates the correlation between response values and predicted response values and also measures the extent of how successful the fit is in explaining data variation. $R^2 = 1$ was obtained for all cases, meaning that accurate fitting was performed.

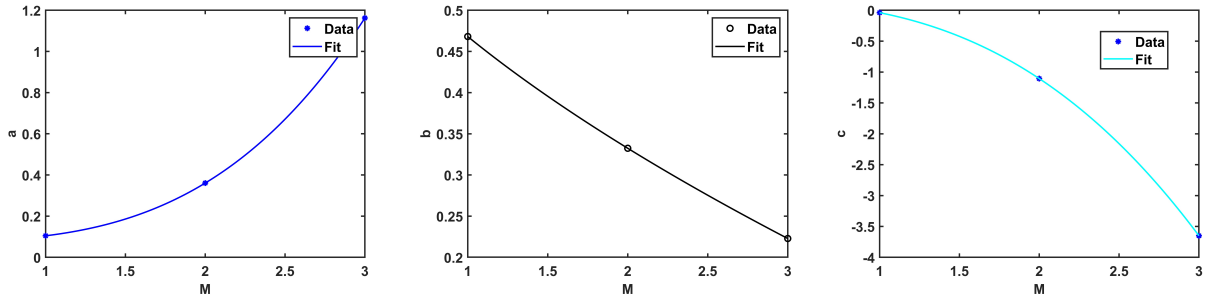

(a) a (b) b (c) c

Figure 4.22: Fitting parameters

Table 4.2: Fitting Performance

M	1	2	3
R-Square	1	1	1

Each fitting curve resulted in different parameters a_i, b_i, c_i for $i = 1, 2, 3$, indicating each is a function of the sampling reduction factor M and, consequently, of receiver sampling rate (See Eq. 4.8). Therefore, curve fitting was applied on a_i, b_i, c_i to derive the functions $a = f(M)$, $b = f(M)$, and $c = f(M)$. Vectors are defined as $a = [a_1 a_2 a_3]$, $b = [b_1 b_2 b_3]$, and $c = [c_1 c_2 c_3]$. Fitting was performed on these coefficients vectors, as shown in Fig. 15. Power law equation was employed for fitting so that each coefficient could be expressed, as follows.

$$a(M) = a' * M^{b'} + c' \tag{4.9a}$$

$$b(M) = a'' * M^{b''} + c'' \tag{4.9b}$$

$$c(M) = a''' * M^{b'''} + c''' \tag{4.9c}$$

$R^2 = 1$ was obtained for all cases, meaning that accurate fitting was performed for all

coefficients. Fig. 4.22 also shows data points and obtained fitting curves for a, b, and c vectors. To obtain a final model for prediction, Eqs. 4.8 and 4.9 were combined into the single Eq. 4.10, which—when provided with receiver sampling rate and number of received and processed samples—indicates how to predict the number of successfully detectable users utilizing the proposed methodology:

$$N_{users}(N_s, M) = a * {N_s}^b + c = (a' * M^{b'} + c') * {N_s}^{a'' * M^{b''} + c''} + a''' * M^{b'''} + c''' \tag{4.10}$$

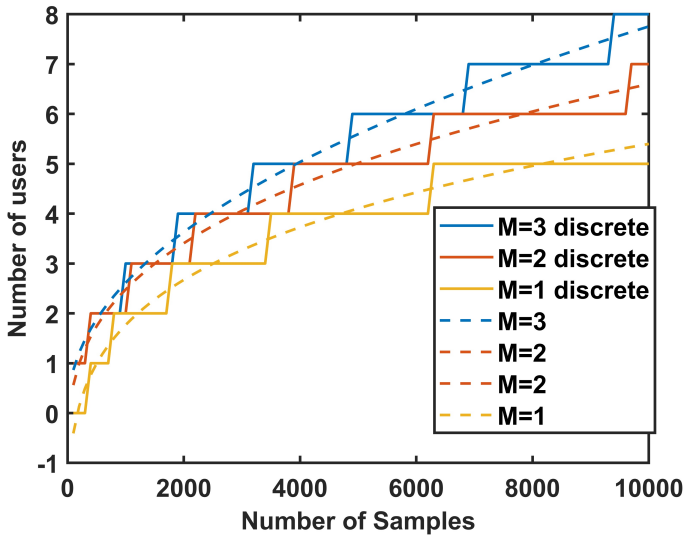

Figure 4.23: Final fitting equation

Fig. 4.23 shows the trend of the predicted N_{users} for $M = 1, 2, 3$ and for a range of sample numbers $[10 : 10,000]$, as described in Eq. 4.10 Since number of users is a discrete parameter, quantization was performed on the predicted N_{user}values. Obtained results will aid in designing preamble signal length at the head of the packets. For example, if the FSO receiving system is designed to support four simultaneous users with a receiver sampling rate of 1 Gsample/s and required sample size of $5,000$ samples, then packet length will be designed with a preamble length of 5 μs. Moreover, obtained results will be exploited to assist with the design of the electrical and optical receiver system in terms of memory requirement and implementation of a cognitive receiver with adaptive sampling rate. The aim is conserving computational complexity and reducing power consumption, which further

reduces SWaP system specifications.

4.2.5 Model Validation

To validate the derived empirical model, four independent users concurrently transmitting were combined into a single receiver (i.e., photodetector) with $M = 1, 2, 3$. User wavelengths and data-rate were set selected to demonstrate wavelength independence of the proposed method and applicability to higher data-rate. 1550 nm and 100 Mbps were set for user 1; 1550 nm and 150 Mbps for user 2; 1310 nm and 200 Mbps for user 3; and 1310 nm and 250 Mbps for user 4. All pre-processing steps were applied on the time-series received mixed signals and the minimum number of samples N_s, which guaranteed accurate peak detection in the obtained empirical 1-D histogram $H_L[y_L F]$ for each M were identified. The empirical cumulative distribution function (CDF) was calculated to demonstrate validation results. CDF is the probability that the number of samples required to correctly estimate number of communicating users produces a value less than or equal to a given N_s. Ten acquisitions were considered in the CDF calculation for each M value; results are illustrated in Fig. 4.24. The blue, orange, and yellow lines represent the empirical CDFs obtained for $M = 1, 2, 3$, respectively. Each point in the CDF represents minimum number of samples N_s required to correctly identify $m = k = 2^4 = 16$ peaks in the $H_L[y_L F]$. The blue, orange, and yellow dashed vertical lines represent the upper bound N_s^* for estimating four users, as predicted by Eq. 4.10, whose trend is illustrated in Fig. 4.23. The upper bound $N_s{}^*$ is defined as $N_s^* = \{N_s < N_s^* : m = k\}$, where m is the number of detected peaks and k number of expected peaks. Given that all obtained CDF curves are on the left side of the corresponding dashed lines (e.g., $N_s < N_s{}^*$), all tested cases could correctly detect four users requiring the number of samples N_s of the time-series received mixed signals within the predicted region (i.e., $N_s < N_s{}^* = 6,200, 3,800, 3,100$ for four users scenario and for $M = 1, 2, 3$, respectively). Experimental results confirm the goodness-of-fit for the derived empirical equation.

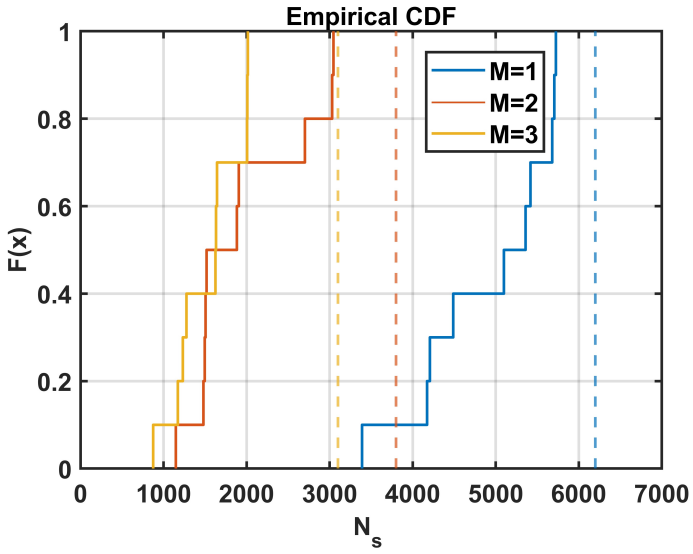

Figure 4.24: Validation results

4.2.6 System Limitations

The presented methodology is a power-based technique that uses the amplitude of the received mixed signal to calculate number of simultaneously communicating users. Notably, two factors could affect the proposed method's accuracy and limit system performance.

- Dynamic range of the received mixed signal

  Fig. 4.25 shows the histogram $H_L[y_L F]$ of received mixed signals for two transmitting users with diverse SNRs: SNR1=26 dB and SNR2= 20 dB (See blue histogram) and SNR1=16 dB and SNR2= 10 dB (See green histogram). Dynamic range of the blue histogram (i.e., 7 mV) is wider than the green histogram (i.e., 2 mV). The blue histogram $H_L[y_L F]$ can easily accommodate additional users within the dynamic range (i.e., additional peaks within the histogram). Resulting peaks will be clearly separated and easily detected (i.e., there is enough space between two peaks 2 mV). The green histogram $H_L[y_L F]$ can accommodate fewer users within its dynamic range because additional users will result in an increasing number of merging peaks. The resulting peaks will be difficult to distinguish from one another (i.e., space between two peaks is 0.5 mV). The higher the dynamic range, the higher the number of users that can

be accommodated and detected by the proposed methodology.

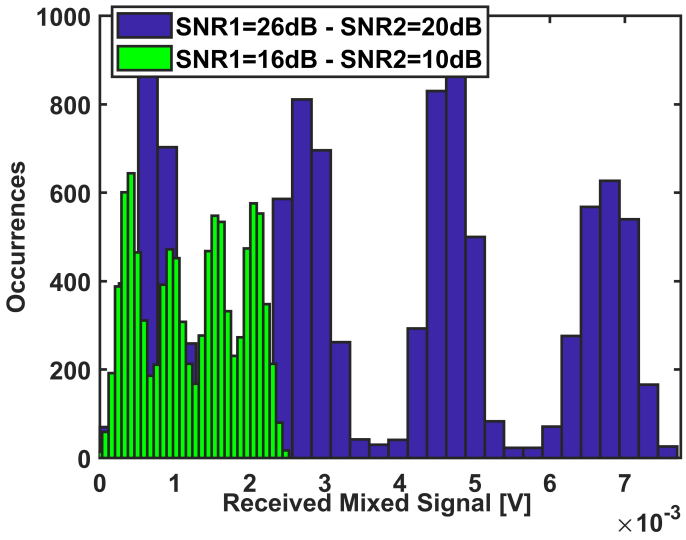

Figure 4.25: Received mixed signals with different dynamic ranges

- Multi-level modulation format

  The developed technique has been validated on experimental data using a binary modulation format (i.e., OOK). Given the needs of upcoming optical networks for increased bandwidth and data-rate, multi-level and coherent modulation formats (i.e., QAM) with high-bandwidth efficiency have been under consideration [12]. Extension of the proposed methodology to accommodate multiple modulation formats could consist of applying the technique separately on the real and imaginary part of the received mixed signal. However, the diverse number of users and m-QAM modulation format can result in constellation diagrams with equal symbol distributions. The result is an identical, empirical 1-D histogram $H_L[y_{LF}]$ created from the real and imaginary parts of the received complex signal amplitude. For example, Fig. 4.26 illustrates the constellation diagram obtained with computer simulations for Fig. 4.26a two users employing 4-QAM and Fig. 4.26b one user with 16-QAM modulation. Given that the modulation format is known at the receiver side, the number of users could be retrieved as $N = log_m p_c$, where m is the modulation order and p_c is the number of peaks in the constellation diagram. In other words, $p_c = k_R * k_I$, where k_R is the number of de-

tected peaks in $H_L[Re\{y_{LF}\}]$ of the real part of the complex received signal and k_I is the number of detected peaks in $H_L[Im\{y_{LF}\}]$ of the imaginary part. It is important to note that if the modulation format is not known, the proposed methodology fails to correctly estimate the number of users.

(a) Two users 4-QAM (b) One user 16-QAM

Figure 4.26: QAM

4.3 QoT Estimation

Users sharing resources (time, frequency, wavelength, space), will overlap at the receiving node and interfere with each other. As such, measuring QoT parameters (e.g., SNR) for each user prior to signal separation becomes a challenging task, given no interference cancellation. Prior knowledge of QoT would aid the cognitive optical receiver in deciding if users' signal should not be decoded, given its QoT is below a certain threshold. Advance knowledge of signal quality will result in saving computational time and complexity. A methodology for estimating QoT for a multi-user FSOC link was presented and experimentally validated. The suggested technique leverages supervised ML for joint estimation of two transmitting users' SNR received into a single node FSOC receiver that share time, bandwidth, and space resources.

4.3.1 Experimental Setup

The FSO experimental setup used for this research was composed of two independent users based on an OOK modulation (See Fig. 4.27). User 1 consisted of the Thorlabs MX10B digital reference transmitter,driven by a PRBS featuring $2^{31}-1$ bits length and 300 Mbps data-rate. User 2 consisted of a 1310 nm optical module transceiver (SFP) driven via an SMA-to-SFP board by a PRBS with the same features. Variable optical attenuators were used to vary channel-input power for user 1 and user 2, and channel noise was measured to include SNR calculation. Transmitted signals were mixed through a wavelength division multiplexer designed for combining two signals at 1310 nm and 1550 nm. Mixed signal was transmitted using a free-space collimators pair with 37.17 mm focal length. The mixed signal propagated through free space for 1 m, and then was collected by a 5 GHz DET08CFC photodetector. Although two wavelengths were employed at the transmitting side, no wavelength selective filter was implemented at the receiving side. An oscilloscope with spectrum analyzer capability and 20 Gsample/s sampling rate was used for recording data collected from the photodetector and computing SNR values required for training. SNR targets were measured using each user separately. Data were postprocessed offline with MATLAB software on a 2.60-GHz Intel Core i7 processor.

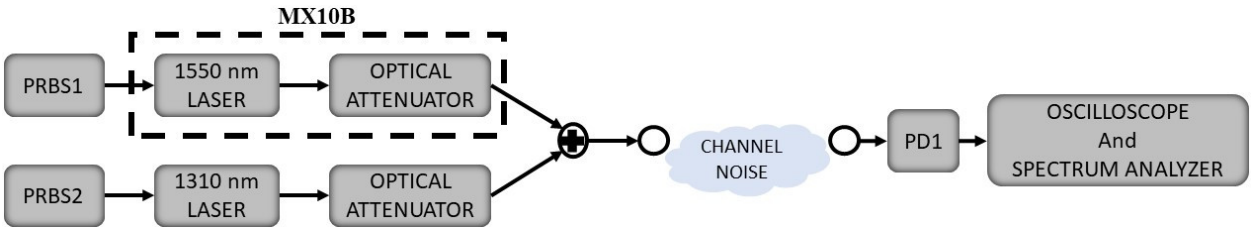

Figure 4.27: Experimental setup depiction

4.3.2 Methodology

1. **Data collection**

   Experimentation was conducted while observing the following processes:

   (a) Sample background channel noise power N[dBm] in the lab setup.

(b) Vary transmission power using optical attenuator.

(c) Measure received power RX[dBm] per user transmission.

(d) Calculate SNR per user by SNR[dB]=RX[dBm]-N[dBm].

(e) Collect and process power measurements for SNR calculations when user 1 and user 2 are transmitting and received simultaneously.

Received SNR1 for user 1 was varied from 26 dB to 10 dB in 2 dB steps. SNR2 for user 2 was similarly varied from 20 dB to 10 dB. For each of the 54 SNR1/SNR2 combinations, between 450 and 500 acquisitions of the time series received mixed signal were collected. The resulting dataset consisted of 25,967 instances. Fig. 4.28 illustrates the received mixed signal for SNR1=16 dB and SNR2 =10 dB.

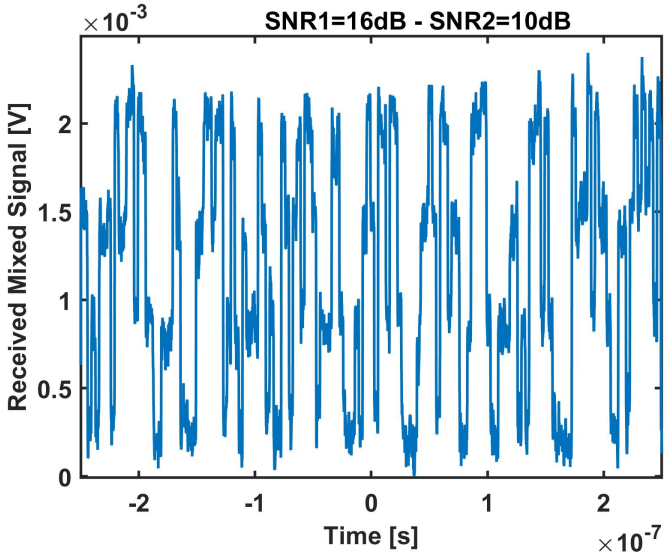

Figure 4.28: Received mixed signals

2. **Feature selection**

Two approaches were investigated to select input features for building classification models: histogram counts and local maxima.

(a) Histogram Counts

The first approach used the empirical histogram of received mixed signal amplitude as input features. Histogram distribution is sensitive to changes in received

SNRs. Figs. 4.29a and 4.29b show the empirical histogram of the received mixed signal for SNR1=16 dB /SNR2=10 dB and SNR1=16 dB /SNR2=18 dB, respectively. Note that varying SNRs causes changes in histogram distribution. When SNR2 increased from 10 dB to 18 dB, SNR difference between user 1 and user 2 signals changes from 6 dB to 2 dB. Consequently, separation spacing between the middle two peaks reduced from 6 dB to 2 dB. The vector of obtained occurrences was used as classifier input. Since each histogram contained 30 bins, the occurrences of input vector consisted of 30 features.

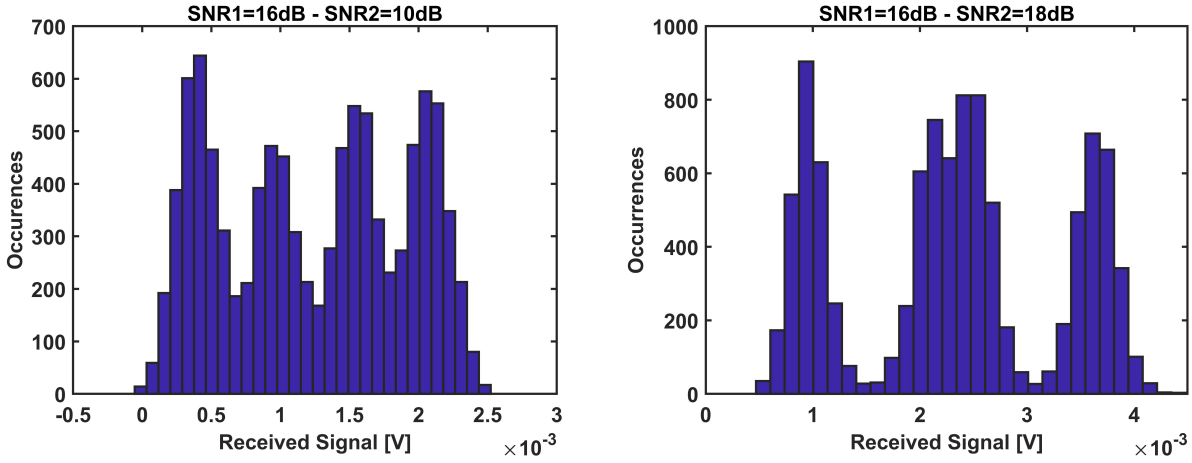

(a) SNR1=16, SNR2=10 dB (b) SNR1=16, SNR2=18 dB

Figure 4.29: Histogram of received mixed signal

(b) Local Maxima

The second approach detected local maxima (i.e., peaks) of the empirical histogram, shown in 4.29, of the received signal amplitude, as shown in Figs. 4.30a and 4.30b. For two transmitting users and OOK modulation, the expected number of peaks was four—given two users were received with different power—or three—given two users were received with the same power. Peak locations (i.e., the amplitude valued with the highest occurrences) were used as input features, guaranteeing dimensionality reduction: four features were employed from 30 features, to train the classifiers.

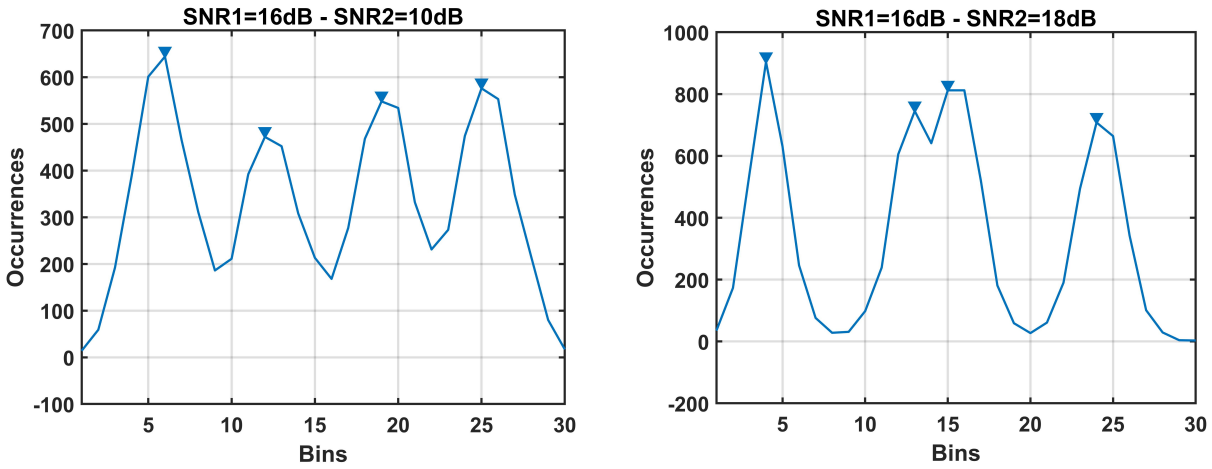

(a) SNR1=16, SNR2=10 dB (b) SNR1=16, SNR2=18 dB

Figure 4.30: Peak detection of histograms

3. **Learning models**

Several learning models (e.g., Decision Tree (DT) [100 number of splits, Gini index as split criterion], K-Nearest Neighbor (K-NN) [k=10 and Euclidean distance], Random Forest (RF) [30 learners, 53 number of split and 0.1 learning rate], Naïve Bayes (NB) [gaussian kernel], Support Vector Machine (SVM) [quadratic kernel], and ANN [one hidden layer, 50 neurons and conjugate gradient backpropagation algorithm]) were leveraged as ML classifiers in this study. A holdout validation method was used, wherein 80% of data were used for training and 20% for testing. Output of the classifiers was the SNR1-SNR2 combination (i.e., 1610 indicates SNR1=16 dB and SNR2=10 dB).

4.3.3 Results

1. **Histogram: SNR1-SNR2**

Results for simultaneous SNR1-SNR2 classification using empirical histogram occurrences are illustrated in Fig. 4.31. Classification accuracy [%] for each tested model is shown on the left label of the graph and the training time on right [s] label. SVM achieved the best performance with 76.2% classification accuracy and 241.85 s training time. DT demonstrated the worst accuracy performance and lowest training time.

Notably, classification performance improved at the expense of increased computation time.

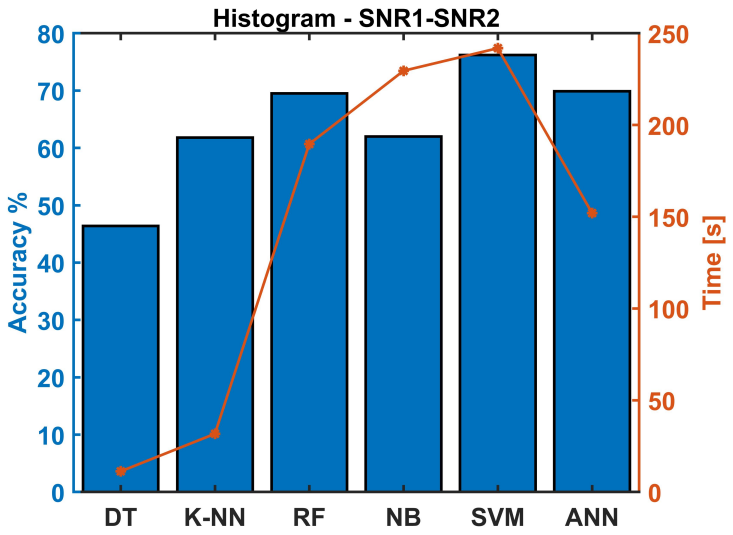

Figure 4.31: Classification accuracy and training time

2. **Histogram local maxima: SNR1-SNR2**

Results for simultaneous SNR1-SNR2 classification using peak locations are illustrated in Fig. 4.32. Increased accuracy was obtained for trained classifiers resulting in increased training time for the majority of tested models. SVM testing accuracy was 92%; ;while RF and K-NN demonstrated high performance with an accuracy greater than 90%. Overall, reducing the number of features resulted in improved classification performance.

Previous results did not consider model behavior for each SNR combination. Therefore, SVM was selected as the trained model, and the error for each SNR combination was computed as the number of wrongly predicted classes for each SNR combination over the total number of instances (see Fig. 4.33). One can see that the error tended to decrease when the absolute SNR difference between user 1 and user 2 signals decreased. Minimum error was achieved when SNR2 equaled SNR1, given that the histogram consisted of three peaks that uniquely identified and accurately estimated SNR.

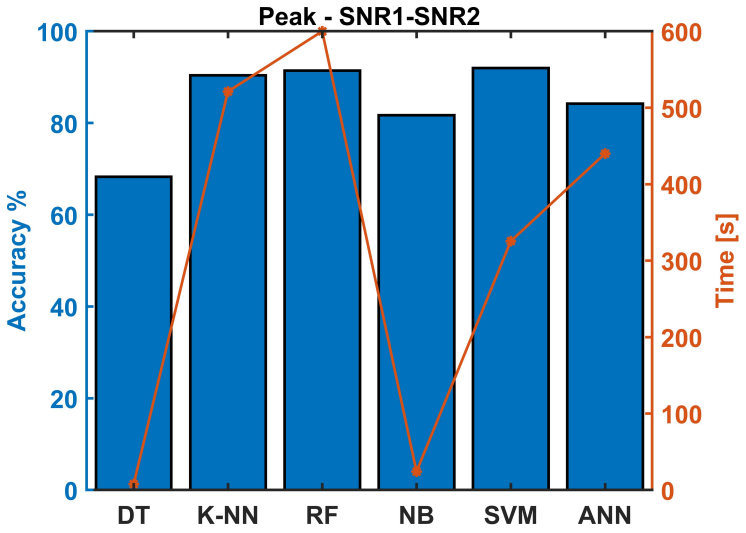

Figure 4.32: Classification accuracy and training time

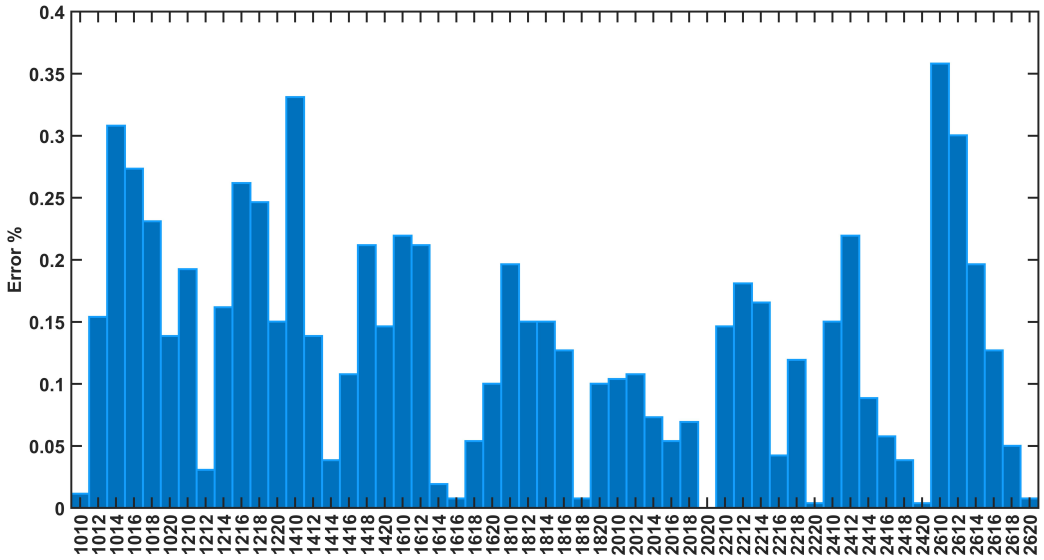

Figure 4.33: Error for each SNR1-SNR1

3. **SNR1 and SNR2**

Previous analysis considered joint estimation of SNR from user 1 and user 2. Derived performance did not consider model capabilities for singularly classifying each SNR. Thus, classifiers were first trained using SNR1 as the target, and later considered SNR2 . The analysis aimed at identifying which user more greatly affected classification error. Fig. 4.34 illustrates achieved accuracy for separately classifying SNR1 (blue

bars) and SNR2 (orange bars). Results show that high classification accuracy was

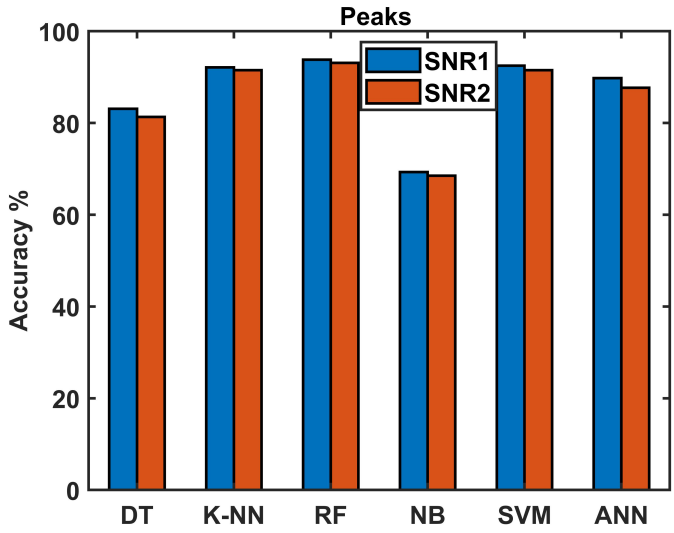

Figure 4.34: Accuracy for SNR1 and SNR2

achieved for both scenarios, and that there was no considerable difference in accuracy between SNR1 and SNR2. The average relative error between user 1 and user 2 SNR accuracy was 1.17%. As such, it is easy to see that they contribute equally to the error calculation illustrated in Fig. 4.33. To better compare classifier performance for SNR1, SNR2, and joint SNR1-SNR2 estimation, Table 4.3 shows obtained accuracies for each trained model. Classifiers demonstrated similar behavior for each case scenario, with the exception of DT, whose accuracy for joint classification worsened, and NB, which improved.

Table 4.3: Accuracy Comparison

Accuracy [%]	DT	KNN	RF	NB	SVM	ANN
SNR1-SNR2	68.3	90.4	91.4	81.7	92	84.2
SNR1	83.1	92.1	93.8	69.3	92.5	89.8
SNR2	81.3	91.5	93.1	68.5	91.5	87.7

4. **Sample Size Analysis for Training**

Dataset scalability represents a practical challenge for ML algorithms to save computational time and memory complexity [101]. Accordingly, sample size analysis was

conducted. Data set consisted of 25,967 data objects. Data size was then consecutively reduced in steps of 5,000 samples. Three outperforming classifiers (i.e., SVM, K-NN, and RF) were selected for the balance of the study. Figs. 4.35a and 4.35b illustrate classifier accuracy [%] and training time [s] versus sample size, respectively, for each classifier.

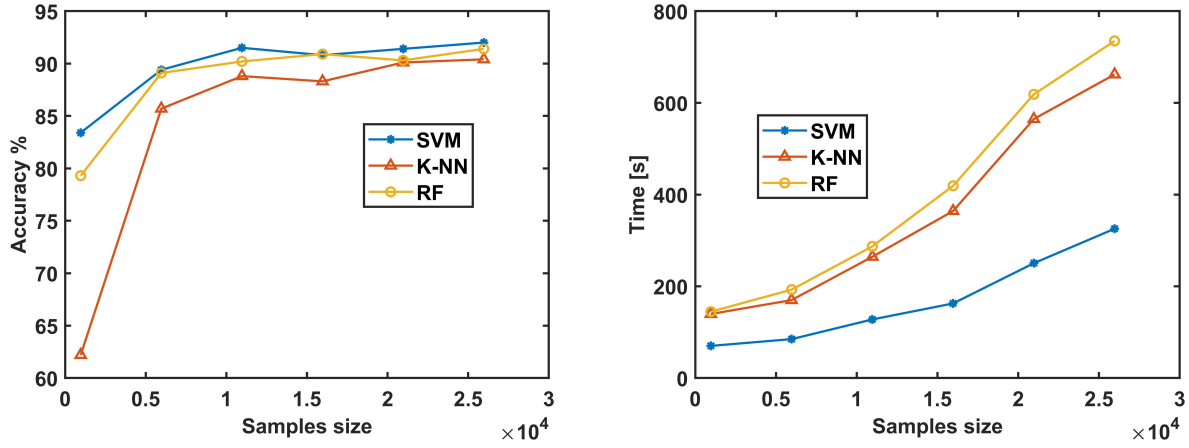

(a) Accuracy (b) Training time

Figure 4.35: Sample size analysis

Overall, SVM outperformed the other two models. For all tested sample sizes, achieved accuracy was slightly higher, and required training time was reduced by half. As expected, training time increased as sample size increased, while achieved accuracy did not increase significantly once sample size was greater than 10,967 instances. Results indicated that 10967 data objects guaranteed an accuracy greater than 90% and a training time less than 130 s.

5. **Sample Size Analysis for Feature Extraction**

The received mixed signal shown in Fig. 4.28 represents a time series signal consisting of 10,000 samples. Each acquisition was processed to obtain a histogram of received amplitude and peak locations. Reducing the number of time series signal samples (i.e., sampling time) changed the histogram shape, and the location of detected peaks began to shift until no peaks were detected. Figs. 4.36a and 4.36b show the empirical

histogram and peak detection, respectively, for varying time series signal sample size. Note that the histograms shape along with the peaks locations vary with the number of

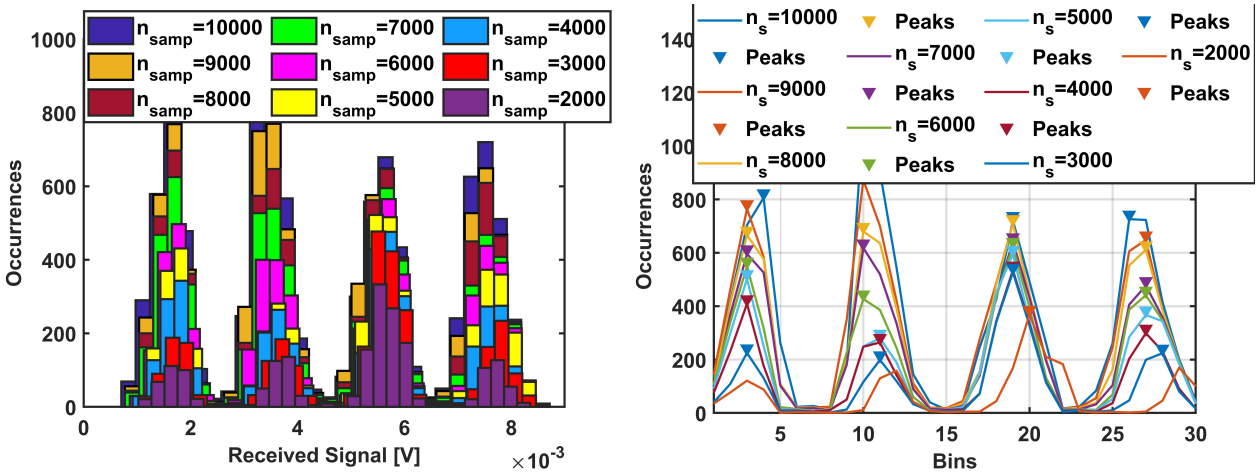

(a) Histogram (b) Peaks detection

Figure 4.36: Sample size analysis for feature extraction

collected time series samples. Number of received signal samples was reduced in steps of 1,000 samples to determine if change affects the SNR embedded information in the empirical histogram. Given that the histogram changes proportionally and constantly with the number of samples, sensitivity to SNRs could be preserved. Because no regular pattern was found, number of time series samples was analyzed. Data object size was fixed to 25,967. SVM, K-NN, and RF classifiers were trained. Fig. 4.37 illustrates testing accuracy versus sample size for feature extraction (i.e., peak location). SVM and RF performed nearly identical, and both achieved an accuracy greater than 90% when time series sample size was greater than or equal to 7,000 samples. Given 4,000 samples, SVM achieved 86% testing accuracy, and RF 87%. Thus, the optical receiver should guarantee an acquisition time $T_S > 7,000$ sampling rate to accurately classify user' SNRs.

4.4 Number of Users and Modulation Format Classification

To address limitations discussed in Section 4.2.6, a CNN-based methodology is presented to automatically classify number of communicating users and their modulation

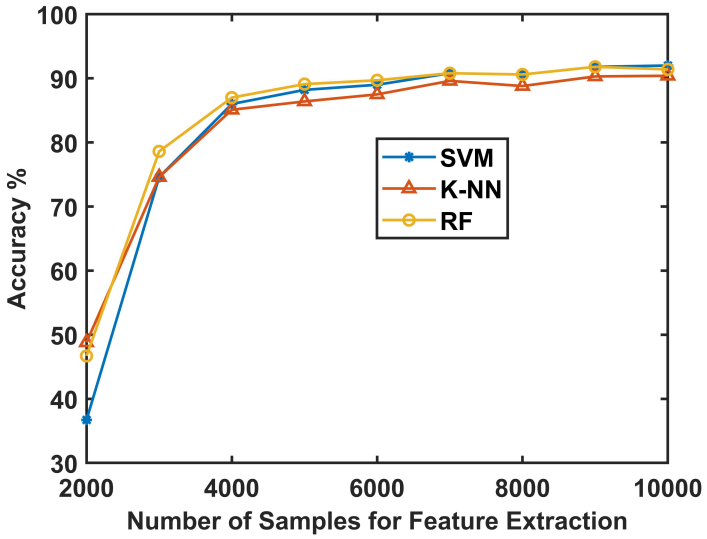

Figure 4.37: Accuracy versus sample size for features extraction

format.

4.4.1 Methodology

1. **Simulations**

   Synthetic data were generated to emulate a multi-user FSOC scenario under additive white gaussian noise (AWGN). The scenario assumes a transmitting side with three independent, optical transmitters sharing time and bandwidth resource and a receiving side with a single photodiode. For each considered user number scenario (e.g., 1, 2, and 3), modulation formats were selected from QPSK-, 8-, 16-, and 32-QAM, resulting in a classification problem with 12 classes. Random selection of SNR values ranging from 0 to 20 dB in 5 dB steps was performed for each user. Extensive simulations were conducted, and for each case the constellation diagram was generated from the received complex-signal symbols. Six thousand constellation diagrams were collected, and each consisted of 84,000 received complex symbols. More specifically, for each user number and modulation format combination, 500 constellation diagrams were generated. Simulations were performed using MATLAB software and the Communication and Deep Learning Toolbox.

Table 4.4: Resolution and image size

R	0.004	0.005	0.006	0.007	0.008	0.009	0.01
M	283	226	189	162	142	126	113

2. **Constellation image generation**

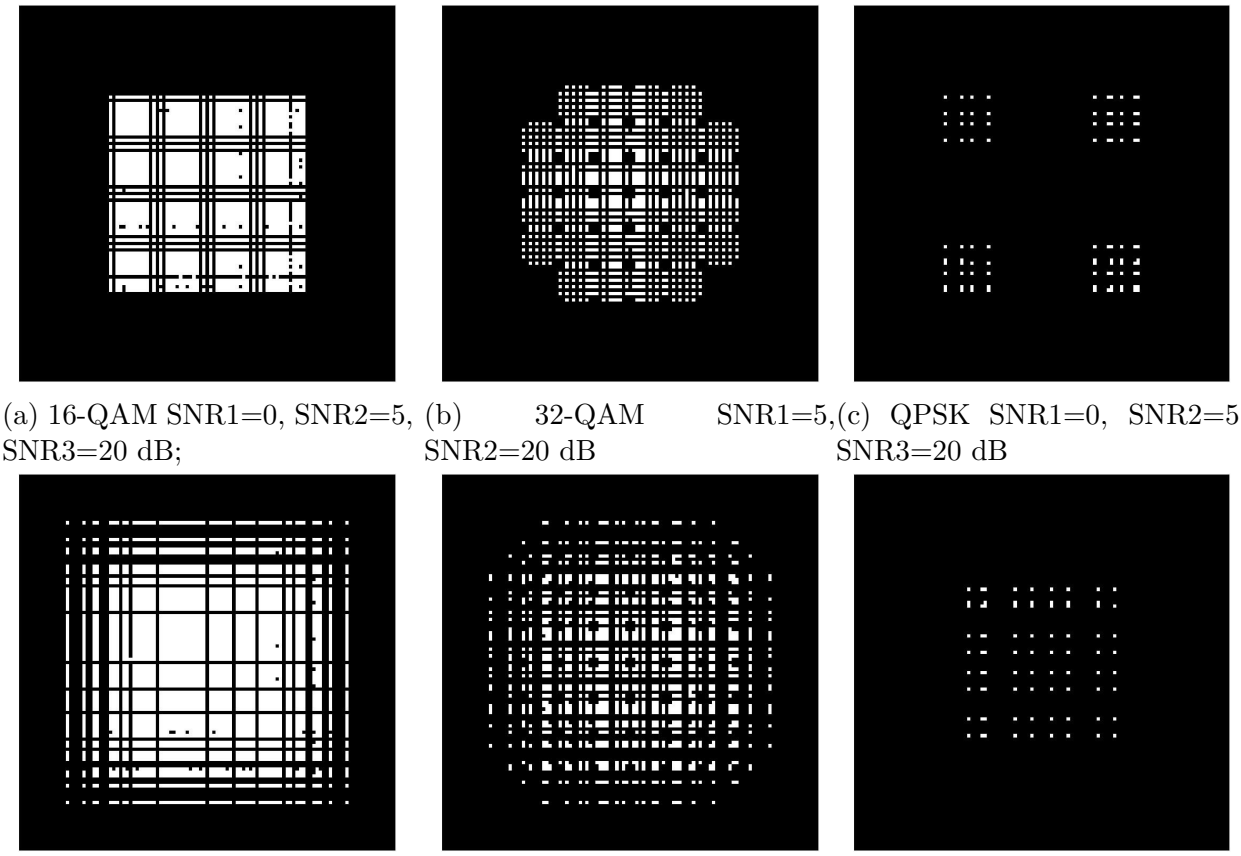

(a) 16-QAM SNR1=0, SNR2=5, SNR3=20 dB; (b) 32-QAM SNR1=5, SNR2=20 dB (c) QPSK SNR1=0, SNR2=5, SNR3=20 dB

(d) 16-QAM SNR1=10, SNR2=15, SNR3=20 dB (e) 32-QAM SNR1=15, SNR2=20 dB (f) QPSK SNR1=0, SNR2=10, SNR3=15 dB

Figure 4.38: Constellations R=0.01

Constellation diagrams were transformed into .png images for input into the CNN model. Black and white images were generated to reduce computation complexity. Each in-phase and quadrature symbol in the constellation diagram was normalized by maximum received power among all received complex signals to obtain same-sized images. Once lower L and upper U limits were defined as received signal minimum and maximum power value, images with varying image resolution R were generated. R ranged from 0.004 to 0.01 with 0.001 incremental steps. Each resolution defined

the image pixel number M (i.e., image size), as illustrated in Table 4.4. Finer image resolution leads to a greater number of pixels and increased image dimension. Once an MxM grid was obtained using $M = (U - L)/R$, each symbol was assigned to a grid pixel according to power value. Fig. 4.38 shows examples of obtained images under various modulation formats, number of broadcasting users, and received SNRs, given that R=0.01. Note that varying user SNRs causes the constellation to change shape. The higher the difference in SNR among users, the sparser the constellation and more separated the received symbols (See Fig. 4.38c). Reducing SNR separation results in decreasing symbol distances. Cleary, each constellation diagram has diverse and distinguishable shapes that could be easily classified by a CNN.

3. **CNN structure**

A CNN architecture was developed to train and classify generated constellation images [105]. CNN output is defined as user number and their modulation formats (e.g., 232 indicates 2 users with 32-QAM). Input images were separated into 80% for training and 20% for testing. An initial learning rate of 0.01 was selected, and maximum number of epochs was initially set to 10. The CNN structure consists of three transformation layers followed by one dense fully connected layer.

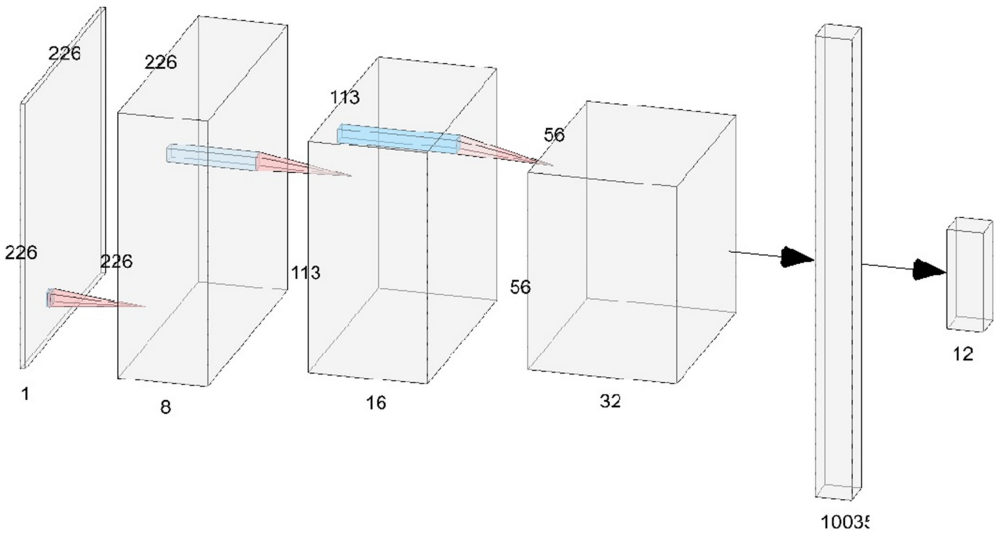

Figure 4.39: CNN structure

Table 4.5: CNN parameters

Layer name	Activation	Filters/Pooling size	Filter stride
Image input	226x226x1	-	-
Convolution	226x226x8	3x3x1	1
Batch normalization	226x226x8	-	-
ReLU	226x226x8	-	-
Max pooling	113x113x8	2x2	2
Convolution	113x113x16	3x3x8	1
Batch normalization	113x113x16	-	-
ReLU	113x113x16	-	-
Max pooling	56x56x16	2x2	2
Convolution	56x56x32	3x3x16	1
Batch normalization	56x56x32	-	-
ReLU	56x56x32	-	-
Fully connected	1x1x12	-	-
Softmax	1x1x12	-	-
Classification output	-	-	-

Fig. 4.39 depicts the complete network structure. Table 4.5 describes in detail each CNN network architecture layer. The 2-D convolutional layer applies sliding convolutional filters with a given filter size and step (i.e., stride) to the input images. The batch normalization layer normalizes each CNN input channel to speed-up training. Rectified Linear Unit (ReLU) layer serves as a nonlinear activation function that performs a threshold operation for each element of the input, where any value less than zero is set to zero. The max pooling layer performs down-sampling by dividing the input into rectangular pooling regions, and then computing the maximum of each region. The fully connected layer combines all features learned from previous layers across the image and classifies the images.

4.4.2 Results

1. **Resolution**

   Identical image sets were generated for each R value using a 2.60-GHz Intel Core i7 processor. Figs. 4.40a and 4.40b show Figs. 4.38d and 4.38e images with resolution 0.004. Note that finer resolution results in an image where separation between received

symbols is more visible when compared with lower resolution, where received symbols combine and results in loss of information. The CNN was trained and validated for each image set with varying resolution. Fig. 4.41 shows the validation (red line) and training (light blue line) accuracy versus the number of iterations for R=0.004. 100% training and validation accuracy was achieved at nine epochs with a training time of 163 [m] and 40 [s]. For finer image resolutions, training will require longer times.

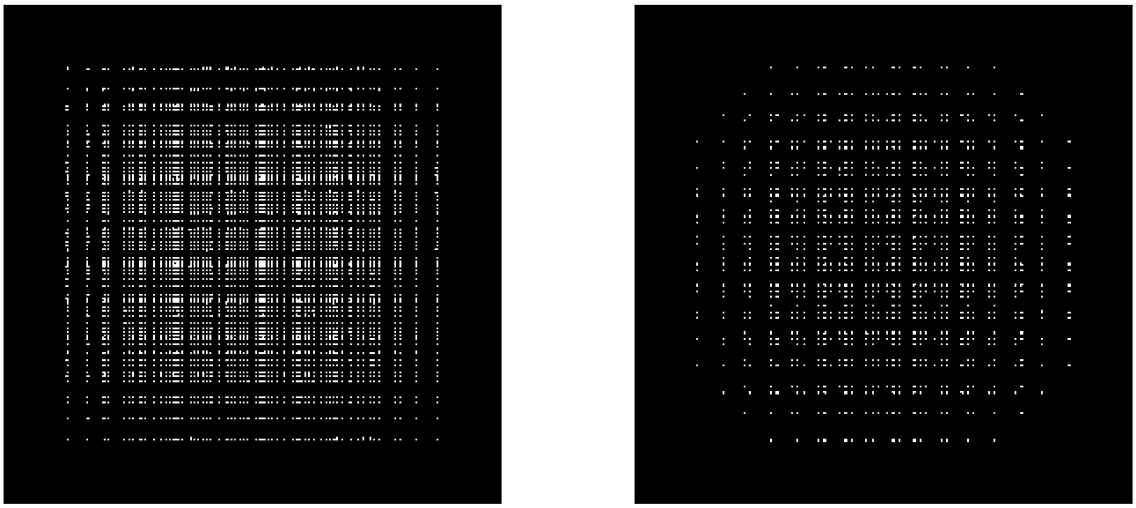

(a) 16-QAM SNR1=10, SNR2=15, SNR3=20 dB (b) 32-QAM SNR1=15, SNR2=20 dB

Figure 4.40: Constellation R = 0.004

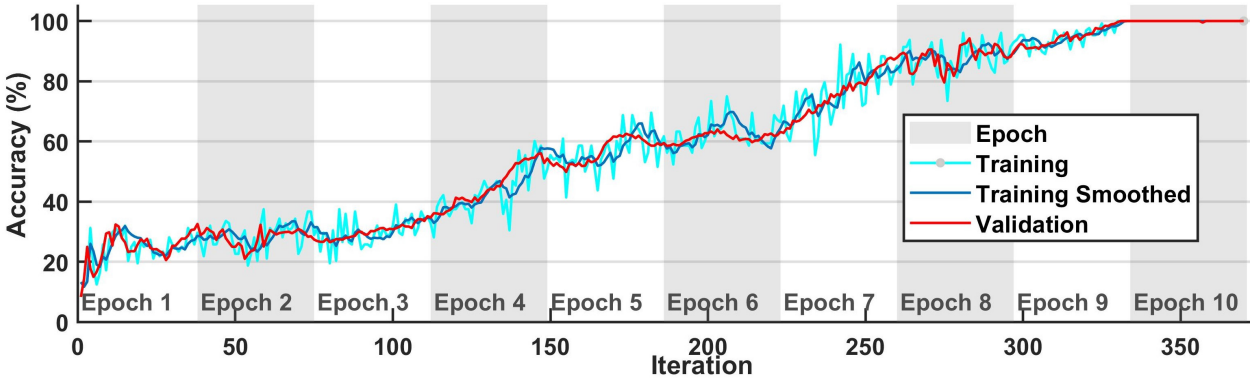

Figure 4.41: Accuracy for R = 0.004

To compare CNN performance for different resolutions, Fig. 4.42 shows validation accuracies for R= 0.004, 0.005, 0.007, 0.008, and 0.01 versus the number of iterations. All tested resolutions with different converging rates achieved 100% classification accuracy. Results show that when R increases and image size decreases, CNN performance

converges faster to obtain optimal value. Fig. 4.43 illustrates normalized training time (left blue axes) and the epoch in which 100% accuracy was obtained (right orange axes) for each R value. Training time and epoch decrease with increased resolution. R=0.01 achieved 100% testing accuracy within the first epoch with a training time of 30 m and 49 s; therefore, resolution 0.01 and 113 x 113 image size was selected for the remaining analyses.

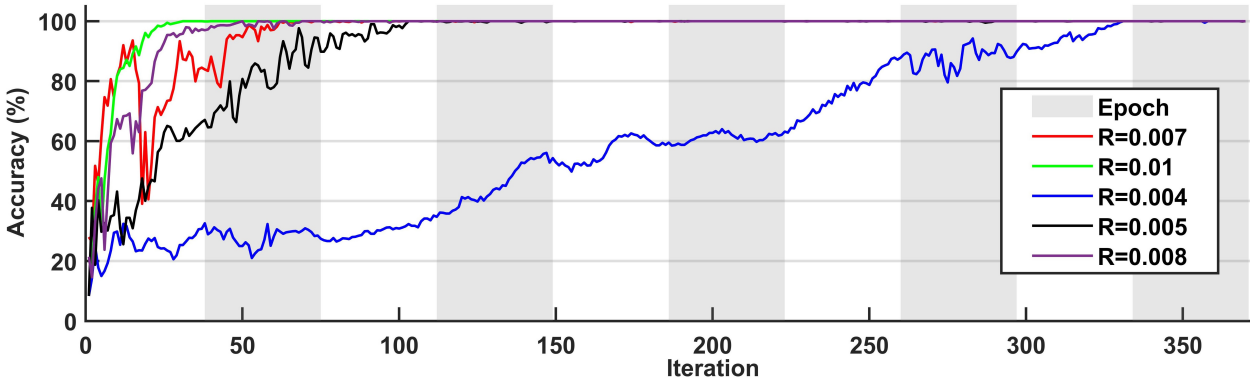

Figure 4.42: Accuracy for varying R

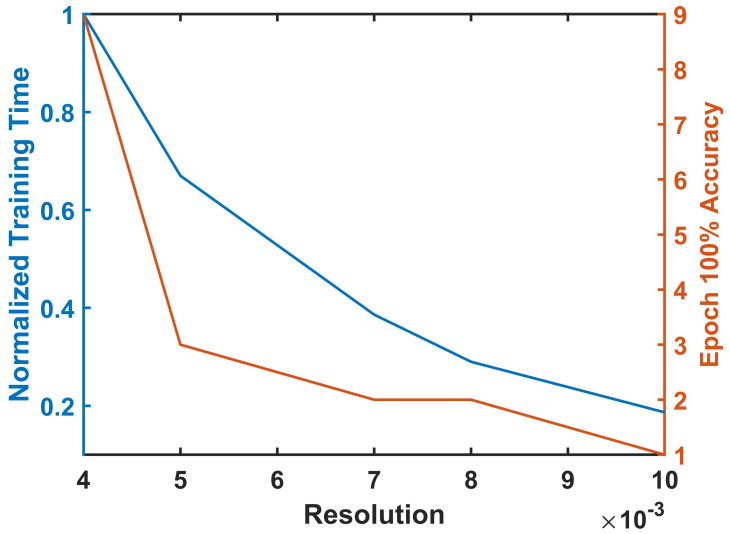

Figure 4.43: Training time and accuracy epoch versus R

2. **Data size analysis**

Dataset scalability relative to saving computational time and memory complexity is a challenging issue for ML algorithms [101]. Accordingly, sample size N analysis was

conducted. Data set originally consisted of 6,000 images and was consecutively reduced in steps of 1,000 images. Testing accuracy for N =5,000 (green line), N =3,000 (blue line), and N=1,000 (red line) data objects (i.e., images) is illustrated in Fig. 4.44. 100% accuracy was achieved within 45 iterations, and training time decreased with data size reduction: 30 m 49 s for N=5,000; 9 m 14 s for N=3,000; and 1 m 42 s for N=1,000. Thus, a smaller data set achieved optimum performance.

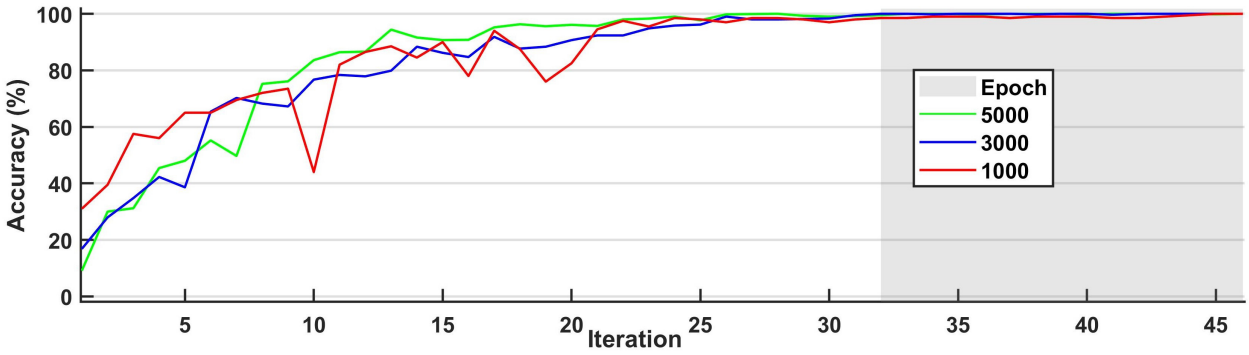

Figure 4.44: Accuracy for varying dataset size

3. **Atmospheric turbulence**

FSOC links can be significantly affected by atmospheric turbulence-induced scintillation, which leads to power loss, random fluctuation of the received intensity, and degraded communication performance. The proposed method was evaluated under a log-normal turbulent channel [106]. Atmospheric turbulence severity was varied through the refractive index structure constant parameter C_n^2. Turbulence with $C_n^2 = 10^{-15}$ (i.e., low turbulence) and 10^{-14} (i.e., moderate turbulence) $[m^{-2/3}]$ was analyzed.

Fig. 4.45 shows how constellation diagram images illustrated in Figs. 4.38d, 4.38e, and 4.38c were affected by low and moderate turbulence regimes. Notably, turbulence strongly affects constellation diagrams. Symbols are not distinguishable, causing one point to be misidentified and leading to symbol error and poor communication performance. However, the CNN model proved to accurately classify user number and modulation format. Fig. 4.46 shows validation accuracy versus iteration number for no turbulence (red line), low turbulence (green line), and moderate turbulence (blue

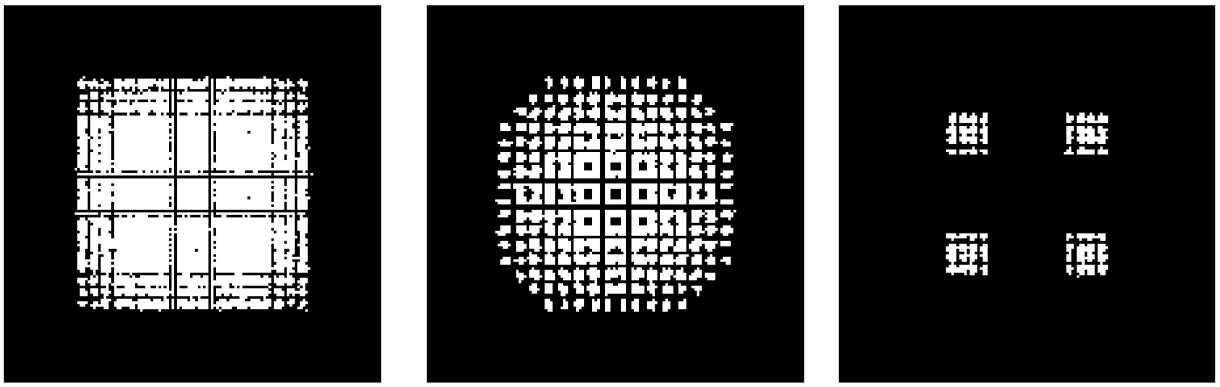

(a) Fig 1(d) low turbulence (b) Fig 1(e) low turbulence (c) Fig 1(c) low turbulence

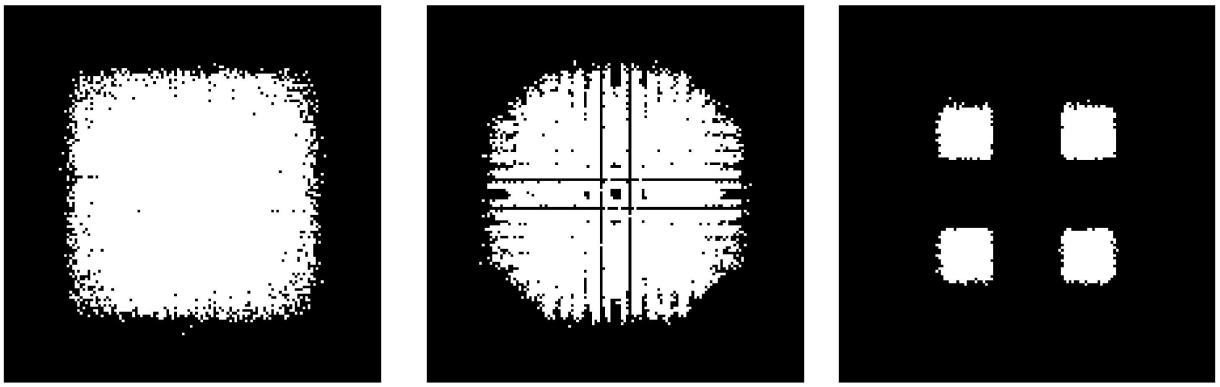

(d) Fig 1(d) high turbulence (e) Fig 1(e) high turbulence (f) Fig 1(c) high turbulence

Figure 4.45: Turbulence analysis

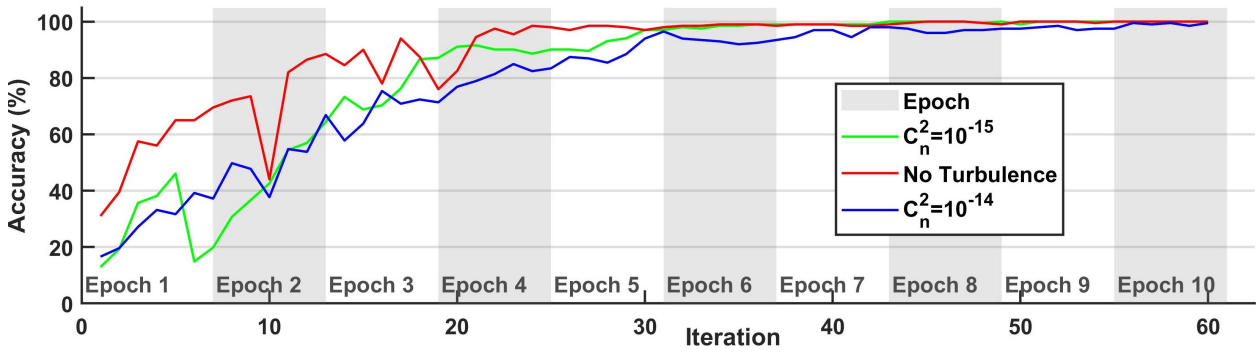

Figure 4.46: Accuracy for varying turbulence severity

line). $C_n^2 = 10^{-14}$ achieved 99.5% accuracy, while 100% was obtained within 10 epochs for other scenarios. Results demonstrated that the CNN model is robust against atmospheric turbulence, leading to successful and accurate classification and suggesting immunity to additive noise. Accordingly, it seems that constellation shape, rather than symbol distance and position, contains additional intrinsic useful features for the CNN.

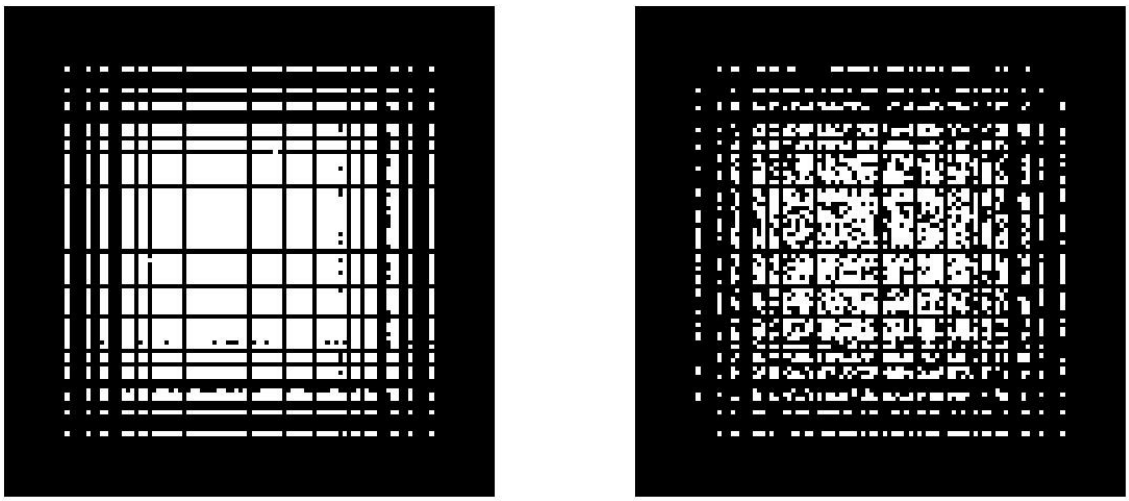

(a) $N_S = 44,000$ (b) $N_S = 4,000$

Figure 4.47: 16-QAM SNR1=10, SNR2=15, SNR3=20 dB

Each point in the constellation diagram refers to a received complex symbol. High number of symbols leads to a constellation diagram with enough points to represent all possible symbols that can be transmitted by the system. However, collecting a huge amount of data symbols requires longer acquisition time or excessive memory requirement for the cognitive optical receiver. As such, the minimum number of symbols N_S (i.e., minimum sampling time) for obtaining accurate constellation reproduction should be identified. Number of received signal symbols was reduced from 84,000 to 4,000 in steps of 20,000 samples to determine how the constellation diagram is affected and, consequently, how classification accuracy changes accordingly.

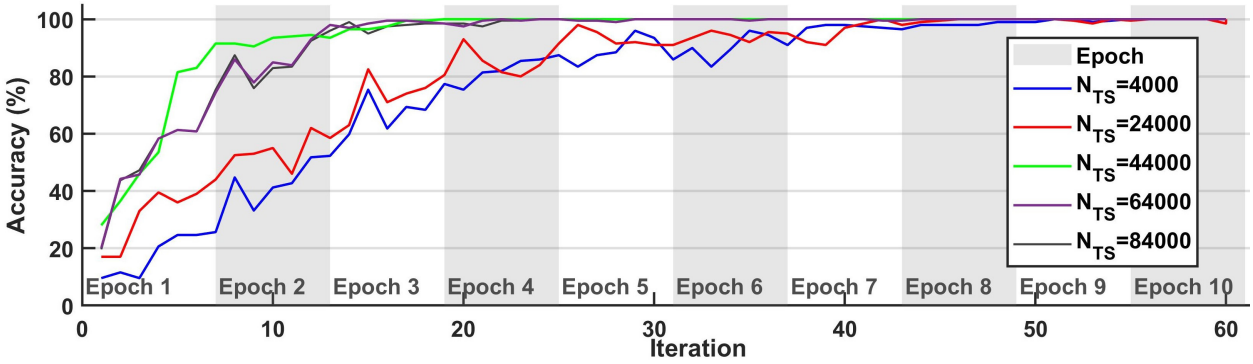

Figure 4.48: Accuracy for varying number of symbols

Fig. 4.47 illustrates constellation diagrams of Fig. 4.38d with reduced number of symbols for N_S= 44,000, shown in 4.47a and N_S= 4,000 in 4.47b. Clearly, the image in Fig. 4.47 shows reduced constellation point density. However, classification results in Fig. 4.48 demonstrate that 100% accuracy is obtained for all tested symbol numbers. N_S=4,000 (blue line) and 24,000 (red line) converge to maximum performance after 50 iterations (9th epoch), while N_S=84,000, 64,000, and 44,000 (black, purple and green line respectively) reach maximum accuracy more rapidly in less than 25 iterations (4th epoch).

CHAPTER 5

OWC TESTBED

The OWC testbed is poised to provide a research and testing platform for designing and validating next generation optical wireless/fiber-based communication systems and technologies. The testbed was designed to provide a hardware and software infrastructure for fast and flexible algorithm development, prototype testing, and system upgrading. The system consists of a cognitive, multi-node, modular, high-speed, and real-time design suitable for demonstrating next-generation FSO systems that would allow omni-directional and multi-user communication.

5.1 Testbed Design

A depiction of the testbed is illustrated in Fig. 5.1. Free-space optical pathways are drawn in light blue; fiber-based optical pathways are drawn in blue; and electrical pathways are drawn in black. The testbed consists of four independently tunable, optical transmitters that can be configured and combined to emulate various communication scenarios through the use of optical combiners, power splitters, attenuators, and phase shifters. As such, diverse user configurations can be implemented (e.g., single user on single channel, single user on multiple channels, multiple users on single channel, and multiple users or multiple channels). A picture of the OWC testbed is illustrated in Fig. 5.2. Each transmitting node consists of an optical laser source (i.e., $\lambda 1 = 1310$ nm or $\lambda 2 = 1550$ nm operating wavelength) with variable transmitting power driven by independently configurable PRBS. Nodes are based on an intensity modulation (OOK) with direct detection (IM/DD) scheme. Laser 1 consists of: a high-speed digital reference optical transmitter (i.e., C-band Thorlabs MX10B) with embedded optical attenuator for tuning transmitted

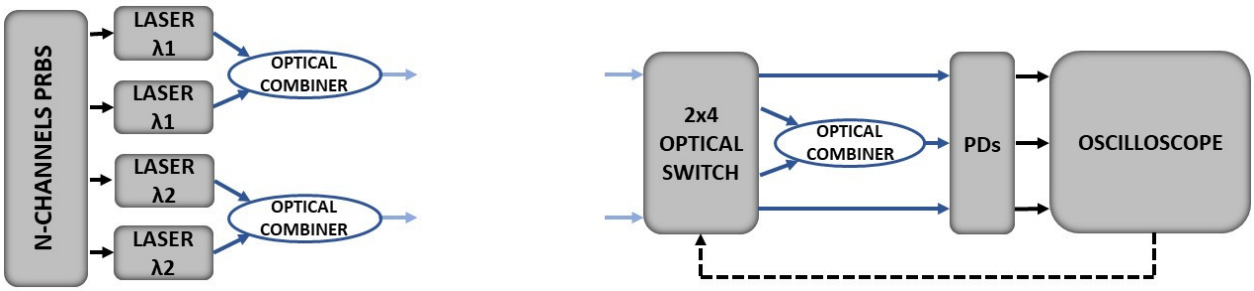

Figure 5.1: OWC testbed depiction

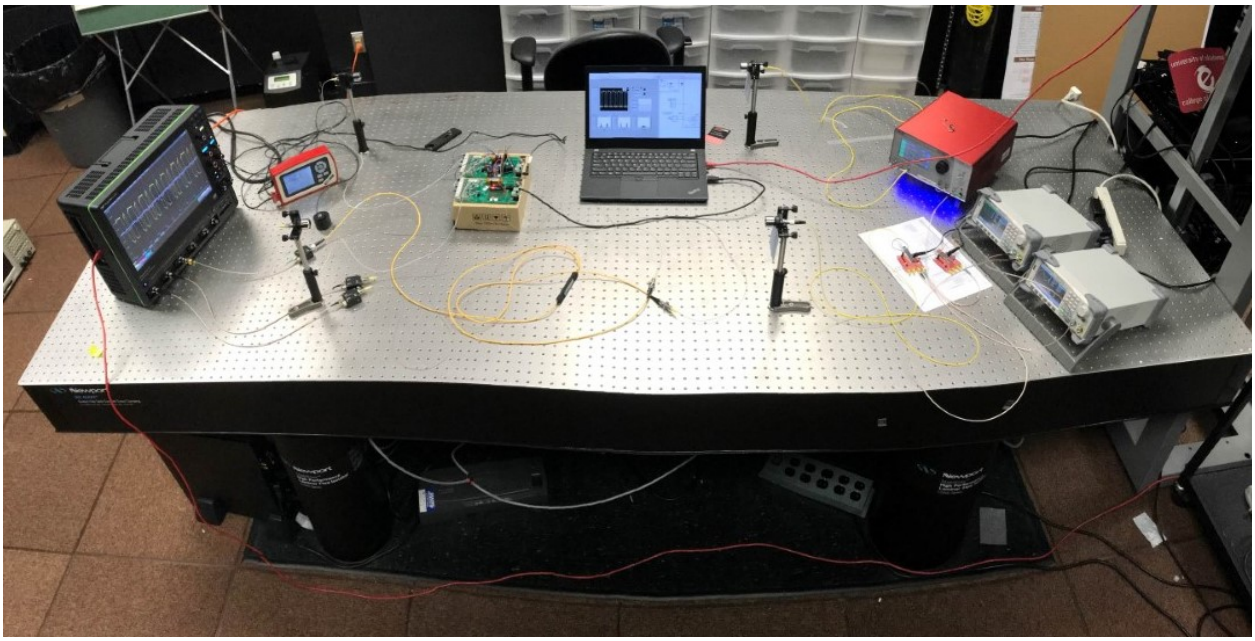

Figure 5.2: OWC testbed

power; remaining lasers consisting of optical module transceivers (SFP, 1310/1550 nm wavelengths) independently driven via Hitech Global SMA to SFP conversion modules; and an external variable optical attenuators (Thorlabs VOA50-FC) for varying transmitted power. PRBSs are generated with two independent, dual-channel pulse/arbitrary waveform generators, namely SIGLENT's SDG6032X. Each channel can be independently configured to generate the desired PRBS amplitude and length. Transmitted signals can be combined using optical combiners and power splitters with various input-output configurations (e.g., 4x1, 2x1, 2x2, and the like) to cover several configuration scenarios. Two pairs of collimators with 1550 nm wavelength-dependent and 1310 nm wavelength-dependent lenses are used to propagate the combined signals through a free space turbulent and/or non-turbulent channel.

Atmospheric turbulence can be generated and evaluated using the turbulence box detailed in Chapter 3. Received optical signals are collected by two 1x2 MEMS optical switches (e.g., Thorlabs OSW12-1310E). The design and configuration of the two optical switches make them function as a single 2x4 optical switch, as illustrated in Fig. 5.3. If received optical signals IN1 and IN2 are copies of the same signal (i.e., single user), the optical switch will route the input signals to $OUT1_2$ and $OUT2_2$ to be summed with the optical combiner to increase signals SNR and therefore signal quality. Then signals are directed to a photode-

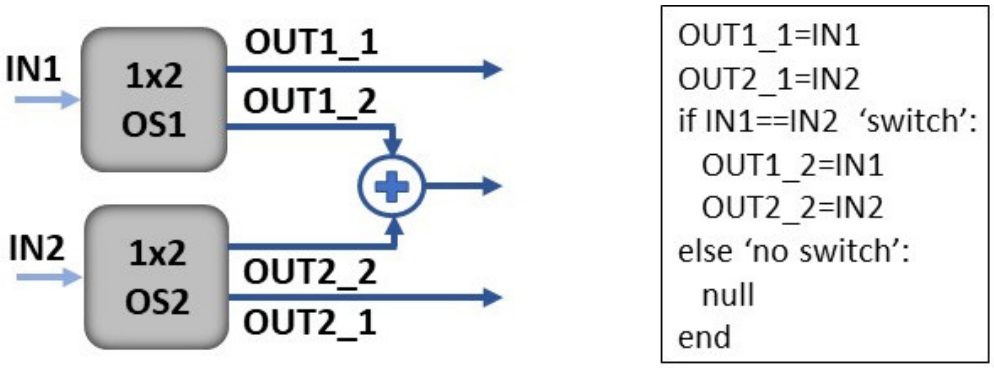

Figure 5.3: Optical switch working principle

tector for signal processing. Given that IN1 and IN2 are two different signals (e.g., multiple users or different single users), the optical switch will guide the signals directly to the photodetectors for signal decoding. Three 5-GHz bandwidth InGaAs photodetectors, namely Thorlabs DET08CFC, were used for optical-to-electrical conversion. Photodetector outputs were connected to WavePro 254HD-MS oscilloscope with a 20 GSample/s sampling rate for data collection and visualization.

5.2 Initial Measurements Results

To prove and validate testbed capabilities and to highlight the testbed limitations, several experiments were conducted. Preliminary results of BER, attenuation, insertion losses, and multiple user configuration analysis were reported.

5.2.1 BER Analysis

To evaluate high-speed, single user communication capabilities, BER measure-

ments were collected for varying transmitted power and data-rate, as illustrated in 5.4. User

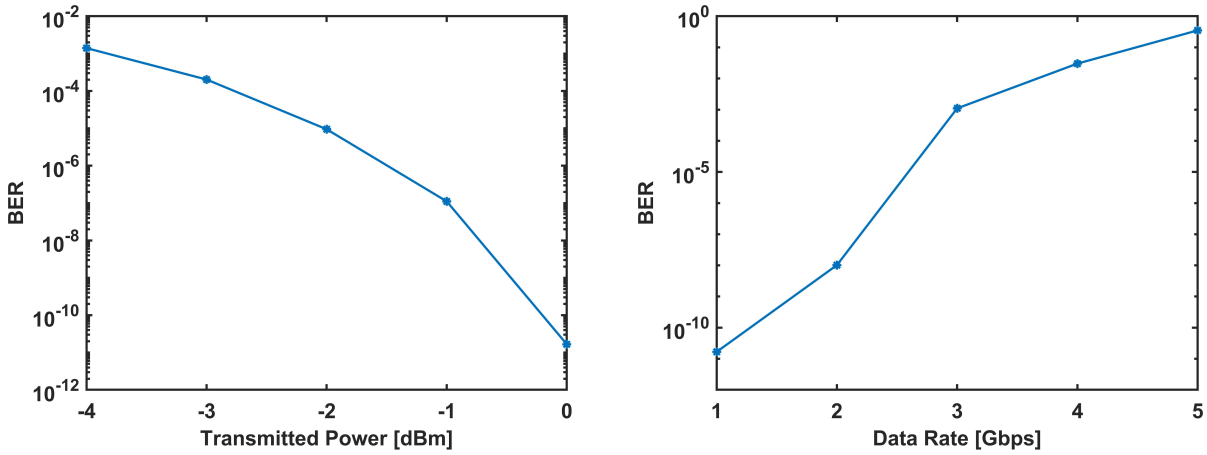

(a) Transmitted power (b) Data rate

Figure 5.4: BER

1 was selected for the analysis, and BER measurements were collected using the BertScope analyzer, SyntheSys Research BSA12500A. Transmitted power was varied from -4 dBm to 5 dBm. BER versus power is shown in Fig. 5.4a; zero BER was obtained for transmitted power greater than 0 dBm. Fig. 5.4b shows how BER increased with the data-rate in the range 1 Gbps to 5 Gbps. Notably, BER value greater than 10^{-3} were obtained due to limited photodetector bandwidth. Upgrading the photodetectors would allow single user communication with communication speed greater than 10 Gbps.

5.2.2 Loss Insertion

Developed O-MAC, signal processing, and ML algorithms are power-based methodologies. These techniques employ received signal amplitude as a distinct feature for detecting and decoding simultaneously transmitting users. As such, power analysis in terms of attenuation and insertion losses is crucial for testing proposed techniques. Received optical power was measured in various sections along the optical link using the optical spectrum analyzer Advantest Q8384. In particular, optical power before the optical switch, after the switch, and after the optical combiner was collected. Transmitted optical power of user 1 was varied from -2 dBm to 5 dBm with 1 Gbps data-rate. Fig. 5.5a shows received optical power

[dBm] versus transmitted optical power [dBm]. Received optical power decreases linearly with decreasing of transmitted power for all three sections studied. Fig. 5.5b illustrates the average total attenuation [dB] introduced by the optical switches (4.46 dB) and by the optical combiner (1.88 dB). Thus, a total average insertion loss at the receiving side of 6.34 dB is obtained. Total attenuation is due to the insertion losses of the devices and the cou-

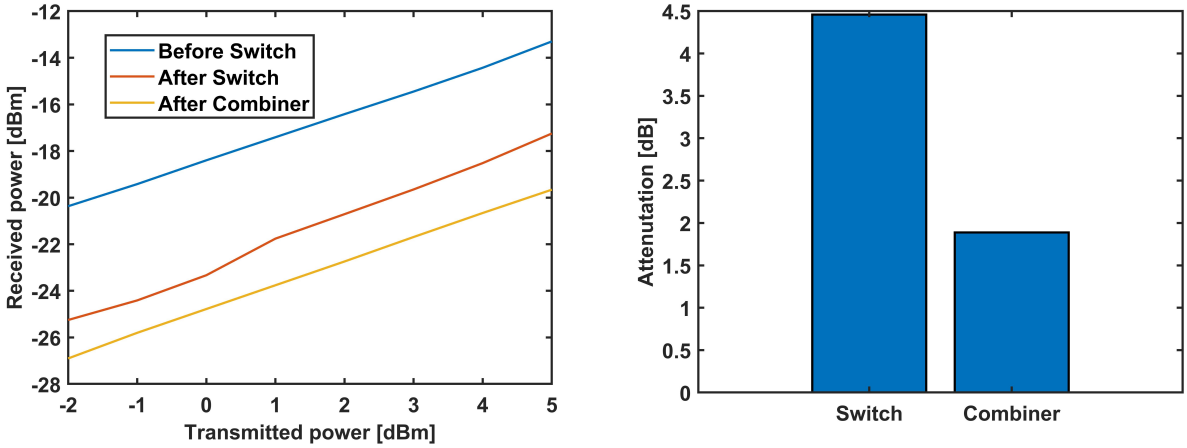

(a) Loss insertion

(b) Total attenuation

Figure 5.5: Loss

pling losses of fiber connections. Hence, to reduce losses, MF, customized devices, and/or multi-mode devices could be adopted, resulting in additional coupling power.

5.2.3 Multi-User Configurations

The transmitting side of the OWC testbed consists of four independently tunable users that can be configured to emulate various communication scenarios. Data in the time-domain and frequency-domain can be displayed and collected for further analysis. Fig. 5.6 shows possible experimental scenarios where transmitted power and data-rate for each user were set as: 2.87 dBm and 50 Mbps for user 1; 1 dBm and 250 Mbps for user 2; -2.81 dBm and 150 Mbps for user 3; and -3.98 dBm and 100 Mbps for user 4. Single user on single channel, single user on multiple channels (e.g., two), multiple users (e.g., four) on single channel, and multiple users (e.g., three) on multiple channels (e.g., two) are illustrated in 5.6a, 5.6b, 5.6c, 5.6d respectively.

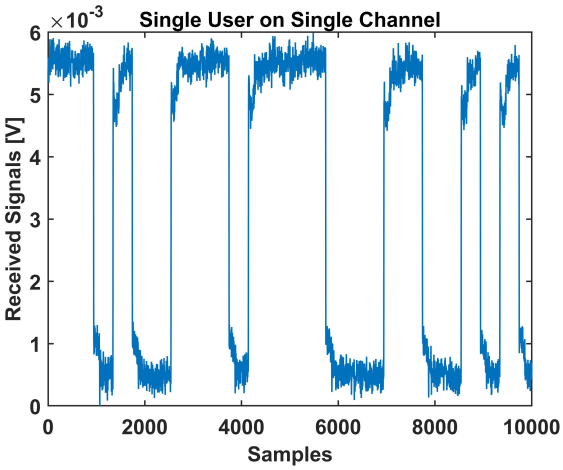

(a) Single user on single channel

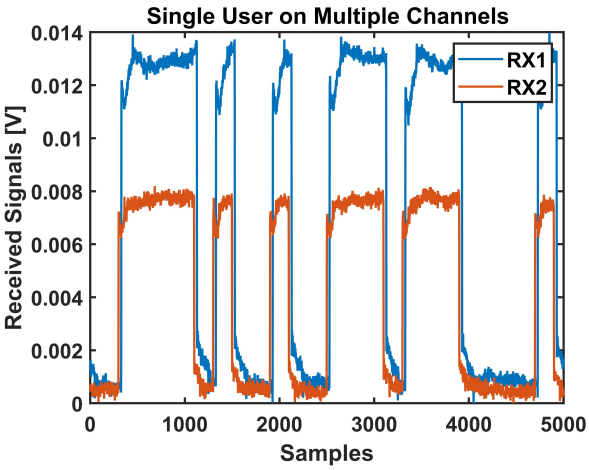

(b) Single user on multiple channels

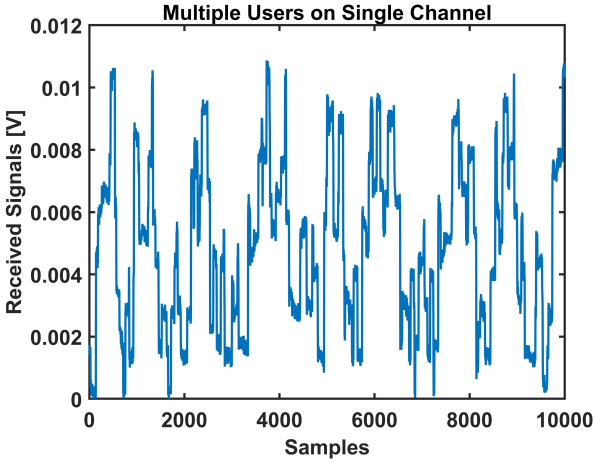

(c) Multiple users on single channel

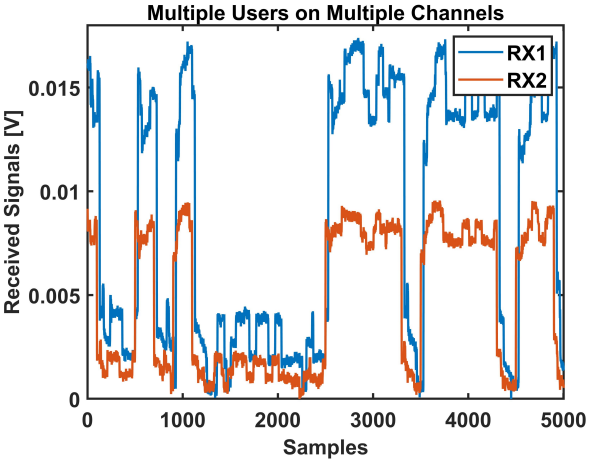

(d) Multiple users on multiple channels

Figure 5.6: Communication scenarios

5.3 Applications

The platform targets a variety of application scenarios for testing several FSOC systems for space, aerial, and terrestrial communication links. Upgrading of the current software and hardware would extend the listed capabilities. Examples of system capabilities that can be tested with the actual testbed include:

1. time-domain and frequency-domain analysis,

2. real-time and off-line analysis,

3. point-to-point and multi-point to multi-point analysis,

4. omni-directional receiver,

5. atmospheric turbulence,

6. noise effects,

7. diversity combining, and

8. BER analysis.

Hardware upgrades and device replacement will further extend testbed capabilities. Additional scenarios and applications could be emulated and evaluated, including:

1. higher number of users,

2. multi-level modulation format,

3. user mobility, and

4. pointing errors.

CHAPTER 6

CONCLUSION AND FUTURE WORK

6.1 Conclusion

The new high data-rate and high bandwidth services/applications required from forthcoming terrestrial, aerial, and space networks dramatically increase the demand for wireless capacity. Multi-point FSOC has been considered a promising technology for meeting these needs and supporting high data-rate, high capacity, low power consumption, secure, and high-density communication networks. Such requirements mean that next-generation wireless networks will face increased system complexity, especially due to the heterogeneity of supported services, applications, devices, and transmission technologies. Cognitive multi-user FSOC networks offer a significant solution for addressing these new network requirements and for tackling the increased system complexity. This work has successfully demonstrated the use of signal processing, O-MAC, and ML techniques for performing cognitive, multi-user FSOC. The strength of the proposed solutions is the use of intelligent algorithms along with the extensive experimental validation of their ability to support multiple users, sharing allocation resources and communicating in a single, optical channel without affecting system SWaP specifications.

In this dissertation, signal processing algorithms, including ICA and NOMA, were first investigated and experimentally validated to separate signals from simultaneously transmitting users into single and multiple channels. ICA was shown to require a number of receivers that is equal to the number of transmitting users, albeit without prior knowledge of users and channel properties. NOMA, on the other end, required only one receiver with prior information of the channel. Results confirmed that both techniques can be implemented to successfully decode overlapping transmitted signals under several configuration scenarios.

Supporting experimentation was designed to carefully investigate the effect of two parameters, namely signal power and data-rate on signal separation. Tests were conducted for two users under both turbulent and non-turbulent scenarios. Results demonstrated that between the two users, a minimum power difference of 3 dB was required to achieve cross-correlation greater than 0.9 when using both ICA and NOMA methods. However, ICA was shown to be sensitive to data-rate difference, while NOMA showed superior performance for the tested range. Moreover, to overcome the limitations of each method and to consider potential CSI availability at the receiver side, combinations of the various O-MAC techniques were evaluated through additional experimentation. On both received signals, NOMA proved to demodulate the signals with the greatest accuracy, although CSI was required at both receivers. A combination ICA and NOMA reconstructed the transmitted signals with a mean cross-correlation greater than 0.9 between the three users. ICA and NOMA required CSI at one receiver. Ultimately, utilizing NOMA on one received signal delivered the poorest performance due to cancellation errors propagated on the two weaker users.

Following the initial experimentation, a novel methodology for introducing intelligence at the PHY of FSOC networks was presented and tested with a goal of estimating the number of concurrently transmitting users sharing allocation resources. The proposed technique was designed to leverage unsupervised ML based on the amplitude information of the received mixed signals. Four clustering techniques, namely K-mean, hierarchical, K-medoid and fuzzy clustering, were experimentally validated in a setup composed of a fiber-bundle receiver, in which one, two, and three independent transmitting users were tested. Moreover, a weighted clustering analysis was proposed to correct for underestimation when users with the same power values are received. Experimental results proved that the proposed technique can successfully estimate the number of transmitting users, even under moderate atmospheric turbulence, with accuracy greater than 92%. Effect of sample size and receiver sampling rate on the estimation accuracy were experimentally tested and evaluated. Then, an empirical equation for successfully predicting the number of detectable users, given the number of time series samples and receiver sampling rate, was derived and validated. To

overcome system limitations, a CNN-based methodology was presented to jointly estimate number of concurrently transmitting users and their modulation format. Simulation results showed an accuracy greater than 99.5% in the presence of medium atmospheric turbulence and for several communication scenarios. Lastly, this dissertation investigated the use of supervised ML for joint estimation of received SNRs for two transmitting users overlapping into a single node receiver. Multiple classification algorithms (e.g., SVM, ANN, RF) were evaluated using two approaches for training the model. First, a histogram of received mixed signal amplitude was employed as input to the classification model, and then, local maxima location of the histogram was utilized. Experimental results proved successful estimation of joint SNR1 from user 1 and SNR2 from user 2 with classification accuracy of 92%. Also investigated was the effect of a varying number of instances for training the classifier and number of time series samples for feature extraction of received signal.

The design, implementation, and testing of an OWC testbed was conducted to fully characterize, test, and evaluate cognitive and multi-user technologies developed throughout the entirety of research efforts reported in this work. The testbed consists of multiple, independently tunable optical transmitters that can be configured to emulate various communication scenarios (e.g., point-to-point, point to multi-point, multi-point to multi-point). At the receiver side, an optical switch was adopted to route the detected signals to pre-defined paths for signal processing. Testbed capabilities for single user and multiple user scenarios were demonstrated. Besides providing preliminary results for experimentation carried out for this work, the OWC testbed represents a research and testing platform that could be exploited by both research and commercial entities for testing and validating a wide spectrum of ideas and applications.

6.2 Future Work

The research outcomes presented in this dissertation represent the preliminary findings and results for implementing a cognitive, multi-user FSOC. Several hardware, software, and testing research efforts could be pursued for practical realization of an FSOC

system. Accordingly, this dissertation concludes by posing some research questions, along with possible solutions that could be investigated and pursued as future research directions.

- What is the maximum number of users and the highest modulation order supported by NOMA, ICA and by combination of them?

  Testing O-MAC techniques for different configuration scenarios including more transmitting users and/or receiving nodes with different modulation formats.

- Is it possible to support O-MAC techniques with an omni-directional optical receiver to increase number of communicating users?

  Designing and building an omni-directional transceiver to exploit spatial and angular diversity along with the demonstrated O-MAC and ML methodologies.

- Can we further increase system capacity by combining the demonstrated power-based O-MAC with other conventional O-MAC?

  Integration of DWDM with ICA/NOMA to increase the number of channels (DWDM) and capacity per each channel (O-MAC).

- What is the trade-off between number of simultaneously transmitting users and their modulation order?

  Extension of the OWC test bed to cover higher number of users (i.e., > 4) and higher level modulation format (e.g., QAM).

- What other communication/performance parameters could be estimated to facilitate and automate O-MAC techniques and performance evaluation prior to signal demodulation?

  Develop ML algorithms for estimating parameters of interest (e.g., SINR, BER, C_n^2, and others) of each user when they share the same channel allocation resources.

BIBLIOGRAPHY

[1] Markets and Markets. Free Space Optics (FSO) and Visible Light Communication (VLC)/Light Fidelity (Li-Fi) Market by Component (LED, Photodetector, Microcontroller, and Software), Transmission Type, Application, and Geography - Global Forecast to 2023, 2018.

[2] M A Khalighi and M Uysal. Survey on Free Space Optical Communication: A Communication Theory Perspective. *IEEE Communications Surveys & Tutorials*, 16(4):2231–2258, 2014.

[3] Linda M Thomas, Courtney Mann, Christopher I Moore, and William S Rabinovich. Free space optics for tactical environments. In *Free-Space Laser Communication and Atmospheric Propagation XXX*, volume 10524, page 1052402. International Society for Optics and Photonics, 2018.

[4] Gregory Staple and Kevin Werbach. The end of spectrum scarcity [spectrum allocation and utilization]. *IEEE spectrum*, 41(3):48–52, 2004.

[5] Mingjie Feng and Shiwen Mao. Harvest the potential of massive MIMO with multilayer techniques. *IEEE Network*, 30(5):40–45, 2016.

[6] Fan Wang, Haibo Wang, Hao Feng, and Xiaohui Xu. A hybrid communication model of millimeter wave and microwave in D2D network. In *2016 IEEE 83rd vehicular technology conference (VTC Spring)*, pages 1–5. IEEE, 2016.

[7] A Sharmila and P Dananjayan. Spectrum Sharing Techniques in Cognitive Radio Networks–A Survey. In *2019 IEEE International Conference on System, Computation, Automation and Networking (ICSCAN)*, pages 1–4. IEEE, 2019.

[8] Gustavo Wagner Oliveira Da Costa. Dynamic spectrum sharing among femtocells: Coping with spectrum scarcity in 4g and beyond. 2012.

[9] Amal Ali Algedir and Hazem H Refai. Energy Efficiency Optimization and Dynamic Mode Selection Algorithms for D2D Communication Under HetNet in Downlink Reuse. *IEEE Access*, 8:95251–95265, 2020.

[10] Ian F Akyildiz, Josep Miquel Jornet, and Chong Han. Terahertz band: Next frontier for wireless communications. *Physical Communication*, 12:16–32, 2014.

[11] Mostafa Zaman Chowdhury, Md Tanvir Hossan, Amirul Islam, and Yeong Min Jang. A comparative survey of optical wireless technologies: architectures and applications. *IEEE Access*, 6:9819–9840, 2018.

[12] Hemani Kaushal, V K Jain, and Subrat Kar. *Free Space Optical Communication*. Springer, 2017.

[13] Zabih Ghassemlooy, Wasiu Popoola, and Sujan Rajbhandari. *Optical wireless communications: system and channel modelling with Matlab®*. CRC press, 2019.

[14] Bruce Moision, Baris Erkmen, Edward Keyes, Todd Belt, Oliver Bowen, Devin Brinkley, Paul Csonka, Michael Eglington, Andrei Kazmierski, Nam-hyong Kim, John Moody, Thanh Tu, and William Vermeer. Demonstration of free-space optical communication for long-range data links between balloons on Project Loon. In *Proc.SPIE*,

volume 10096, feb 2017.

[15] E A Park, D Cornwell, and D Israel. NASA's Next Generation ≥100 Gbps Optical Communications Relay. In *2019 IEEE Aerospace Conference*, pages 1–9, 2019.

[16] Antonios Seas, Bryan Robinson, Tina Shih, Farzana Khatri, and Mark Brumfield. Optical communications systems for NASA's human space flight missions. In *Proc.SPIE*, volume 11180, jul 2019.

[17] Tamer Rakia, Fayez Gebali, Hong-Chuan Yang, and Mohamed-Slim Alouini. Throughput analysis of point-to-multi-point hybric FSO/RF network. In *Communications (ICC), 2017 IEEE International Conference on*, pages 1–6. IEEE, 2017.

[18] Yagiz Kaymak, Roberto Rojas-Cessa, Jianghua Feng, Nirwan Ansari, MengChu Zhou, and Tairan Zhang. A Survey on Acquisition, Tracking, and Pointing Mechanisms for Mobile Free-Space Optical Communications. *IEEE Communications Surveys & Tutorials*, 20(2):1104–1123, 2018.

[19] Jayasri Akella, Murat Yuksel, and Shiv Kalyanaraman. Multi-channel communication in free-space optical networks for the last-mile. In *Local & Metropolitan Area Networks, 2007. LANMAN 2007. 15th IEEE Workshop on*, pages 43–48. IEEE, 2007.

[20] Francesco Musumeci, Cristina Rottondi, Avishek Nag, Irene Macaluso, Darko Zibar, Marco Ruffini, and Massimo Tornatore. An overview on application of machine learning techniques in optical networks. *IEEE Communications Surveys & Tutorials*, 2018.

[21] Faisal Nadeem Khan, Qirui Fan, Chao Lu, and Alan Pak Tao Lau. An Optical Communication's Perspective on Machine Learning and Its Applications. *Journal of Lightwave*

Technology, 37(2):493–516, 2019.

[22] Javier Mata, Ignacio De Miguel, Ramon J Duran, Noemi Merayo, Sandeep Kumar Singh, Admela Jukan, and Mohit Chamania. Artificial intelligence (AI) methods in optical networks: A comprehensive survey. *Optical switching and networking*, 28:43–57, 2018.

[23] I I Robert H BRUMLEY, Robert H Brumley III, Richard Rosenthal, Steven BIRRELL, Michael J Reedy, and Fletcher W Brumley. Optical communication system, jan 2020.

[24] F Aveta, H H Refai, and P LoPresti. Multi-user FSO communication link. In *2017 Cognitive Communications for Aerospace Applications Workshop (CCAA)*, pages 1–5, 2017.

[25] Federica Aveta, Hazem H Refai, Peter LoPresti, Sarah A Tedder, and Bryan L Schoenholz. Independent component analysis for processing optical signals in support of multi-user communication. In *Free-Space Laser Communication and Atmospheric Propagation XXX*, volume 10524, page 105241D. International Society for Optics and Photonics, 2018.

[26] Federica Aveta, Hazem H Refai, and Peter LoPresti. Multiple access technique in a high-speed free-space optical communication link: independent component analysis. *Optical Engineering*, 58(3):36111, 2019.

[27] Federica Aveta and Hazem H. Refai. Free space optical non-orthogonal multiple access experimentation. In *Free-Space Laser Communication and Atmospheric Propagation XXX*, page 60, 2019.

[28] Federica Aveta, Hazem H Refai, and Peter LoPresti. Multi-user detection in optical wireless communication. In *2019 15th International Wireless Communications & Mobile Computing Conference (IWCMC)*, pages 214–219. IEEE, 2019.

[29] Federica Aveta, Hazem H. Refai, and Peter G. LoPresti. Number of Users Detection in Multi-Point FSOC Using Unsupervised Machine Learning. *IEEE Photonics Technology Letters, [In Press]*, 2019.

[30] Federica Aveta and Hazem H Refai. Modulation format and number of users classification in multipoint free-space optical communication using convolutional neural network. *Optical Engineering*, 59(6):60501, 2020.

[31] F Aveta, H H Refai, and P LoPresti. Cognitive Multi-Point Free Space Optical Communication: Real-Time Users Discovery using Unsupervised Machine Learning. *IEEE Access*, page 1, 2020.

[32] Yusuf Said Eroğlu, İsmail Güvenç, Alphan Şahin, Yavuz Yapıcı, Nezih Pala, and Murat Yüksel. Multi-Element VLC Networks: LED Assignment, Power Control, and Optimum Combining. *IEEE Journal on Selected Areas in Communications*, 36(1):121–135, 2018.

[33] Sifat Ibne Mushfique, Prabath Palathingal, Yusuf Said Eroglu, Murat Yuksel, Ismail Guvenc, and Nezih Pala. A Software-Defined Multi-Element VLC Architecture. *IEEE Communications Magazine*, 56(2):196–203, 2018.

[34] Syed H Murshid and Michael F Finch. Omnidirectional free space optical communications receiver, dec 2016.

[35] Syed H Murshid, Gregory L Lovell, and Michael F Finch. Modeled and experimental results of an omnidirectional free-space optical receiver architecture. *Optical Engineering*, 56(3):36108, 2017.

[36] Peter LoPresti, Nathan Hutchins, Steven Kohrmann, M Fahd Babelli, and Hazem H Refai. Wavelength dependence of a fiber-bundle based FSO link. In *Globecom Workshops (GC Wkshps), 2014*, pages 493–498. IEEE, 2014.

[37] Asaad Kaadan, Hazem Refai, and Peter Lopresti. Spherical FSO receivers for UAV communication: geometric coverage models. *IEEE Transactions on Aerospace and Electronic Systems*, 52(5):2157–2167, 2016.

[38] Asaad Kaadan, Hazem H Refai, and Peter G LoPresti. On the development of modular optical wireless elements (MOWE). In *Globecom Workshops (GC Wkshps), 2015 IEEE*, pages 1–7. IEEE, 2015.

[39] D J Geisler, T M Yarnall, G Lund, C M Schieler, M L Stevens, N K Fontaine, B S Robinson, and S A Hamilton. Experimental comparison of 3-mode and single-mode coupling over a 1.6-km free-space link. In *Free-Space Laser Communication and Atmospheric Propagation XXX*, volume 10524, page 105240H. International Society for Optics and Photonics, 2018.

[40] Gregory Baiden and Alberto Rui Frutuoso Barroso. Omnidirectional optical wireless communications receiver & system, mar 2018.

[41] Alberto Rui Frutuoso Barroso and Julia Johnson. Optical wireless communications omnidirectional receivers for vehicular communications. *AEU - International Journal of Electronics and Communications*, 79:102–109, 2017.

[42] Luigi Bagnato, Laurent Jacques, Pierre Vandergheynst, Hossein Afshari, Alexandre Schmid, and Yusuf Leblebici. Omnidirectional sensor array system, jan 2018.

[43] Jose E Velazco, Joseph Griffin, Danny Wernicke, John Huleis, Andrew DeNucci, Ozdal Boyraz, and Imam Uz Zaman. Inter-satellite omnidirectional optical communicator for remote sensing. In *Proc.SPIE*, volume 10769, sep 2018.

[44] Jose E Velazco. Method and apparatus for omnidirectional optical communication, jul 2019.

[45] Junyi Zhou, Yufeng Shao, Yue Zhou, Changxiang Li, Zhifeng Wang, Wenzhe Ma, XingPing Ji, and Jianjun Wang. Analysis of Coherent MPSK-OFDMA Signals in FSO Communication System under Complex Weather Conditions.

[46] Jiang Liu, Jin Sando, Shigeru Shimamoto, Chiemi Fujikawa, and Kashiko Kodate. Experiment on space and time division multiple access scheme over free space optical communication. *IEEE Transactions on Consumer Electronics*, 57(4), 2011.

[47] Naresh Kumar and Trilok Singh. 2.50 Gbit/s optical CDMA over FSO communication system. *Optik-International Journal for Light and Electron Optics*, 125(16):4538–4542, 2014.

[48] Zeping Zhao, Zhike Zhang, Jun Tan, Yu Liu, and Jianguo Liu. 200 Gb/s FSO WDM communication system empowered by multiwavelength directly modulated TOSA for 5G wireless networks. *IEEE Photonics Journal*, 10(4):1–8, 2018.

[49] S M Riazul Islam, Nurilla Avazov, Octavia A Dobre, and Kyung-Sup Kwak. Power-domain non-orthogonal multiple access (NOMA) in 5G systems: potentials and chal-

lenges. *IEEE Communications Surveys & Tutorials*, 2017.

[50] Bangjiang Lin, Xuan Tang, and Zabih Ghassemlooy. Optical power domain noma for visible light communications. *IEEE Wireless Communications Letters*, 8(4):1260–1263, 2019.

[51] Xiaodong Liu, Zezong Chen, Yuhao Wang, Fuhui Zhou, Yusang Luo, and Rose Qingyang Hu. BER Analysis of NOMA-Enabled Visible Light Communication Systems With Different Modulations. *IEEE Transactions on Vehicular Technology*, 68(11):10807–10821, 2019.

[52] Mansourah K A Aljohani, Mohamed O I Musa, Mohammed T Alresheedi, and Jaafar M H Elmirghani. WDM NOMA VLC Systems. In *2019 21st International Conference on Transparent Optical Networks (ICTON)*, pages 1–5. IEEE, 2019.

[53] Yusuf Said Eroglu, Chethan Kumar Anjinappa, Ismail Guvenc, and Nezih Pala. Slow beam steering and NOMA for indoor multi-user visible light communications. *IEEE Transactions on Mobile Computing*, 2019.

[54] Ruijie Li and Anhong Dang. Multi-user access in wireless optical communication system. *Optics express*, 26(18):22658–22673, 2018.

[55] Marzieh Najafi, Vahid Jamali, Panagiotis D Diamantoulakis, George K Karagiannidis, and Robert Schober. Non-orthogonal multiple access for FSO backhauling. In *Wireless Communications and Networking Conference (WCNC), 2018 IEEE*, pages 1–6. IEEE, 2018.

[56] Thomas Shun Rong Shen, Ke Meng, Alan Pak Tao Lau, and Zhao Yang Dong. Opti-

cal performance monitoring using artificial neural network trained with asynchronous amplitude histograms. *IEEE Photonics Technology Letters*, 22(22):1665–1667, 2010.

[57] Faisal Nadeem Khan, Thomas Shun Rong Shen, Yudi Zhou, Alan Pak Tao Lau, and Chao Lu. Optical performance monitoring using artificial neural networks trained with empirical moments of asynchronously sampled signal amplitudes. *IEEE Photonics Technology Letters*, 24(12):982–984, 2012.

[58] Takahito Tanimura, Takeshi Hoshida, Jens C Rasmussen, Makoto Suzuki, and Hiroyuki Morikawa. OSNR monitoring by deep neural networks trained with asynchronously sampled data. In *2016 21st OptoElectronics and Communications Conference (OECC) held jointly with 2016 International Conference on Photonics in Switching (PS)*, pages 1–3. IEEE, 2016.

[59] Takahito Tanimura, Takeshi Hoshida, Tomoyuki Kato, Shigeki Watanabe, and Hiroyuki Morikawa. Data-analytics-based Optical Performance Monitoring Technique for Optical Transport Networks. In *Optical Fiber Communication Conference*, OSA Technical Digest (online), page Tu3E.3, San Diego, California, 2018. Optical Society of America.

[60] N G Gonzalez, D Zibar, and I T Monroy. Cognitive digital receiver for burst mode phase modulated radio over fiber links. In *36th European Conference and Exhibition on Optical Communication*, pages 1–3, 2010.

[61] Jakob Thrane, Jesper Wass, Molly Piels, Julio C M Diniz, Rasmus Jones, and Darko Zibar. Machine Learning Techniques for Optical Performance Monitoring From Directly Detected PDM-QAM Signals. *Journal of Lightwave Technology*, 35(4):868–875, 2017.

[62] Sandra Aladin and Christine Tremblay. Cognitive Tool for Estimating the QoT of New Lightpaths. In *Optical Fiber Communication Conference*, OSA Technical Digest (online), page M3A.3, San Diego, California, 2018. Optical Society of America.

[63] W Mo, Y Huang, S Zhang, E Ip, D C Kilper, Y Aono, and T Tajima. ANN-Based Transfer Learning for QoT Prediction in Real-Time Mixed Line-Rate Systems. In *2018 Optical Fiber Communications Conference and Exposition (OFC)*, pages 1–3, 2018.

[64] William M Turner, Daniel J Tebben, Jason R Madsen, and Anurag Dwivedi. A testbed to emulate next-generation directional RF and free-space optical tactical networks. In *Testbeds and Research Infrastructures for the Development of Networks & Communities and Workshops, 2009. TridentCom 2009. 5th International Conference on*, pages 1–5. IEEE, 2009.

[65] Daniel Tebben, Anurag Dwivedi, Jason Madsen, William Turner, Jeff Garretson, and Tim Frey. Tenet (tactical edge network emulation tool): A tool for connectivity analysis for tactical scenario. In *Military Communications Conference, 2008. MILCOM 2008. IEEE*, pages 1–7. IEEE, 2008.

[66] P Harshavardhana, Daniel J Tebben, Anurag Dwivedi, and A Roger Hammons. DAPR (Distributed adaptive precomputed restoration): An Algorithm for Assured availability Directional RF and FSO MANET. In *Military Communications Conference, 2007. MILCOM 2007. IEEE*, pages 1–6. IEEE, 2007.

[67] Morio Toyoshima, Yasushi Munemasa, Hideki Takenaka, Yoshihisa Takayama, Yoshisada Koyama, Hiroo Kunimori, Toshihiro Kubooka, Kenji Suzuki, Shinichi Yamamoto, and Shinichi Taira. Terrestrial Free-Space Optical Communications Network Testbed: INNOVA. *Proc. ICSOS*, pages S2–4, 2014.

[68] Morio Toyoshima, Yasushi Munemasa, Hideki Takenaka, Yoshihisa Takayama, Yoshisada Koyama, Hiroo Kunimori, Toshihiro Kubooka, Kenji Suzuki, Shinichi Yamamoto, and Shinichi Taira. Introduction of a terrestrial free-space optical communications network facility: IN-orbit and Networked Optical ground stations experimental Verification Advanced testbed (INNOVA). In *Free-Space Laser Communication and Atmospheric Propagation XXVI*, volume 8971, page 89710R. International Society for Optics and Photonics, 2014.

[69] D Giggenbach, J Poliak, R Mata-Calvo, C Fuchs, N Perlot, R Freund, and T Richter. Preliminary results of Terabit-per-second long-range free-space optical transmission Experiment THRUST. In *Unmanned/Unattended Sensors and Sensor Networks XI; and Advanced Free-Space Optical Communication Techniques and Applications*, volume 9647, page 96470H. International Society for Optics and Photonics, 2015.

[70] Juraj Poliak, Dirk Giggenbach, Florian Moll, Fabian Rein, Christian Fuchs, and Ramon Mata Calvo. Terabit-throughput GEO satellite optical feeder link testbed. In *Telecommunications (ConTEL), 2015 13th International Conference on*, pages 1–5. IEEE, 2015.

[71] Steven M Zuraski, Steven T Fiorino, Elizabeth A Beecher, Nathan M Figlewski, Jason D Schmidt, and Jack E McCrae. Electro-optic testbed utilizing a dynamic range gated Rayleigh beacon for atmospheric turbulence profiling. In *Optics in Atmospheric Propagation and Adaptive Systems XIX*, volume 10002, page 1000207. International Society for Optics and Photonics, 2016.

[72] Mikhail A Vorontsov, Gary W Carhart, Matt Banta, Thomas Weyrauch, John Gowens, and John C Carrano. Atmospheric Laser Optics Testbed (A_LOT): Atmospheric propagation characterization, beam control, and imaging results. In *Advanced Wavefront*

Control: Methods, Devices, and Applications, volume 5162, pages 37–49. International Society for Optics and Photonics, 2003.

[73] H R Burris, C I Moore, L M Wasiczko, M F Stell, R Mahon, W S Rabinovich, and W J Scharpf. Comparison study of packet error rates and bit error rates at the US Naval Research Laboratory free-space lasercom test facility. In *Atmospheric Propagation IV*, volume 6551, page 65510G. International Society for Optics and Photonics, 2007.

[74] H R Burris, C I Moore, L A Swingen, M J Vilcheck, D A Tulchinsky, R Mahon, L M Wasiczko, M F Stell, M A Davis, and S W Moore. Latest results from the 32 km maritime lasercom link at the Naval Research Laboratory, Chesapeake Bay Lasercom Test Facility. In *Atmospheric Propagation II*, volume 5793, pages 209–220. International Society for Optics and Photonics, 2005.

[75] Christopher I Moore, Harris R Burris, William S Rabinovich, Linda Wasiczko, Lee A Swingen, Rita Mahon, Mena F Stell, G Charmaine Gilbreath, and William J Scharpf. Overview of NRL's maritime laser communication test facility. In *Free-Space Laser Communications V*, volume 5892, page 589206. International Society for Optics and Photonics, 2005.

[76] David C Harrison, Alexander G Hayes, Leaf A Jiang, Eric L Hines, and Jonathan M Richardson. The MIT Lincoln Laboratory optical systems test facility. In *Technologies for Synthetic Environments: Hardware-in-the-Loop Testing XI*, volume 6208, page 620801. International Society for Optics and Photonics, 2006.

[77] Leaf A Jiang, David R Schue, David C Harrison, Alexander G Hayes, Eric L Hines, Jonathan M Richardson, and Kenneth J Schultz. Active range of the optical systems test facility at MIT lincoln laboratory. In *Laser Radar Technology and Applications*

XI, volume 6214, page 62140Q. International Society for Optics and Photonics, 2006.

[78] Jonathan M Richardson and John C Aldridge. The standoff aerosol active signature testbed (SAAST) at MIT Lincoln Laboratory. In *Chemical and Biological Standoff Detection III*, volume 5995, page 59950E. International Society for Optics and Photonics, 2005.

[79] Thomas Little, Michael Rahaim, Iman Abdalla, Emily Lam, Richard Mcallister, and Anna Maria Vegni. A multi-cell lighting testbed for VLC and VLP. In *LIFI Congress (GLC), 2018 Global*, pages 1–6. IEEE, 2018.

[80] Boris Shishkin, Doug Pfeil, Danh Nguyen, Kevin Wanuga, James Chacko, Jeremy Johnson, Nagarajan Kandasamy, Timothy P Kurzweg, and Kapil R Dandekar. SDC testbed: Software defined communications testbed for wireless radio and optical networking. In *Modeling and Optimization in Mobile, Ad Hoc and Wireless Networks (WiOpt), 2011 International Symposium on*, pages 300–306. IEEE, 2011.

[81] Aapo Hyvärinen and Erkki Oja. Independent component analysis: algorithms and applications. *Neural networks*, 13(4):411–430, 2000.

[82] Nikolaos Mitianoudis and Mike E Davies. Audio source separation: Solutions and problems. *International Journal of Adaptive Control and Signal Processing*, 18(3):299–314, 2004.

[83] Te-Won Lee, Mark Girolami, and Terrence J Sejnowski. Independent component analysis using an extended infomax algorithm for mixed subgaussian and supergaussian sources. *Neural computation*, 11(2):417–441, 1999.

[84] John R Hershey and Peder A Olsen. Approximating the Kullback Leibler divergence between Gaussian mixture models. In *Acoustics, Speech and Signal Processing, 2007. ICASSP 2007. IEEE International Conference on*, volume 4, pages IV–317. IEEE, 2007.

[85] Aapo Hyvarinen. Fast and robust fixed-point algorithms for independent component analysis. *IEEE transactions on Neural Networks*, 10(3):626–634, 1999.

[86] P Xie and S L Grant. A Fast and Efficient Frequency-Domain Method for Convolutive Blind Source Separation. In *2008 IEEE Region 5 Conference*, pages 1–4, 2008.

[87] Claude Elwood Shannon. Communication in the presence of noise. *Proceedings of the IRE*, 37(1):10–21, 1949.

[88] William S Rabinovich, Rita Mahon, Mike S Ferraro, James L Murphy, and Christopher I Moore. Scintillation recording and playback in free-space optical links. *Optical Engineering*, 55(11):111613, 2016.

[89] P Sudhakar, K Anitha Sheela, D Ramakrishna Rao, and Malladi Satyanarayana. Experimental investigations on range-resolved refractive index structure parameter C n 2, by optical measurements over a 2.0 km free space laser path. In *Lidar Remote Sensing for Environmental Monitoring XV*, volume 9879, page 987919. International Society for Optics and Photonics, 2016.

[90] Muhammad Saeed Khan, Muhammad Amin, Muhammad Saleem Awan, Abid Ali Minhas, Jawad Saleem, and Rahim Dad Khan. Statistical modeling of optical attenuation measurements in continental fog conditions. *Optical Engineering*, 56(3):36113, 2017.

[91] Zhiguo Ding, Xianfu Lei, George K Karagiannidis, Robert Schober, Jinhong Yuan, and Vijay K Bhargava. A survey on non-orthogonal multiple access for 5G networks: Research challenges and future trends. *IEEE Journal on Selected Areas in Communications*, 35(10):2181–2195, 2017.

[92] Wonjae Shin, Mojtaba Vaezi, Byungju Lee, David J Love, Jungwoo Lee, and H Vincent Poor. Non-orthogonal multiple access in multi-cell networks: Theory, performance, and practical challenges. *IEEE Communications Magazine*, 55(10):176–183, 2017.

[93] Hanaa Marshoud, Sami Muhaidat, Paschalis C Sofotasios, Sajjad Hussain, Muhammad Ali Imran, and Bayan S Sharif. Optical Non-Orthogonal Multiple Access for Visible Light Communication. *IEEE Wireless Communications*, 25(2):82–88, 2018.

[94] Saad Al-Ahmadi, Omar Maraqa, Murat Uysal, and Sadiq M Sait. Multi-User Visible Light Communications: State-of-the-Art and Future Directions. *IEEE Access*, 6:70555–70571, 2018.

[95] Souvik Sen, Naveen Santhapuri, Romit Roy Choudhury, and Srihari Nelakuditi. Successive interference cancellation: A back-of-the-envelope perspective. In *Proceedings of the 9th ACM SIGCOMM Workshop on Hot Topics in Networks*, page 17. ACM, 2010.

[96] Linglong Dai, Bichai Wang, Yifei Yuan, Shuangfeng Han, I Chih-Lin, and Zhaocheng Wang. Non-orthogonal multiple access for 5G: solutions, challenges, opportunities, and future research trends. *IEEE Communications Magazine*, 53(9):74–81, 2015.

[97] It Ee Lee, Zabih Ghassemlooy, Wai Pang Ng, and Murat Uysal. Performance analysis of free space optical links over turbulence and misalignment induced fading channels. In *Communication Systems, Networks & Digital Signal Processing (CSNDSP), 2012*

8th International Symposium on, pages 1–6. IEEE, 2012.

[98] Peter G LoPresti, Shannon Suddath, Hazem Refai, Sarah A Tedder, and Bryan L Schoenholz. Examining the ability of an FSO receiver to simultaneously communicate with multiple transmitters. In *Free-Space Laser Communication and Atmospheric Propagation XXX*, volume 10524, page 1052413. International Society for Optics and Photonics, 2018.

[99] Neil J Salkind. *Encyclopedia of research design*, volume 1. Sage, 2010.

[100] Arun K Majumdar. *Advanced Free Space Optics (FSO): A Systems Approach*, volume 186. Springer, 2014.

[101] Pang-Ning Tan, Michael Steinbach, and Vipin Kumar. *Introduction to data mining*. Pearson Education India, 2016.

[102] Tao Chen and Hong Ren Wu. Impulse noise removal by multi-state median filtering. In *2000 IEEE International Conference on Acoustics, Speech, and Signal Processing. Proceedings (Cat. No.00CH37100)*, volume 4, pages 2183–2186 vol.4, 2000.

[103] Aditi Malik and Preeti Singh. Free Space Optics: Current Applications and Future Challenges. *International Journal of Optics*, 2015:945483, 2015.

[104] Steve Hanneke. The optimal sample complexity of PAC learning. *The Journal of Machine Learning Research*, 17(1):1319–1333, 2016.

[105] Saad Albawi, Tareq Abed Mohammed, and Saad Al-Zawi. Understanding of a convolutional neural network. In *2017 International Conference on Engineering and Tech-*

nology (ICET), pages 1–6. IEEE, 2017.

[106] Hassan Moradi, Maryam Falahpour, Hazem H Refai, Peter G LoPresti, and Mohammed Atiquzzaman. BER analysis of optical wireless signals through lognormal fading channels with perfect CSI. In *2010 17th International Conference on Telecommunications*, pages 493–497. IEEE, 2010.

APPENDIX A

ICA ALGORITHMS

A.1 FastICA

The FastICA algorithm is an HOS method for BSS solution that aims to estimate directions for maximizing nonGaussianity of the original components by using a fixed-point iteration scheme. Accordingly, negentropy J serves as a quantitative measure of nonGaussianity for a random variable [23]:

$$J(y) = H(y_{gauss}) - H(y) \tag{A.1}$$

where H is the differential entropy; y is a random vector, and y_{gauss} is a Gaussian random vector with the same covariance of y. Since Gaussian variables have the largest entropy among all random variables of equal variance [26], negentropy will be zero for variables with Gaussian distributions and non-negative for other distributions. Due to the computational difficulties associated with computing negentropy, approximations based on a non-quadratic function G were used and expressed as:

$$J(y) \propto \Big[E\left\{G(y)\right\} - E\left\{G(v)\right\}\Big]^2 \tag{A.2}$$

where v is a Gaussian variable of zero mean and unit variance. However, a two-step, preprocessing stage (i.e., centering and whitening) is required. First, observed signal x is centered by subtracting its mean value $m = E\{x\}$. Then, centered signal x is linearly transformed in white vector $\tilde{x}$ so that its covariance matrix is the identity matrix $E\{\tilde{x}\tilde{x}^T\} = I$.

Eigenvalue decomposition (EVD) of covariance matrix $E\{\tilde{x}\tilde{x}^T\} = EDE^T$ is performed, where E is the orthogonal matrix of eigenvectors and D is the diagonal matrix of eigenvalues. After whitening is applied, mixing matrix A is transformed into a new orthogonal matrix $\tilde{A}$ as follows:

$$\tilde{x} = ED^{-1/2}E^T x = ED^{-1/2}E^T As = \tilde{A}s \tag{A.3}$$

This process lowers solution complexity due to the reduced number of parameters (i.e.., from n^2 to $n(n-1)/2$). After pre-processing, the FastICA algorithm is applied. This one-unit algorithm aims to maximize negentropy in A.2 computed for $y = w^T x$. Optimum $E\{G(w^T x)\}$ under constraint $E\{(w^T x)^2\} = \|w\|^2 = 1$, can be found using the Lagrange function. Therefore, the final solution is expressed, as follows:

$$w = E\{xG'(w^T x)\} - E\{G''(w^T x)\}w \tag{A.4}$$

where G' and G'' are the first and second order derivative of G function. This algorithm has several advantages over other methods. For example, extremely fast convergence (e.g., cubic or at least quadratic), validity for any non-Gaussian distribution, no requirement for probability distribution estimation, and improvement given the selection of a proper non-linear function G.

A.2 JADE

JADE exploits fourth order moments to separate source signals from mixed received signals. Fourth cumulants Q_i^z of whitened signals are computed. A set of $n(n+1)/2$ eigenvalues λ_i and eigenmatrices V_i of Q_i^z are considered and processed by joint approximate diagonalization to determine unitary matrix. This is then used to obtain source signal estimation. A detailed explanation of JADE can be found in [47].